SATBAYEV UNIVERSITY

ISSN 2959-2348 (Online)

ENGINEERING JOURNAL of Satbayev University

Volume 147 (Issue 3)
June 2025

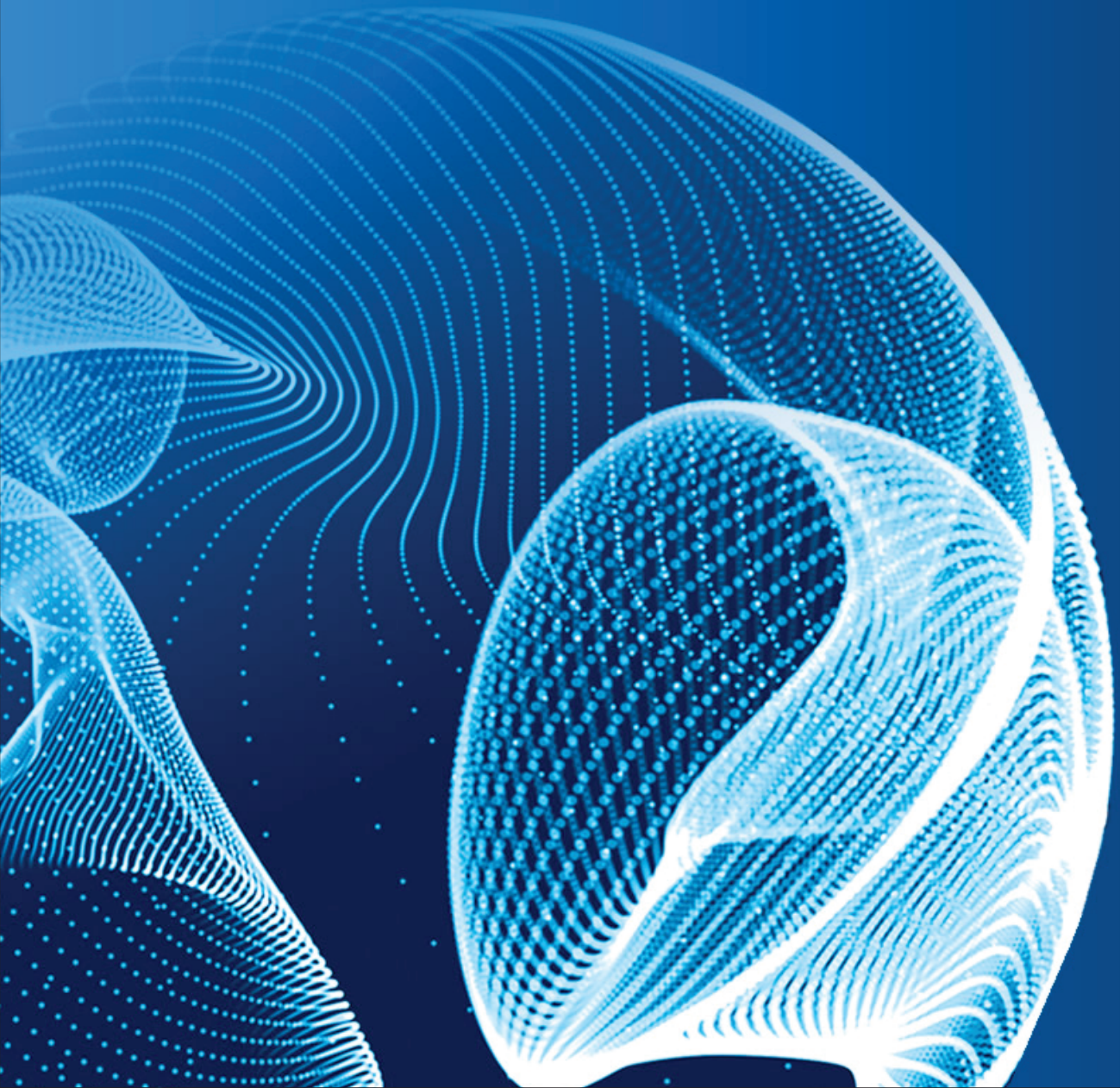

eISSN 2959-2348

eISSN 2959-2348

eISSN 2959-2348

SATBAYEV UNIVERSITY

Engineering Journal of Satbayev University

Volume 147 (2025), Issue 3, 1-6

https://doi.org/10.51301/ejsu.2025.i3.01

Mechanical and tribological behavior of multilayer and monolayer TiN-based coatings

B.K. Kenzhaliyev, A.K. Kenzhegulov*, A.A. Mamaeva, A.V. Panichkin, B.B. Kshibekova

Institute of Metallurgy and Ore Beneficiation, Almaty, Kazakhstan

**Corresponding author: kazakh_1403@mail.ru*

Abstract. This study investigates the mechanical and tribological properties of monolayer TiN coatings and multilayer TiN/TiCN coatings deposited via direct current magnetron sputtering onto titanium substrates (VT1-0). The coatings were characterized by microstructure, nanohardness, elastic modulus, and tribological performance under lubricated friction conditions. Scanning electron microscopy (SEM) revealed that the coatings exhibit a uniform microstructure without visible defects and a typical columnar growth morphology. Nanoindentation tests demonstrated that the multilayer TiN/TiCN coatings possess enhanced hardness (up to 23.5 GPa) and elastic modulus (191 GPa) compared to the monolayer TiN, attributed to interlayer strengthening effects and redistribution of residual stresses. Tribological tests using a ball-on-disk configuration under lubricated conditions showed that the multilayer coatings exhibit a significantly lower coefficient of friction (0.10–0.13) and improved wear resistance compared to the TiN coating. This behavior is associated with TiCN layers, which reduce interfacial adhesion, promote uniform load distribution, and facilitates the formation of a protective tribofilm. The results confirm that the TiN/TiCN multilayer coatings offer superior mechanical and tribological properties, making them promising candidates for engineering components operating under friction and wear conditions.

Keywords: *multilayer coating, magnetron sputtering, coefficient of friction, nanohardness, wear resistance.*

Received: 24 February 2025
Accepted: 15 June 2025
Available online: 30 June 2025

1. Introduction

Recent advances in materials science and surface engineering have increasingly focused on the development of high-performance protective coatings to reduce wear and friction in tribological components of machines and mechanisms [1-3]. Among such coatings, titanium nitride (TiN) and titanium carbonitride (TiCN) compounds are fascinating due to their high microhardness, chemical inertness, and thermal stability. Multilayer systems such as TiN/TiCN exhibit improved operational properties by combining the strength TiN with's enhanced plasticity of TiCN, effectively mitigating stress accumulation during service [4-6].

The key parameters determining the effectiveness of such coatings include tribological and nanomechanical properties, such as coefficient of friction (CoF), wear rate (WR), nanohardness, and elastic modulus. These properties are strongly influenced by the coating's structure, surface morphology, and deposition parameters. Direct current (DC) magnetron sputtering is widely used in scientific and industrial settings to produce coatings with high density, uniform microstructure, and strong adhesion to the substrate [7, 8]. However, optimizing multilayer systems requires comprehensive studies, including investigations of morphological features and tribological behavior under boundary lubrication conditions.

Most tribological studies of TiN/TiCN multilayer coatings have been conducted under dry sliding conditions in ambient air. While this approach allows for evaluating basic wear characteristics, it does not always reflect the actual operating conditions of tribological components in mechanical engineering and other industries. In recent years, growing attention has been paid to testing in liquid media that simulate realistic friction and wear processes in mechanical systems. Testing in lubricated environments–such as oils and functional fluids–provides deeper insight into the influence of lubrication on tribological behavior, including changes in CoF, WR, and the mechanism of protective film formation on the contact surface.

For instance, Su Y.L. [9] investigated multilayer TiN/TiCN/TiN coatings under both dry and lubricated conditions using HD-150 oil and water-based lubricants. Results showed that under HD-150 lubrication, the CoF decreased to 0.25, and wear was completely absent due to the formation of a protective tribofilm at the contact surface. In contrast, dry sliding conditions resulted in severe surface damage, iron oxide formation, and fluctuations in CoF.

Tribological tests of multilayer TiAlCN and TiTaCN coatings under dry and lubricated conditions [8] revealed that the CoF ranged from 0.13 to 0.85 in dry sliding. At the same time, under lubrication, it dropped significantly to 0.0015-0.081, with the minimum value (0.0015) recorded for $TiAlCN^{-1}$. The WR in lubricated environments was also considerably lower – for example, 7.4×10^{-9} mm³/N·m for $TiAlCN^{-2}$.

bagdaulet_k@mail.ru; kazakh_1403@mail.ru; ak78@mail.ru; abpanichkin@mail.ru; alzh_79@mail.ru
Engineering Journal of Satbayev University. eISSN 2959-2348. Published by Satbayev University

In another study [10], the tribological performance of nanostructured coatings was evaluated under reciprocating sliding against 100Cr6 steel balls using paraffin oil as a lubricant, under varying loads (2 and 7 N) and temperatures (30 and 100°C). The CoF remained largely unaffected by testing parameters; however, a significant reduction in wear volume was observed at elevated temperatures.

Despite extensive research on TiN/TiCN multilayer coatings, tribological assessments under lubricated conditions remain limited in scientific literature. This study deposited monolayer TiN and multilayer TiN/TiCN coatings on VT1-0 titanium substrates via DC magnetron sputtering. The primary objective was to investigate the mechanical and tribological properties of these TiN/TiCN-based multilayer coatings under lubricated friction conditions.

2. Materials and methods

Multilayer TiN/TiCN and monolayer TiN coatings were deposited by direct current (DC) magnetron sputtering using a VT1-0 titanium target (equivalent to GRADE 2) with a diameter of 99 mm. As substrates, finely polished titanium plates (15 × 15 mm, VT1-0) and p-type Si(100) wafers (SW GmbH, Schramberg, Germany) were used. The silicon substrates were employed for morphological investigations, while 58 mm-diameter titanium discs served as substrates for tribological testing.

All substrates underwent surface preparation involving sanding with abrasive paper and polishing with diamond paste. The prepared substrates were mounted on a substrate holder inside the vacuum chamber. The chamber was evacuated to a base pressure of 10^{-3} Pa, after which ion cleaning was performed using argon at a pressure of 0.2 Pa, voltage of 2.5 kV, and current of 20-25 mA for 30 minutes, employing an APEL-IS-21CELL ion source (Applied Electronics, Tomsk, Russia).

Following ion cleaning, the substrates were positioned opposite the APEL-MRE100 magnetron source (Applied Electronics, Tomsk, Russia). A constant substrate bias voltage of –100 V was applied, and the target-to-substrate distance was maintained at 300 mm. The reactive gases used were propane and nitrogen, with argon as the inert carrier gas. The flow rates of both reactive and inert gases were regulated using PPG-12 mass flow controllers (Eltochpribor, Moscow, Russia). All deposition parameters for the TiN and TiN/TiCN coatings are summarized in Table 1.

Table 1. Deposition parameters of TiN and TiN/TiCN coatings by DC magnetron sputtering

Coating	Deposition parameters				
	Deposition time, min	Chamber pressure, Pa	Inert and reactive gas flow, L/h	Plasma current, A	Voltage, V
TiN	140	0.4-0.45	Ar = 1.3; N_2 = 0.08	2	530-550
TiN/TiCN-1	140	0.4-0.45	Ar = 1.3; C_3H_8 = 0.31; N_2 = 0.08	2	530-550
TiN/TiCN-2	140	0.4-0.45	Ar = 1.3; C_3H_8 = 0.31; N_2 = 0.08	2	530-550

Surface morphology of the coatings was examined using a JXA-8230 electron microscope (JEOL, Tokyo, Japan). All samples were analyzed in backscattered electron mode (COMPO) at various magnifications. Coatings were deposited on silicon substrates to facilitate cross-sectional thickness measurements.

Nanohardness measurements were conducted using a NanoScan-4D nanohardness tester (Nanoscan, Moscow, Russian Federation). Ten indents were made with a Berkovich indenter under a load of 100 mN. The penetration depth of the indenter into the coating ranged from 350 to 450 nm. The Young's modulus and hardness were determined using the Oliver and Pharr method [11]. Hardness and modulus profiles were plotted based on the obtained data, considering standard deviations.

Tribological properties of the coatings were evaluated using a ball-on-disk configuration on a TRB3 tribometer (CSM Instruments, Peseux, Switzerland) at room temperature under lubricated sliding conditions with ambient humidity of 42%. A Wezzer 80W-90 transmission oil was used as a lubricant. The tribological testing parameters were as follows: sliding speed of 1 cm/s, normal load of 5 N, wear track radius of 5 mm, total sliding distance of 160 m (5000 cycles), and data acquisition frequency of 50 Hz. The test conditions met the international standard DIN 50324 [12]. A 3 mm diameter ball of 100Cr6 bearing steel was used as the counterbody.

3. Results and discussion

Figure 1 presents the surface morphology and coating thickness analysis results of TiN-based coatings obtained by scanning electron microscopy (SEM). All deposited coatings exhibit a uniform and smooth surface morphology, free of visible defects or microcracks. Minor inclusions (nucleation sites) are present, which may be attributed to the deposition process or the formation of microstructural phases. However, their occurrence is minimal and does not significantly impact on the overall morphology of the coatings.

No substantial variations in surface morphology were observed among the different coating types. The graph in the lower right corner of Figure 1 shows the measured thickness values of the coatings. The monolayer TiN coating exhibited a thickness of 4.4 μm, whereas the multilayer TiN/TiCN and TiN/TiCN/TiN/TiCN coatings showed thicknesses of approximately 4.0 μm. This difference is attributed to the higher deposition rate of TiN compared to TiCN under identical magnetron sputtering conditions. Cross-sectional SEM analysis of the monolayer TiN coating revealed a columnar microstructure characteristic of such coatings [13].

The results of nanohardness (H) and Young's modulus (E) measurements for all investigated coatings are presented in Figure 2a. The graph shows that the multilayer coatings exhibit the highest values, with H = 20–23.5 GPa and E = 161–191 GPa. It should be noted that these values reflect surface-level hardness, as the indenter penetration depth was confined to the uppermost layer. Nevertheless, the multilayer structure significantly contributes to surface hardness during nanoindentation due to several mechanisms: interfacial strengthening (Hall–Petch effect at the nanoscale), restriction of dislocation motion, and hardening induced by residual stress accumulation.

Studies [14-16] have demonstrated that alternating layers with differing mechanical properties enhance hardness compared to monolithic coatings. Among all tested samples, the four-layer TiN/TiCN/TiN/TiCN coating showed the highest hardness value of 23.5 GPa, which may be attributed to the optimal combination of TiN and TiCN layers. TiCN further reinforces the coating structure in this case, increasing stiffness and resistance to mechanical deformation [4, 17].

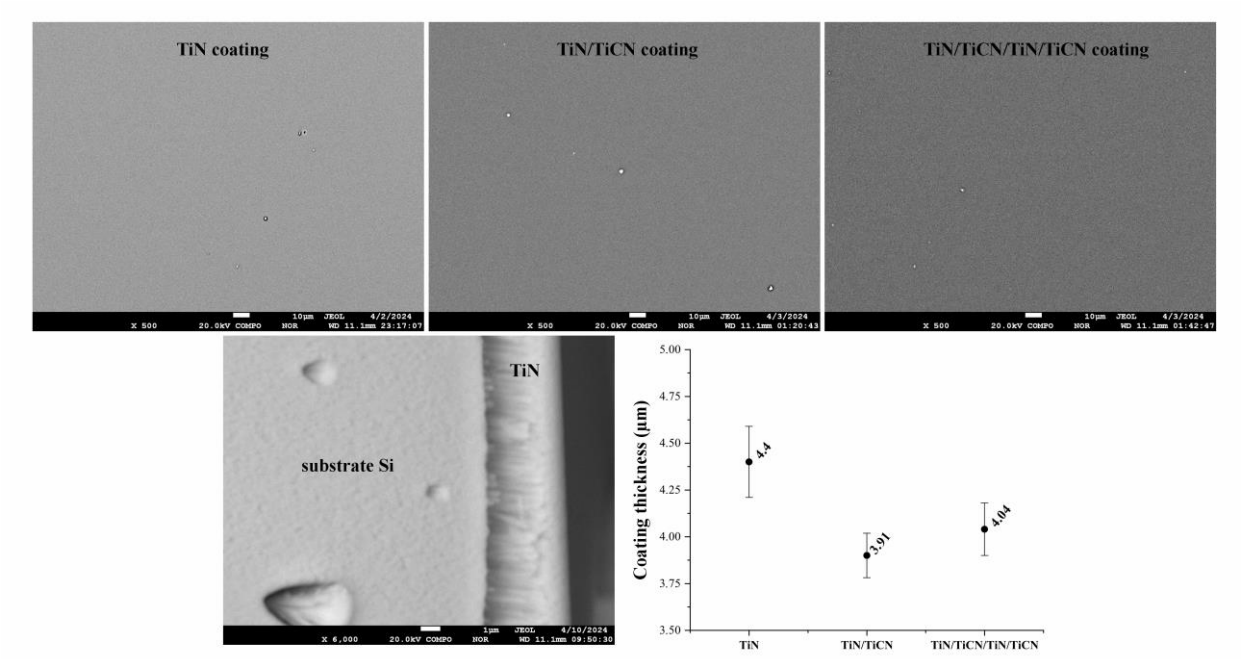

Figure 1. SEM images of surface morphology, cross-sectional view of TiN coating on a silicon substrate, and thickness measurements of the deposited coatings

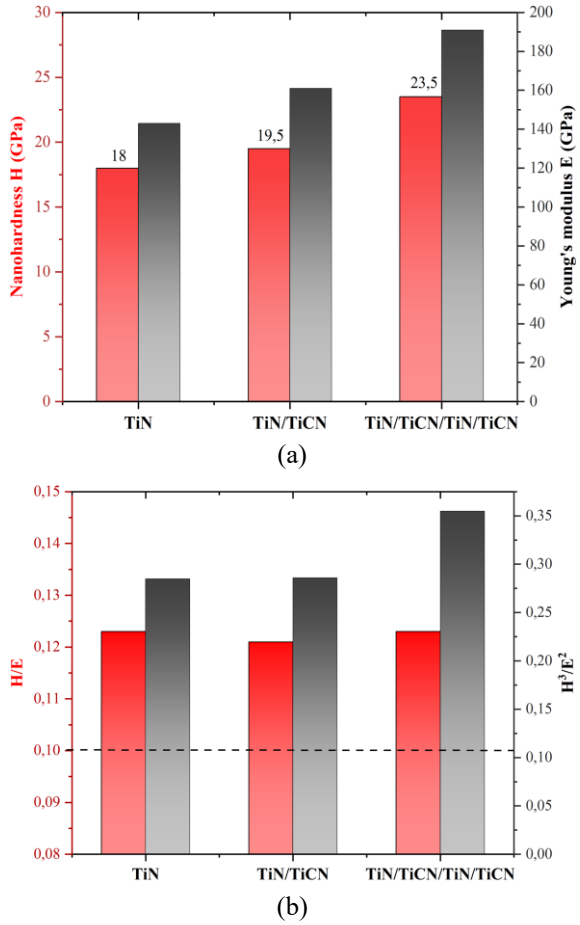

Figure 2. Nanohardness and Young's modulus data of TiN-based deposited coatings

Figure 2b displays the calculated H/E and H^3/E^2 ratios, which are recognized indicators of resistance to mechanical degradation and failure [18]. According to the literature, higher values (H/E > 0.1) are associated with reduced wear rates and lower material loss [19]. From this perspective, all TiN/TiCN/TiN/TiCN multilayer coatings demonstrated the highest H/E and H^3/E^2 values, exceeding the threshold of H/E > 0.1 (indicated by dashed lines), confirming their superior resistance to mechanical failure.

The wear resistance of carbonitride coatings is determined by their microstructure, hardness, and adhesion. These characteristics significantly impact the CoF and WR, which are, in turn, governed by material mass loss during operation [6, 20]. Tribological tests of TiN-based coatings under lubricated sliding conditions revealed low CoF values. This effect can be attributed to a combination of factors: low interfacial adhesion, effective lubrication performance, the possible formation of oxide films, and the high stiffness of TiN all contribute to consistently low CoF under lubrication.

The CoF for all coatings was measured against 100Cr6 steel balls under lubricated conditions. The average CoF was calculated after completing 5000 sliding cycles.

Figure 3 presents the graphs of the CoF with averaged values of all TiN-based coatings deposited on titanium substrates after tribological testing.

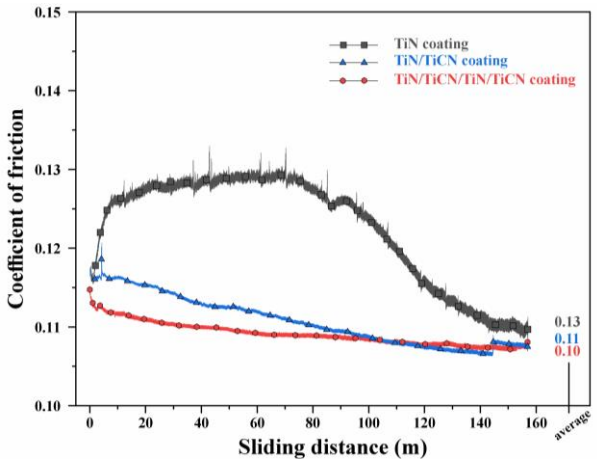

Figure 3. Averaged CoF of the deposited coatings on titanium substrates

According to the results, the average CoF values range from 0.10 to 0.13. Among the tested coatings, monolayer TiN exhibited the highest CoF of 0.13. In contrast, the multilayer coatings demonstrated smoother and lower CoF values than the monolayer TiN coating.

These improved tribological properties are attributed to introducing the TiCN layer, which reduces adhesive friction and enhances load distribution across the coating surface [21, 22]. Incorporating two TiCN layers with differing composition and structure further reduced friction, possibly due to improved crystallinity. These layers may enhance the lubricating behavior of the surface and lower contact resistance, ultimately resulting in minimal friction.

No visible wear tracks were observed on the surfaces of the coatings after tribological tests, which may indicate either minimal material loss or complete wear resistance, as previously reported in studies [23-26].

Thus, the findings of this study confirm that the TiN/TiCN multilayer coatings (both two- and four-layer variants) exhibit significantly higher wear resistance and durability than pure TiN coatings.

4. Conclusions

A comprehensive study was conducted on the mechanical and tribological properties of monolayer TiN and multilayer TiN/TiCN coatings deposited via direct current magnetron sputtering. The main findings are summarized as follows.

SEM analysis revealed that all coatings possess a homogeneous, defect-free microstructure with a characteristic columnar morphology.

Due to interlayer strengthening and dislocation blocking effects, the TiN/TiCN multilayer coatings demonstrated enhanced hardness (up to 23.5 GPa) and elastic modulus (191 GPa) compared to TiN.

Under lubricated sliding conditions, the multilayer TiN/TiCN coatings exhibited significantly lower friction coefficients (0.10–0.13) and superior wear resistance than monolayer TiN. These improved tribological properties are attributed to the optimized layer architecture, reduced adhesion, and formation of protective tribofilms.

No significant wear tracks were observed on the multilayer coatings, confirming their high durability under lubricated friction conditions.

The results confirm that TiN/TiCN multilayer coatings offer superior operational performance to monolayer TiN, making them promising candidates for engineering components subjected to friction and wear. Future work will further optimize layer thickness, interfacial architecture, and deposition parameters to enhance coating performance under real-world operating conditions.

Author contributions

Conceptualization: AKK., AAM., AVP.; Data curation: AKK., BBK; Formal analysis: AKK., AVP.; Funding acquisition: BKK.; Investigation: AKK., AAM., AVP.; Methodology: AKK., BBK; Project administration: BKK.; Resources: BBK; Software: AKK., AVP; Supervision: AAM.; Validation: AAM., AVP.; Visualization: AKK., AAM., AVP.; Writing – original draft: AKK.; Writing – review & editing: AKK. All authors have read and agreed to the published version of the manuscript.

Funding

This research was funded by the Science Committee of the Ministry of Science and Higher Education of the Republic of Kazakhstan (Grant No. BR21882140).

Acknowledgements

The authors are grateful to the National Laboratory for Collective Use of the Institute of Metallurgy and Ore Beneficiation JSC for the analysis of the samples using electron microscopy and X-ray phase analysis. Also, the authors express their sincere gratitude to the Scientific Research Center «Surface Engineering and Tribology» of Sarsen Amanzholov East Kazakhstan University, led by Rakhadilov B. and Sagdoldina Z. for their valuable support, collaboration, and access to advanced experimental facilities, which significantly contributed to the successful completion of this study.

Conflict of interest

The authors declare no conflict of interest.

Data availability statement

The original contributions presented in this study are included in the article. Further inquiries can be directed to the corresponding author.

References

[1] Karar, G.C., Kumar, R. & Chattopadhyaya, S. (2024). Developments on friction surfaced coatings for corrosion, wear-resistant and composite. *Surface Engineering. 41*(1), *8-24.* https://doi.org/10.1177/02670844241293139

[2] Abdulvaliev, R.A., Surkova, T.Y., Baltabekova, Z.A., Yessimova, D.M., Stachowicz, M., Smailov, K.M. & Berkinbayeva, A.N. (2025). Effect of amino acids on the extraction of copper from sub-conditional raw materials. *Kompleksnoe Ispolzovanie Mineralnogo Syra = Complex Use of Mineral Resources, 335(4), 50–58*. https://doi.org/10.31643/2025/6445.39

[3] Yeligbayeva, G., Khaldun, M., Alfergani, A.A., Tleugaliyeva, Z., Karabayeva, A., Bekbayeva, L., Zhetpisbay, D., Shadin, N. & Atabekova, Z. (2024). Polyurethane as a versatile polymer for coating and anti-corrosion applications: A review. *Kompleksnoe Ispolzovanie Mineralnogo Syra = Complex Use of Mineral Resources*, *331*(4), 21–41. https://doi.org/10.31643/2024/6445.36

[4] Shakib, S.E. & Babakhani, A. (2023). Nanomechanical assessment of tribological behavior of TiN/TiCN multi-layer hard coatings deposited by Physical vapor deposition. *Journal of Materials Research and Technology*, *25, 1344-1354.* https://doi.org/10.1016/j.jmrt.2023.05.243

[5] Ospanov, K.K., Smailov, K.M. & Nuruly, Y. (2020). Patterns of non-traditional thermodynamic functions ΔrG⁰/n and Δf($\bar{G}^0$) changes for cobalt minerals. *Chemical Bulletin of Kazakh National University*, *96*(1), 22–30. https://doi.org/10.15328/cb1005

[6] Mamayeva, A.A., Kenzhegulov, A.K., Panichkin, A.V., Kshibekova, B.B. & Bakhytuly, N. (2022). Deposition of carbonitride titanium coatings by magnetron sputtering and its effect on tribo-mechanical properties. *Kompleksnoe Ispolzovanie Mineralnogo Syra = Complex Use of Mineral Resources*, *321*(2), *65-78*. https://doi.org/10.31643/2022/6445.19

[7] Kenzhegulov, A.K., Mamayeva, A.A. & Panichkin, A.V. (2017). Adhesion properties of calcium phosphate coatings on titanium. *Kompleksnoe Ispolzovanie Mineralnogo Syra = Complex Use of Mineral Resources*, *3*, 35-41.

[8] Bakhytuly, N., Kenzhegulov, A., Nurtanto, M., Aliev, A. & Kuldeev, E. (2023). Microstructure and tribological study of TiAlCN and TiTaCN coatings. *Kompleksnoe Ispolzovanie Mineralnogo Syra = Complex Use of Mineral Resources*, *327*(4), 99-110. https://doi.org/10.31643/2023/6445.45

[9] Su, Y.L. & Kao, W.H. (1998). Tribological behavior and wear mechanisms of TiN/TiCN/TiN multilayer coatings. *Journal of Materials Engineering and Performance*, *7*, 601-612. https://doi.org/10.1361/105994998770347440
[10] Kashyap, A., Harsha, A.P., Barshilia, H.C., Bonu, V., Kumar, V.P. & Singh, R. K. (2020). Study of tribological properties of multilayer Ti/TiN coating containing stress-absorbing layers. *Journal of Tribology*, *142*(11), 111401. https://doi.org/10.1115/1.4047195
[11] Galanov, B.A. & Dub, S. (2017). Critical comments to the Oliver–Pharr measurement technique of hardness and elastic modulus by instrumented indentations and refinement of its basic relations. *Journal of Superhard Materials, 39(6), 373-389*. https://doi.org/10.3103/S1063457617060016
[12] DIN 50324. (1992). Tribology; Testing of friction and wear model test for sliding friction of solids (ball on disc system). *German Institute for Standardisation: Berlin, Germany.*
[13] Lapitskaya, V.A., Nikolaev, A., Khabarava, A., Sadyrin, E.V., Antipov, P., Abdulvakhidov, K., Aizikovich, S.M. & Chizhik, S. (2023). The influence of nitrogen flow on the stoichiometric composition, structure, mechanical, and microtribological properties of TiN coatings. *Materials, 17*(1), 120. https://doi.org/10.3390/ma17010120
[14] Zheng, J., Hao, J., Liu, X., Gong, Q. & Liu, W. (2012). A thick TiN/TiCN multilayer film by DC magnetron sputtering. *Surface & Coatings Technology*, *209*, 110-116. https://doi.org/10.1016/j.surfcoat.2012.08.045
[15] Cicek, H. (2018). Wear behaviors of TiN/TiCN/DLC composite coatings in different environments. *Ceramics International*, *44*(5), 4853-4858. https://doi.org/10.1016/j.ceramint.2017.12.074
[16] Lin, Y.W., Chih, P.C. & Huang, J.H. (2020). Effect of Ti interlayer thickness on mechanical properties and wear resistance of TiZrN coatings on AISI D2 steel. *Surface and Coatings Technology*, *394*, 125690. https://doi.org/10.1016/j.surfcoat.2020.125690
[17] Badita-Voicu, L.L., Zapciu, A., Angelescu, D. & Voicu, A.C. (2024). Increasing the wear resistance of hip prostheses components using micro-nanostructured thin layers. *Proceedings of the Institution of Mechanical Engineers, Part C: Journal of Mechanical Engineering Science,* 09544062241242655 https://doi.org/10.1177/09544062241242655
[18] Musil, J. & Jirout, M. (2007). Toughness of hard nanostructured ceramic thin films. *Surface and Coatings Technology*, *201*, 5148-5152. https://doi.org/10.1016/j.surfcoat.2006.07.020
[19] Leyland, A. & Matthews, A. (2000). On the significance of the H/E ratio in wear control: a nanocomposite coating approach to optimized tribological behavior. *Wear*, *246*, 1-11. https://doi.org/10.1016/S0043-1648(00)00488-9
[20] Leitans, A., Jansons, E., Lungevics, J., Kundzins, K., Boiko, I., Kanders, U. & Linins, O. (2023). Tribological and micromechanical properties of the nanostructured carbonitride/nitride coatings of transition metals alloyed by Hf and Nb. *Coatings*, *13*(3), 552. https://doi.org/10.3390/coatings13030552
[21] Guo, D., Zheng, W.S., Huang, T.L., Zhang, S.L., & Guo, F. (2022). Friction and wear properties of multilayer films designed on tantalum substrate. *Materials Science Forum*, *1078*, 121-135. https://doi.org/10.4028/p-l75xgh
[22] Larhlimi, H., Jaghar, N., Lahouij, M., Abegunde, O., Makha, M. & Alami, J. (2024). Effect of carbon content on the tribological behaviour of TiCx coatings prepared by reactive HiPIMS. *International Journal of Refractory Metals and Hard Materials*, *120*, 106599. https://doi.org/10.1016/j.ijrmhm.2024.106599
[23] Wei, C., Lin, J.F., Jiang, T.H. & Ai, C.F. (2001). Tribological characteristics of titanium nitride and titanium carbonitride multilayer films: Part I. The effect of coating sequence on material and mechanical properties. *Thin Solid Films*, *381*(1), 94-103. https://doi.org/10.1016/S0040-6090(00)01540-6
[24] Madej, M., Kowalczyk, J., Ozimina, D. & Milewski, K. (2018). The tribological properties of titanium carbonitride TiCN coating lubricated with non-toxic cutting fluid. *Materials Research Proceedings*, *5*, 47–53. https://doi.org/10.21741/9781945291814-9
[25] Abdulvaliyev, R., Ultarakova, A., Mukangaliyeva, A., Lokhova, N. & Kassymzhanov, K. (2024). Comparative analysis of acid leaching for the efficient recovery of lanthanum and cerium from phosphate. *Separations, 11*, *288.* https://doi.org/10.3390/separations11100288
Zhang, P., Ying, P., Lin, C., Yang, T., Wu, J., Huang, M., ... & Levchenko, V. (2021). Effect of modulation periods on the mechanical and tribological performance of MoS_2–TiL/MoS_2–TiH multilayer coatings. *Coatings*, *11*(10), 1230. https://doi.org/10.3390/coatings11101230

TiN негізіндегі көпқабатты және бірқабатты жабындардың механикалық және трибологиялық қасиеттері

Б.К. Кенжалиев, А.К. Кенжегулов*, А.А. Мамаева, А.В. Паничкин, Б.Б. Кшибекова

Металлургия және кен байыту институты, Алматы, Қазақстан

**Корреспонденция үшін автор: kazakh_1403@mail.ru*

Аңдатпа. Берілген жұмыста тұрақты токты магнетронды бүрку әдісімен титан негізіндегі (ВТ1-0) үлгілерге тұндырылған моноқабатты TiN және көпқабатты TiN/TiCN жабындарының механикалық және трибологиялық қасиеттері зерттелді. Жабындардың микроқұрылымы, наноқаттылығы, серпімділік модулі және майланған үйкеліс жағдайындағы трибологиялық сипаттамалары талданды. Сканерлейтін электрондық микроскопия (СЭМ) нәтижелері барлық жабындардың біртекті және ақаусыз, бағана құрылымды микроструктураға ие екенін көрсетті. Наноиндентация әдісі бойынша алынған мәліметтерге сәйкес, TiN/TiCN көпқабатты жабындарының қаттылығы (23.5 ГПа дейін) мен серпімділік модулі (191 ГПа) моноқабатты TiN-мен салыстырғанда жоғары, бұл қабатаралық беріктену және қалдық кернеулердің қайта бөлінуімен түсіндіріледі. «Шар-диск» схемасы бойынша майланған үйкеліс жағдайында жүргізілген трибологиялық сынақтар көпқабатты жабындардың үйкеліс коэффициентінің (0.1–0.13) төмен екенін және тозуға төзімділігінің жоғары екенін көрсетті. Бұл нәтиже TiCN қабаттарының енгізілуімен байланысты, олар жабын бетінің адгезиясын төмендетіп, жүктеменің біркелкі таралуына және қорғаныштық трибоқабат түзілуіне ықпал етеді. Алынған нәтижелер TiN/TiCN көпқабатты жабындарының механикалық және трибологиялық қасиеттерінің жақсарғанын дәлелдейді және оларды үйкеліс пен тозуға ұшырайтын инженерлік компоненттерде қолдануға болашағы зор екенін көрсетеді.

Негізгі сөздер: *көпқабатты жабын, магнетронды бүрку, үйкеліс коэффициенті, наноқаттылық, тозуға төзімділік.*

Механическое и трибологическое поведение многослойных и однослойных покрытий на основе TiN

Б.К. Кенжалиев, А.К. Кенжегулов*, А.А. Мамаева, А.В. Паничкин, Б.Б. Кшибекова

Институт металлургии и обогащения, Алматы, Казахстан

**Автор для корреспонденции: kazakh_1403@mail.ru*

Аннотация. В данной работе исследованы механические и трибологические свойства монослойных покрытий TiN и многослойных покрытий TiN/TiCN, осажденных методом магнетронного распыления постоянного тока на титановые подложки (ВТ1-0). Проведена их характеристика с точки зрения микроструктуры, нанотвердости, модуля упругости и трибологических характеристик в условиях трения со смазкой. Сканирующая электронная микроскопия (СЭМ) показала, что покрытия имеют однородную микроструктуру без видимых дефектов и характерный столбчатый рост. Испытания методом наноиндентирования продемонстрировали, что многослойные покрытия TiN/TiCN обладают повышенной твердостью (до 23.5 ГПа) и модулем упругости (191 ГПа) по сравнению с монослойным TiN, что объясняется межслойным упрочнением и перераспределением остаточных напряжений. Трибологические испытания по схеме «шар-диск» в условиях смазанного трения показали, что многослойные покрытия демонстрируют значительно меньший коэффициент трения (0.1-0.13) и повышенную износостойкость по сравнению с TiN. Это обусловлено введением слоев TiCN, которые снижают адгезию, способствуют равномерному распределению нагрузки и формированию защитной трибопленки. Полученные результаты подтверждают, что многослойные покрытия TiN/TiCN обладают улучшенными механическими и трибологическими характеристиками, что делает их перспективными для применения в инженерных компонентах, работающих в условиях трения и износа.

Ключевые слова: *многослойное покрытие, магнетронное распыление, коэффициент трения, нанотвердость, износостойкость.*

Publisher's note

All claims expressed in this manuscript are solely those of the authors and do not necessarily represent those of their affiliated organizations, or those of the publisher, the editors and the reviewers.

SATBAYEV UNIVERSITY

Engineering Journal of Satbayev University

Volume 147 (2025), Issue 3, 7-13

https://doi.org/10.51301/ejsu.2025.i3.02

Overview of oxide electrode materials for lithium–ion batteries

M. Dyussembayev[1], S. Yulussov[2], A. Khabiyev[2*], S. Dilibal[3]

[1]*Kazakh-British Technical University, Almaty, Kazakhstan*
[2]*U.A. Joldasbekov Institute of Mechanics and Engineering, Almaty, Kazakhstan*
[3]*Istanbul Gedik University, Istanbul, Turkey*

**Corresponding author: alibek1324@mail.ru*

Abstract. The article discusses the prospects for developing lithium-ion batteries, emphasizing lithium-enriched transition metal oxides used as cathode materials for lithium-ion batteries (LIB). The primary focus is on materials with the formula $xLi_2MnO_3 \cdot (1-x)LiMO_2$ (where M=Mn, Ni, and Co) that exhibit high discharge capacity (over 250 mAh/g) and specific energy (over 950 Wh/kg), surpassing traditional cathode materials such as $LiCoO_2$, $LiMn_2O_4$, and $LiFePO_4$. These oxides combine the monoclinic phase of Li_2MnO_3 and the trigonal phase of $LiMO_2$, which ensures their high performance. However, the authors note several problems, including low speed characteristics, irreversible capacity of the first cycle, and degradation of voltage and capacity during cycling. These problems are linked to the creation of spinel-like structures, unwanted reactions at the surface with the electrolyte, and the release of oxygen. The authors propose modification methods like protective coatings, alloying, and the creation of composite structures to enhance the characteristics. The article also includes an overview of other common cathode materials such as $LiCoO_2$, $LiMn_2O_4$, $LiNiO_2$ and their combinations, highlighting their advantages and limitations. Special attention is paid to promising materials, including $LiNi_{1/3}Co_{1/3}Mn_{1/3}O_2$ and $LiFePO_4$, which have balanced electrochemical and economic properties. It was also emphasised that further research is needed to understand the degradation mechanisms and optimise the structure of lithium-enriched oxides. Resolving these issues can help create better and more reliable cathode materials for LIB, which is crucial for advancing electric vehicles and other energy-intensive technologies.

Keywords: *spent automotive catalysts, rare metals, precious metals, rare earth elements, platinum metals, hydrometallurgical technologies.*

Received: 21 March 2025
Accepted: 15 June 2025
Available online: 30 June 2025

1. Introduction

The history of lithium-ion batteries (LIB) originates in the discoveries of Alessandro Volta and Luigi Galvani in electrochemistry in the early 19th century, which initiated the research of chemical current sources. A significant contribution was made by Michael Faraday, who developed the laws of electrolysis and introduced the term “ion”.

Early rechargeable batteries such as lead-acid, nickel-cadmium, and nickel-iron served as the basis for further development. LIB's commercial breakthrough came in 1990, when Sony introduced batteries with graphite anodes and cathodes from $LiCoO_2$, contributing to the development of electric mobility. Despite the achievements, LIB research continues to improve the materials for the cathode, anode, electrolyte, and other components to increase productivity and reduce cost, as evidenced by the large number of publications and conferences on this topic.

Special attention is paid to cathode materials, where it is necessary to increase the specific capacitance, expand the cycling voltages and ensure stability during long-term cycling. It is essential to find cheaper and environmentally friendly alternatives to the toxic and expensive $LiCoO_2$, which is widely used in industry. $LiMn_2O_4$ spinel is considered a promising cathode material due to its low cost, low toxicity and high thermal stability, especially in the charged state. However, the known disadvantages of $LiMn_2O_4$, such as unsatisfactory cyclability and poor reproducibility, require further research and optimisation, including cationic and anionic doping, changes in stoichiometry, and surface modification.

2. Materials and methods

2.1. Overview of widely used oxide cathode materials of lithium–ion batteries

During the development of cathode materials for lithium-ion batteries (LIB), lithium cobaltate $LiCoO_2$ turned out to be the most effective, which is still widely used in the industrial production of LIB [1]. This compound has a layered structure similar to α-$NaFeO_2$ or the structure of rock salt. The crystal structure of $LiCoO_2$ consists of densely packed layers of cobalt (Co^{3+}) and lithium (Li^+) ions alternating along the (111) plane. Since such an ordering (111) violates the hexagonal symmetry of the lattice, $LiCoO_2$ crystallises in the space group R3m with unit cell parameters a = 2.816 Å and c = 14.08 Å. Figure 1 shows a schematic representation of the crystal structure of $LiCoO_2$, illustrating the layered arrangement of lithium, cobalt, and oxygen atoms.

m.dyussembayev@gmail.com; s1981b@mail.ru; alibek1324@mail.ru; savas.dilibal@gedik.edu.tr
Engineering Journal of Satbayev University. eISSN 2959-2348. Published by Satbayev University

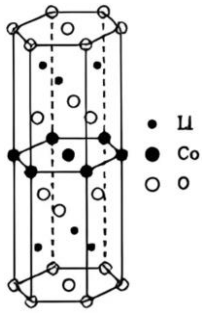

Figure 1. Schematic representation of the $LiCoO_2$ structure [2]

The theoretical capacity of lithium cobaltate ($LiCoO_2$) during electrochemical cycling is 274 mAh/g in the voltage range of 2.5-4.3 V. However, a significant disadvantage of this material is that its practical capacity is theoretically limited since the structure of $Li1–xCoO_2$ is not stable when lithium is deintercalated to $x > 0.5$. This limitation and the high cost of cobalt served as an incentive to search for alternative cathode materials for lithium-ion batteries with higher electrochemical capacity, energy and better resistance to cycling [2]. Lithium-manganese spinel $LiMn_2O_4$ has become one of the successful materials developed. The Li-Mn-O system is more complex than the Co-O system and includes more than ten stable compounds with different structures and degrees of manganese oxidation. Figure 2 shows the isothermal cross-section of the Li–Mn–O phase diagram and an enlarged fragment indicating stoichiometric compositions with rock salt, spinel, and defective spinel structures.

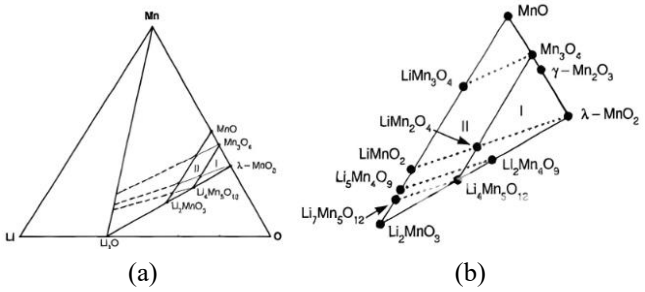

(a) (b)

Figure 2. Isothermal cross-section of the Li–Mn–O phase diagram: (a) – general view of the isothermal section showing phase regions of Li–Mn–O compounds; (b) – enlarged fragment illustrating the location of stoichiometric compositions with rock salt, spinel, and defective spinel structures [3]

The Li-Mn-O system is a complex phase diagram with various stoichiometric and defective spinel structures. The $Mn_3O_4 \cdot Li_4Mn_5O_{12} \cdot \lambda\text{-}MnO_2$ triangle characterises these spinel compositions (Figure 2). The general formula $Laxman_{3-x}O_4$ ($0 \le x \le 1.33$) describes stoichiometric spinel structures located between Mn_3O_4 ($x = 0$) and $Li_4Mn_5O_{12}$ ($x = 1.33$). Manganese oxides with the $Mn_{3-x}O_4$ ($0 \le x \le 1$) defective spinel structure are located between Mn_3O_4 and $\gamma\text{-}MnO_2$.. The lithiated manganese oxides with the defective spinel structure $Li_2O \cdot yMnO_2$ ($y > 2.5$) are located on the line between $Li_4Mn_5O_{12}$ and $\lambda\text{-}MnO_2$, which determines the constant valence of the Mn^{4+} ion. Phases with the structure of rock salt $LizMn_{3-z}O_3$ ($0 \le z \le 2$) are located on the line between MnO ($z = 0$) and Li_2MnO_3 ($z = 2$). The $LiMn_2O_4$ compound initially attracted attention as a cathode material for lithium-ion batteries (LIB), being cheaper and less toxic compared to $LiCoO_2$ [4].

The crystal structure of $LiMn_2O_4$ spinel is a tightly packed cubic anionic lattice, where cations occupy octahedral and tetrahedral positions (Figure 3).

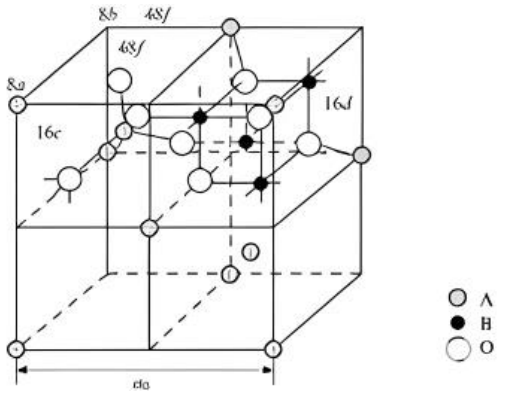

Figure 3. Schematic representation of the spinel structure of type $A[B_2]O_4$ [5]

There are two limiting cation placement options: In normal spinels, A cations are in tetrahedral positions (8a), and B cations are in octahedral positions (16d). Half of the A and B cations in reversed spinels occupy octahedral positions, while the remaining B cations occupy tetrahedral positions. A continuous series of intermediate structures is possible between these variants, allowing cations with different valences to be in various positions. However, one of the disadvantages of $LiMn_2O_4$ is the potential structural rearrangement of spinel into a layered rhombohedral $LiMnO_2$ structure.

One of the disadvantages of $LiMn_2O_4$ as a cathode material for lithium-ion batteries is its relatively low theoretical discharge capacity of 148 mAh/g. At the same time, in practice, this compound can only provide 100-140 mAh/g. On the other hand, lithium nickelate ($LiNiO_2$) was considered a promising cathode material capable of producing about 200 mAh/g. However, its production is fraught with several problems [6].

The $LiNiO_2$ structure, similar to $LiCoO_2$, has a specific setup known as the R3m space group, where lithium and nickel ions are found in octahedral positions 3(a) and 3(b) within a tightly packed cubic arrangement of oxygen. However, there is a fundamental difference between these compounds. The Jahn-Teller effect causes the NiO_6 octahedra to change shape in the nickelate structure because of the Ni^{3+} ions. Also, getting a consistent and correct $LiNiO_2$ composition is difficult because trivalent nickel becomes unstable at high temperatures during the synthesis [7]. Divalent nickel ions take up some of the spots where lithium would generally be in the oxide structure, so the nickelate formula is better expressed as $[Li_{1-z}Ni_z^{2+}]3a[Ni_{1-z}^{3+}Ni_z^{2+}]\ 3b[O_2]\ 6e$. So, for Li_xNiO_2, the structure changes from rhombohedral to monoclinic when the value of x is between 0.4 and 0.75 because of Jahn-Teller distortions and some nickel ions moving to where lithium ions are; at the same time, the rhombohedral structure is present when x is between 0.75 and 1. Also, lithium nickelate breaks down quickly because of reactions with the electrolyte and isn't stable enough when heated, which has restricted its use as a cathode material in industry [8].

Nickel-based compounds show high discharge capacity, like $LiMO_2$-type layered structures with M being Ni, Co, and Mn. Consequently, numerous studies are devoted to creating

cathode materials containing nickel-doped cobalt, manganese, and other metals, which can be easily synthesised and have favourable electrochemical characteristics [9].

The presence of manganese, cobalt, and nickel enhances the thermal stability and structural stabilisation of cathode materials. Based on the study of individual oxides $LiCoO_2$, $LiNiO_2$, and $LiMnO_2$, researchers have developed mixed systems combining oxides of cobalt, nickel, and manganese [10].

Since $LiCoO_2$ and $LiNiO_2$ structures belong to the same spatial group, oxides in the Li-Co-Ni-O system can form almost ideal solid solutions [11]. The $LiNi_yCo_{1-y}O_2$ solid solution was proposed and patented in 1989 as a cathode material. Many compounds containing cobalt and nickel have been studied, including $LiNi_yCo_{1-y}O_2$ $(0 \le y \le 1)$. These metals can synthesize solid solutions in a wide temperature range (500-1000°C). Solid solutions in this system can exist as a layered or spinel structure, depending on the synthesis conditions.

The structure of solid solutions based on $LiNiO_2$ and $LiCoO_2$ is more resistant to lithium deintercalation up to $x = 0.3$ (O_3 type structure), allowing higher capacitance characteristics [12]. However, $LixNiyCo_1–yO_2$ compounds are also characterised by a lower degree of cationic mixing than $LiNiO_2$, with an increase in nickel concentration in $LixNiyCo_1–yO_2$ oxides, the degree of cationic mixing increases, which is associated with the appearance of divalent nickel. Nevertheless, an increase in the nickel content leads to a rise in the specific capacity of solid solutions in the Li–Co–Ni–O system. $LiNiyCo_1–yO_2$ compositions with $y = 0.7$-0.8 are the most effective [13].

Many scientists have studied the various compositions in this system using multiple synthesis methods, such as solid-phase, coprecipitation, variations of the sol-gel process, and others. According to the data analysis, the conditions and method of synthesis significantly impact the size of the formed particles, morphology, texture, density, and final electrochemical properties of the compounds. In addition, studies have been conducted on compounds in the Li-Ni-Co-O system doped with other elements [14].

Some researchers believe that the compound $LiNi_{1/3}Co_{1/3}Mn_{1/3}O_2$ with an exact ratio of components is the most balanced solid solution composition in the LiCoNiMnO system since it has an optimal combination of capacity, power, lifetime, thermal stability, safety and cost [15]. Numerous works devoted to studying this compound continue to arouse scientific interest. Figure 4 shows the model of the crystalline structure of the $LiNi_{1/3}Co_{1/3}Mn_{1/3}O_2$ layered oxide, illustrating the arrangement of transition metal ions and lithium within the layered framework.

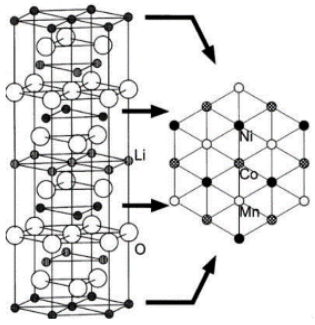

Figure 4. Model of the crystalline structure of the $LiNi1/3Co_{1/3}Mn_{1/3}O_2$ oxide [16]

In addition to the above-mentioned compound $LiNi_{1/3}Co_{1/3}Mn_{1/3}O_2$, there are other compounds in the triad of transition metals nickel, cobalt and manganese that are of industrial interest for use as cathode materials for lithium-ion batteries [17]. The phase diagram of the $LiCoO_2$ - $LiNiO_2$ - $LiMnO_2$ system (Figure 5) shows the compositions used in the industrial production of cathodes for lithium-ion batteries. These compositions are characterised by an optimal combination of electrochemical, structural, and economic parameters, which makes them promising for commercial use as cathode materials.

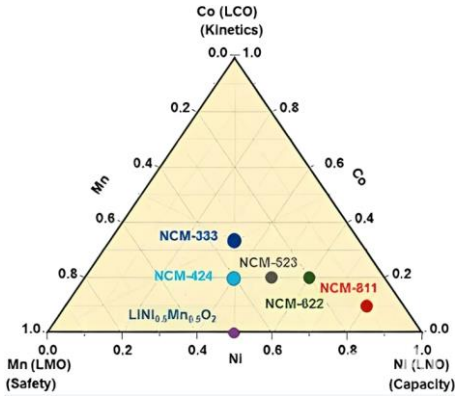

Figure 5. Phase diagram in the triple CO, LMO, LMO system (dots indicate compositions used on an industrial scale [18])

Unlike manganese- and nickel-based cathode materials, lithium iron phosphate ($LiFePO_4$) electrodes with a triphylite structure are characterised by increased structural and thermal stability during lithium ion extraction.

The crystal structure of $LiFePO_4$ belongs to the orthorhombic spatial group Pnma with unit cell parameters $a = 1.033$ nm, $b = 0.601$ nm, and $c = 0.4693$ nm. Figure 6 schematically shows the ideal and real crystal structures of $LiFePO_4$.

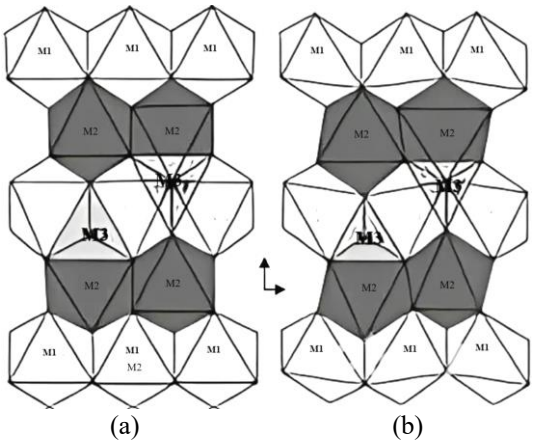

Figure 6. Schematic representation of ideal (a) and real (b) $LiFePO_4$ structures [17]

The $LiFePO_4$ framework structures consist of FeO_6 octahedra and PO_4 tetrahedra touching oxygen vertices in the b-c planes and common edges. The PO_4 tetrahedra are not interconnected. Along the c axis, lithium atoms are located in interstices, forming chains moving along the a-c planes. In the a-c planes, iron atoms form zigzag chains at the vertices of octahedra oriented parallel to the c axis. The iron atoms

occupy the M2 positions, and the lithium atoms occupy the M1 positions. The oxygen structure is a slightly distorted, tightly packed hexagonal structure. Due to the strong covalent P-O bonds forming a three-dimensional delocalised chemical bond system, $LiFePO_4$ retains thermodynamic stability even at temperatures up to 200°C.

Significant efforts by researchers are aimed at improving the electrochemical characteristics of existing cathode materials for lithium-ion batteries. Because the breakdown of cathode materials with reactive nickel starts on their surfaces, creating protective coatings is a key research focus. To enhance how well cathode materials work, researchers commonly use methods like applying coatings, making composites, adding different elements, creating core-shell structures, and other ways to modify them.

Covering the surface of cathode materials makes them more stable and enhances their electrical features, like capacitance, how long they last, and speed. Composite materials made of a cathode compound and conductive additives help boost electronic conductivity and enhance electrochemical features. Doping cathode materials with various elements can modify their structure and redox properties and, as a result, lead to a change in electrochemical behaviour. Core-shell structures are also a promising approach for increasing the stability and improving the characteristics of cathode materials [19, 20].

3. Results and discussion

3.1. Lithium-enriched transition metal oxides with the general formula xLi_2MnO_3 (1-x) $LiMO_2$, (M = Mn, Ni, Co)

A promising direction in the field of cathode materials for lithium-ion batteries is complex lithium oxides of nickel, cobalt and manganese with an excess of lithium compared to the stoichiometry of $LiMO_2$, called “Li-rich” in English literature. These materials were first proposed by a group of researchers led by Michael Thackeray from Argonne National Laboratory [21]. Their structure typically includes two compounds: lithium manganate (Li_2MnO_3), which has a monoclinic shape, and lithium oxide ($LiMO_2$), which has a trigonal shape. The formula of these materials can be represented as $xLi_2MnO_3 \cdot (1-x)LiMO_2$, where $M=Mn_xNi_yCo_z$, $x+y+z=1$, or formally as $Li_{(1+y)}M'_{(1-y)}O_2$ or $Li[Li_yM'_{(1-y)}]O_2$ in excess of lithium.

The main benefits of Li-rich oxides are their ability to store much energy (over 250 mAh/g) compared to other known materials like $LiCoO_2$ (140 mAh/g), $LiMn_2O_4$ (120-140 mAh/g), LiNixCoyMnzO₂ (160 mAh/g), and $LiFePO_4$ (160-170 mAh/g), as well as their high energy output (more than 950 Wh/kg) at an average voltage of 3.5-3.6 V. Additional advantages are their relatively low cost and toxicity due to the reduced content of cobalt and manganese [21].

The Li-rich oxides of the Li_2MnO_3 fraction (monoclinic, pr. C2/m) and $LiMO_2$ (trigonal, pr. R3m) have densely packed face-centred cubic layers with an interlayer distance of about 4.7 Å between the planes (001) in the monoclinic structure of Li_2MnO_3 and (003) in the trigonal structure of $LiMO_2$, which contributes to their interaction.

According to some researchers, the Li_2MnO_3 compound is electrochemically inactive when cycled to a voltage of 4.4 V, which stabilises the structure of the entire material. When cycling to a higher voltage (4.6-4.8 V), a significant increase in the specific capacity of materials is associated with the activation of the monoclinic structure by removing lithium and oxygen, as well as the participation of the oxygen anion (O_2^- O_2n^-) in the redox process. Deeper oxidation and reduction of transition metal cations are also possible. The literature offers various explanations for the abnormally high capacity and the observed decrease in capacity during cycling of Li-rich oxides. Figure 7 presents a schematic comparison of the crystal structures of the monoclinic Li_2MnO_3 phase and the trigonal $LiMO_2$ phase, highlighting their structural differences and layered arrangements.

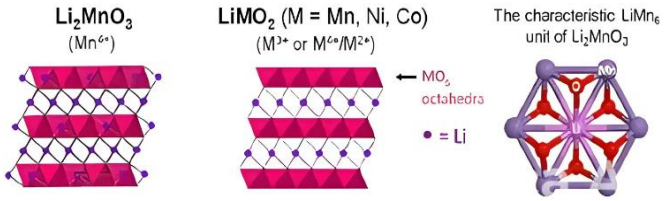

Figure 7. Schematic representation of the structures of the monoclinic phase (Li_2MnO_3) and the trigonal phase ($LiMO_2$) [22]

The key problems associated with using lithium-enriched oxide cathode materials are the reduction of voltage and capacity during cycling, high irreversible capacity on the first cycle, and limited speed characteristics. Despite significant research efforts, no materials that are free of these shortcomings have been found. The reasons for this behaviour of these complex systems have not been definitively established [23]. The formation of spinel-like domains inside the layered phase and side reactions of the surface with the electrolyte and its decomposition products are considered to be one of the factors causing a drop in capacity during cycling. In this case, releasing Li_2O with the formation of oxygen, lithium hydroxide, and carbonate plays a crucial role [24].

As mentioned before, when lithium-enriched oxides are used at high voltage, they change their structure, but we don't fully understand how this happens. The literature emphasises the importance of the initial structure of these materials, but the relationship between the microstructure and its electrochemical properties is currently not completely clear [25]. It also remains unclear whether the lithium-enriched structures are a composite or a solid solution at the nanodomain level. Recent studies using high-resolution transmission electron microscopy and characteristic electron energy loss spectroscopy confirm the existence of a nanodomain structure [26]. The conditions and methods of material synthesis, as well as their composition, are undoubtedly crucial in this matter.

4. Conclusions

In conclusion, it should be noted that the further development of lithium-ion batteries requires close attention to the materials of the positive electrode, particularly to promising lithium-enriched oxides as potential cathode materials. However, the existing disadvantages of these materials, such as limited energy consumption, degradation during cycling, and the complexity of analysing their structures, make their industrial application difficult.

The inconsistency of the data presented in the literature highlights the need for further fundamental research to understand better the influence of various factors on the functional characteristics and performance of lithium-enriched oxides. Identifying ways to improve their performance while reducing degradation during cycling is also necessary. Solv-

ing these problems is an essential prerequisite for the possible industrial introduction of lithium-enriched oxide materials as high-energy cathodes for lithium-ion batteries.

Author contributions

Conceptualization: MD; Data curation: AK; Formal analysis: MD; Funding acquisition: AK, SY; Investigation: SY; Methodology: MD; Project administration: XX, XX; Resources: AK, SY; Software: AK, SD; Supervision: MD, AK; Validation: SY; Visualization: AK, SY; Writing – original draft: AK, SY; Writing – review & editing: SY. All authors have read and agreed to the published version of the manuscript.

Funding

This research was funded by the Science Committee of the Ministry of Science and Higher Education of the Republic of Kazakhstan, grant number BR20280990-OT-24.

Acknowledgements

The authors express their sincere gratitude to the editor and anonymous reviewers for their constructive comments and valuable suggestions, which have significantly improved the quality of this manuscript.

Conflict of interest

The authors declare no conflict of interest.

Data availability statement

The original contributions presented in this study are included in the article. Further inquiries can be directed to the corresponding author.

References

[1] Xiao, B. & Sun, X. (2018). Surface and subsurface reactions of lithium transition metal oxide cathode materials: An overview of the fundamental origins and remedying approaches. *Advanced Energy Materials*, *8*(29), 1802057. https://doi.org/10.1002/aenm.201802057

[2] Kirchartz, T., Márquez, J. A., Stolterfoht, M. & Unold, T. (2020). Photoluminescence-based characterization of Halide perovskites for photovoltaics. *Advanced Energy Materials*, *10*(26), 1904134. https://doi.org/10.1002/aenm.201904134

[3] Wang, J., Wang, Y., Seo, D.-H., Shi, T., Chen, S., Tian, Y., & Ceder, G. (2020). A high-energy NASICON-type cathode material for Na-ion batteries. *Advanced Energy Materials, 10(10), 1903968*. https://doi.org/10.1002/aenm.201903968

[4] Kim, J., Lee, H., Cha, H., Yoon, M., Park, M. & Cho, J. (2018). Prospect and reality of Ni-rich cathode for commercialization. *Advanced Energy Materials,* *8*(6), 1702028. https://doi.org/10.1002/aenm.201702028

[5] Wu, J.-F., Wang, Q. & Guo, X. (2018). Sodium-ion conduction in Na2Zn2TeO6 solid electrolytes. *Journal of Power Sources*, *402*, 513-518. https://doi.org/10.1016/j.jpowsour.2018.09.048

[6] Gam-Derouich, S., Pinson, J., Lamouri, A., Decorse, P., Bellynck, S., Herbaut, R., & Mangeney, C. (2018). Micropatterned anti-icing coatings with dual hydrophobic/hydrophilic properties. *Journal of Materials Chemistry. A, Materials for Energy and Sustainability*, *6*(40), 19353-19357. https://doi.org/10.1039/c8ta06944a

[7] Hannah, D.C., Sai Gautam, G., Canepa, P. & Ceder, G. (2018). On the balance of intercalation and conversion reactions in battery cathodes. *Advanced Energy Materials*, *8*(20), 1800379. https://doi.org/10.1002/aenm.201800379

[8] Sun, Q., Xi, B., Li, J.-Y., Mao, H., Ma, X., Liang, J., & Xiong, S. (2018). Nitrogen-doped graphene-supported mixed transition-metal oxide porous particles to confine polysulfides for lithium-sulfur batteries. *Advanced Energy Materials*, *8*(22), 1800595. https://doi.org/10.1002/aenm.201800595

[9] Yu, X., Zhang, C., Luo, Z., Zhang, T., Liu, J., Li, J., Zuo, Y., Biendicho, J.J., Llorca, J., Arbiol, J., Morante, J.R., & Cabot, A. (2019). A low temperature solid state reaction to produce hollow MnxFe3-xO4 nanoparticles as anode for lithium-ion batteries. *Nano Energy*, *66*, 104199. https://doi.org/10.1016/j.nanoen.2019.104199

[10] Li, Y.B., Li, T., Dai, X.C., Huang, M.H., Hou, S., Fu, X.Y., Wei, Z.Q., He, Y., Xiao, G., & Xiao, F.X. (2020). Precise tuning of coordination positions for transition-metal ions via layer-by-layer assembly to enhance solar hydrogen production. *ACS Applied Materials & Interfaces*, *12*(4), 4373-4384. https://doi.org/10.1021/acsami.9b14543

[11] Goodenough, J.B., & Singh, P. (2015). Review – solid electrolytes in rechargeable electrochemical cells. *Journal of the Electrochemical Society*, *162*(14), A2387-A2392. https://doi.org/10.1149/2.0021514jes

[12] Shin, J.A., Jin, E.M., Na, B.K., Gu, H.B., Wang, W.L. & Jeong, S.M. (2016). Facile preparation and electrochemical properties of carbon-enfolded sulfur particles for Li-S battery application. *Journal of the Electrochemical Society*, *163*(2), A57-A61. https://doi.org/10.1149/2.0031602jes

[13] Huang, B., Pan, Z., Su, X. & An, L. (2018). Recycling of lithium-ion batteries: Recent advances and perspectives. *Journal of Power Sources*, *399*, 274-286. https://doi.org/10.1016/j.jpowsour.2018.07.116

[14] Braga, M.H., Grundish, N.S., Murchison, A.J. & Goodenough, J.B. (2017). Alternative strategy for a safe rechargeable battery. *Energy & Environmental Science*, *10*(1), 331-336. https://doi.org/10.1039/c6ee02888h

[15] Ulvestad, A., Mæhlen, J.P., & Kirkengen, M. (2018). Silicon nitride as anode material for Li-ion batteries: Understanding the SiNx conversion reaction. *Journal of Power Sources*, *399*, 414-421. https://doi.org/10.1016/j.jpowsour.2018.07.109

[16] Huang, B., Pan, Z., Su, X., & An, L. (2018). Recycling of lithium-ion batteries: Recent advances and perspectives. *Journal of Power Sources*, *399*, 274-286. https://doi.org/10.1016/j.jpowsour.2018.07.116

[17] Yang, W. & Devereaux, T.P. (2018). Anionic and cationic redox and interfaces in batteries: Advances from soft X-ray absorption spectroscopy to resonant inelastic scattering. *Journal of Power Sources*, *389*, 188-197. https://doi.org/10.1016/j.jpowsour.2018.04.018

[18] Liu, J., Zhang, C., Guo, S., Xu, L., Xiao, S. & Shen, Z. (2019). Microwave treatment of pre-oxidized fibers for improving their structure and mechanical properties. *Ceramics International*, *45*(1), 1379-1384. https://doi.org/10.1016/j.ceramint.2018.08.311

[19] Ming, F., Liang, H., Lei, Y., Zhang, W. & Alshareef, H. N. (2018). Solution synthesis of VSe2 nanosheets and their alkali metal ion storage performance. *Nano Energy*, *53*, 11-16. https://doi.org/10.1016/j.nanoen.2018.08.035

[20] Le Mong, A. & Kim, D. (2019). Solid electrolyte membranes prepared from poly(arylene ether ketone)-g-polyimidazolium copolymer intergrated with ionic liquid for lithium secondary battery. *Journal of Power Sources*, *422*, 57-64. https://doi.org/10.1016/j.jpowsour.2019.03.038

[21] Che, H., Liu, C., Che, G., Liao, G., Dong, H., Li, C., Li, C. (2020). Facile construction of porous intramolecular g-C_3N_4-based donor-acceptor conjugated copolymers as highly efficient photocatalysts for superior H2 evolution. *Nano Energy*, *67*, 104273. https://doi.org/10.1016/j.nanoen.2019.104273

[22] Liu, S., Rasinski, M., Rahim, Y., Zhang, S., Wippermann, K., Reimer, U. & Lehnert, W. (2019). Influence of operating conditions on the degradation mechanism in high-temperature polymer electrolyte fuel cells. *Journal of Power Sources*, *439*, 227090. https://doi.org/10.1016/j.jpowsour.2019.227090

[23] Dong, L., Zhang, L., Lin, S., Chen, Z., Wang, Y., Zhao, X., Wu, T., Zhang, J., Liu, W., Lu, H., & Loh, K. P. (2020). Building vertically-structured, high-performance electrodes by interlayer-confined reactions in accordion-like, chemically expanded graphite. *Nano Energy*, *70*, 104482. https://doi.org/10.1016/j.nanoen.2020.104482

[24] Billo, T., Shown, I., Anbalagan, A. K., Effendi, T.A., Sabbah, A., Fu, F.Y., Chu, C.M., Woon, W.Y., Chen, R.S., Lee, C.H., Chen, K.H., & Chen, L.C. (2020). A mechanistic study of molecular CO_2 interaction and adsorption on carbon implanted SnS2 thin film for photocatalytic CO_2 reduction activity. *Nano Energy*, *72*, 104717. https://doi.org/10.1016/j.nanoen.2020.104717

[25] Hu, X., Jiang, Z., Yan, L., Yang, G., Xie, J., Liu, S., Zhang, Q., Xiang, Y., Min, H., & Peng, X. (2020). Real-time visualized battery health monitoring sensor with piezoelectric/pyroelectric poly (vinylidene fluoride-trifluoroethylene) and thin film transistor array by in-situ poling. *Journal of Power Sources*, *467*, 228367. https://doi.org/10.1016/j.jpowsour.2020.228367

[26] Rao, K.K., Lai, Y., Zhou, L., Haber, J.A., Bajdich, M., & Gregoire, J.M. (2022). Overcoming hurdles in oxygen evolution catalyst discovery via codesign. *Chemistry of Materials: A Publication of the American Chemical Society*, *34*(3), 899-910. https://doi.org/10.1021/acs.chemmater.1c04120

Литий-ионды аккумуляторларға арналған оксидті электрод материалдарына шолу

М.Ш. Дюсембаев[1], С.В. Юлусов[2], А.Т. Хабиев[2*], С. Дилибал[3]

[1]*Қазақстан-Британ техникалық университеті, Алматы, Қазақстан*
[2]*Ө.А. Жолдасбеков атындағы Механика және машинатану институты, Алматы, Қазақстан*
[3]*Ыстамбұл Гедик университеті, Стамбул, Түркия*

**Корреспонденция үшін автор: alibek1324@mail.ru*

Аңдатпа. Мақалада литий-ионды аккумуляторлардың (ЛИА) даму перспективалары қарастырылады, атап айтқанда, катодты материалдар ретінде қолданылатын литийге бай ауыспалы металл оксидтеріне баса назар аударылады. Негізгі назар $xLi_2MnO_3 \cdot (1-x)LiMO_2$ (мұндағы M = Mn, Ni, Co) формулалы материалдарға аударылған, олар жоғары разрядтық сыйымдылықпен (250 мА·сағ/г-дан астам) және меншікті энергиямен (950 Вт·сағ/кг-нан жоғары) ерекшеленеді, бұл оларды дәстүрлі катодты материалдар — $LiCoO_2$, $LiMn_2O_4$ және $LiFePO_4$-пен салыстырғанда тиімдірек етеді. Бұл оксидтер Li_2MnO_3-тің моноклиндік фазасы мен $LiMO_2$-нің тригональды фазасын біріктіріп, жоғары өнімділікке қол жеткізеді. Алайда, авторлар бірқатар мәселелерге назар аударады: төмен жылдамдық сипаттамалары, алғашқы циклдағы қайтымсыз сыйымдылық және циклдік жұмыс барысында кернеу мен сыйымдылықтың төмендеуі. Бұл кемшіліктер шпинель тәрізді құрылымдардың түзілуімен, электролитпен шекарада жанама реакциялармен және оттектің бөлінуімен байланысты. Мұндай кемшіліктерді жою үшін қорғаныс жабындарын қолдану, легирлеу және композиттік құрылымдар жасау сияқты модификациялау әдістері ұсынылады. Мақалада сондай-ақ кеңінен қолданылатын басқа катодты материалдарға — $LiCoO_2$, $LiMn_2O_4$, $LiNiO_2$ және олардың комбинацияларына шолу жасалып, олардың артықшылықтары мен шектеулері талданады. Әсіресе, $LiNi1/3Co1/3Mn1/3O_2$ және $LiFePO_4$ сияқты перспективалы материалдарға ерекше көңіл бөлінген, себебі олар электрохимиялық және экономикалық тұрғыдан оңтайлы қасиеттерге ие. Сондай-ақ литийге бай оксидтердің құрылымын оңтайландыру және деградация механизмдерін тереңірек түсіну үшін қосымша зерттеулердің қажеттілігі атап өтілген. Бұл мәселелерді шешу ЛИА үшін жоғары тиімді әрі тұрақты катодты материалдарды әзірлеуге мүмкіндік беріп, электромобильділік пен басқа да энергияны көп қажет ететін технологиялардың дамуына ықпал етуі мүмкін.

Негізгі сөздер: *литий-ионды аккумуляторлар, катодты материалдар, литиймен байытылған оксидтер, Lerich оксидтері.*

Обзор по оксидным электродным материалам для литий-ионных аккумуляторов

М.Ш. Дюсембаев[1], С.В. Юлусов[2], А.Т. Хабиев[2*], С. Дилибал[3]

[1]*Казахстанско-Британский технический университет, Алматы, Казахстан*
[2]*Институт механики и машиноведения имени академика У.А. Джолдасбекова, Алматы, Казахстан*
[3]*Стамбульский Гедик университет, Стамбул, Турция*

**Автор для корреспонденции: alibek1324@mail.ru*

Аннотация. В статье рассматриваются перспективы развития литий-ионных аккумуляторов с акцентом на литий-обогащённые оксиды переходных металлов, используемых в качестве катодных материалов для литий-ионных аккумуляторов (ЛИА). Основное внимание уделяется материалам с формулой $xLi_2MnO_3 \cdot (1-x)LiMO_2$ (где M=Mn, Ni, Co), которые демонстрируют высокую разрядную ёмкость (более 250 мА·ч/г) и удельную энергию (свыше 950 Вт·ч/кг), превосходя традиционные катодные материалы, такие как $LiCoO_2$, $LiMn_2O_4$ и $LiFePO_4$. Эти оксиды сочетают в себе

моноклинную фазу Li_2MnO_3 и тригональную фазу $LiMO_2$, что обеспечивает их высокую производительность. днако авторы отмечают ряд проблем, включая низкие скоростные характеристики, необратимую ёмкость первого цикла и деградацию напряжения и ёмкости при циклировании. Эти недостатки связаны с образованием шпинелеподобных структур, побочными реакциями на границе с электролитом и выделением кислорода. Для улучшения характеристик предлагаются методы модификации, такие как защитные покрытия, легирование и создание композитных структур. В статья также включен обзор других распространённых катодных материалов, таких как $LiCoO_2$, $LiMn_2O_4$, $LiNiO_2$ и их комбинации, подчёркивая их преимущества и ограничения. Особое внимание уделяется перспективным материалам, включая $LiNi1/3Co1/3Mn1/3O_2$ и $LiFePO_4$, которые обладают сбалансированными электрохимическими и экономическими свойствами. Также было подчёркнута необходимость дальнейших исследований для понимания механизмов деградации и оптимизации структуры литий-обогащённых оксидов. Решение этих задач может способствовать разработке высокоэффективных и стабильных катодных материалов для ЛИА, что важно для развития электромобильности и других энергоёмких технологий.

Ключевые слова: *литий-ионные аккумуляторы, катодные материалы, обогащенные литием оксиды, Lerich оксиды.*

Publisher's note

All claims expressed in this manuscript are solely those of the authors and do not necessarily represent those of their affiliated organizations, or those of the publisher, the editors and the reviewers.

SATBAYEV UNIVERSITY

Engineering Journal of Satbayev University

Volume 147 (2025), Issue 3, 14-19

https://doi.org/10.51301/ejsu.2025.i3.03

Features of mineral formation in the structure of iron ore materials from the position of the state diagram of the system $CaO–Fe_2O_3–SiO_2$

A. Zhunusova[1], P. Bykov[1], A. Zhunusov[1*], O. Zayakin[2], A. Bakirov[1], A. Kenzhebekova[1]

[1]*Toraighyrov University, Pavlodar, Kazakhstan*

[2]*Institute of Metallurgy of the Ural Branch of the Russian Academy of Sciences, Yekaterinburg, Russia*

**Corresponding author: zhunusov_ab@mail.ru*

Abstract. This paper presents the results of a study of the strengthening of iron ore raw materials obtained by oxidative roasting of granules and pellets using gaseous fuel and agglomeration with combustion of solid fuel in the agglomeration layer. Differences in the mechanisms of mineral formation of granules, pellets and agglomerates appear at the stage of liquid-phase strengthening and are due to the different role of iron in forming the strengthening melt. At the same time, in the agglomerate, granules and pellets, iron is in different valence states, affecting the processes' features. Iron can be in a trivalent state in the iron-silicate melt of granules and pellets and is not a silicate-forming component of the charge. The silicate compositions of the binders in the entire studied range of basicities (0.3-1.5) are located along the line of the $CaO–SiO_2$ connection, which is determined using the phase diagram of the $CaO–Fe_2O_3–SiO_2$ system. During agglomeration, the silicon-containing melt is formed under conditions of excess FeO, which directs the process of mineral formation during the creation of the iron-silicate binder of the agglomerate. Under standard agglomeration conditions, silicate binders with a basicity of 1.0-1.5 are formed in the olivine field of the $CaO–FeO–SiO_2$ phase diagram, covering a wide range of compositions. The processes of mineral formation in batches, by hardened methods, both during the firing of granules, pellets, and during agglomeration, have shown that changing the oxidation potential of the gas phase is an effective lever on the path not only to improving the properties of ferrous sand - a waste product of alumina production, but also to creating both new binders and new types of iron ore raw materials suitable for smelting ferrosilicon.

Keywords: *ferrous sand, agglomeration, sintering, iron ore agglomerate, fluxes.*

Received: 24 March 2025
Accepted: 15 June 2025
Available online: 30 June 2025

1. Introduction

Alumina is known to be produced from bauxite using the Bayer sintering method [1]. These methods produce a large amount of sludge. One of these sludges is called waste (red) sludge. According to sources [2, 3], 0.9 to 1.5 tons of red mud are produced from bauxite for every ton of alumina. To date, red mud has no further use and is stored in sludge fields. The latter occupy vast territories and cause enormous harm to the environment. Such sludge fields occupy 10 to 50 hectares and store millions of tons of waste [4].

Some sources report that between 2.0 billion [5] and 4.0 billion tons of alumina production waste [6] have accumulated worldwide, and vast amounts of money are spent on maintaining such sludge storage facilities. According to [7] alone, the Ural alumina refineries in Russia have accumulated 100-300 million tons of waste.

Alumina production sludge contains a high amount of alkali and therefore poses a danger to the environment. The disaster in Hungary in 2010 (Kolontar) is well known. As a result of a dam break, about 700 thousand tons of sludge were released. People and wildlife suffered, and houses were destroyed [8].

To date, various works on red mud processing have been presented worldwide. However, not all studies conducted are of interest from the metallurgical engineering perspective. Many red mud processing technologies are distinguished by the high cost of implementing the presented studies, and most of them are accompanied by complex and multi-stage processing. Red mud, by its composition, can be used in various areas of industry. The work [9] presents multiple options for using red mud in different sectors. The presented studies consider pyrometallurgical, hydrometallurgical methods, direct use of red mud, and catalysts in the chemical industry. For example, in [10], the processing of red mud is approached critically. In [11], it is proposed to use red mud as a filter for water purification. In [12], it is proposed to subject red mud to pyrometallurgical processing and use it as a building material.

At JSC Aluminum of Kazakhstan, about one million tons of waste sludge accumulates yearly in waste dumps. A significant part of the waste sludge is considered substandard and used only in highway construction as bulk material. As is known, the bauxite deposits of Kazakhstan are distinguished by a large amount of iron and silicon. Therefore, ferrous sands with a

zhunusova.aig@mail.ru; Bykov_petr@mail.ru; zhunusov_ab@mail.ru; zferro@mail.ru; altynsary@mail.ru; kenzhebekova_psu@mail.ru
Engineering Journal of Satbayev University. eISSN 2959-2348. Published by Satbayev University

Fe_2O_3 content of 50-65% are separated at the first stage of bauxite processing by the leaching method. These ferrous sands are sent according to the general scheme to sludge fields and do not find further use. As a result, together with the remains of red and gray sludge, ferrous sands lose their value as iron ore material, mixing with other sludges.

Regarding iron oxide, approximately 10 million tons are already irretrievably lost. Let's consider the iron content in ferrous sands, which are sent to the sludge field in approximately 500 thousand tons per year, as substandard material. This situation is only in Kazakhstan. And according to [13], over 2.7 billion tons of bauxite waste have accumulated worldwide, increasing by 120 million tons annually. However, due to their physical and chemical properties, ferrous sands are suitable for inclusion in metallurgical processing. From this material, it is possible to obtain granules, pellets and agglomerates for use in producing ferrosilicon and other alloys (cast iron and steel). For example, in ferrosilicon production, the obtained granules are quite suitable as a substitute for iron shavings.

When using waste for smelting metals and alloys, two problems are solved: including accumulated waste in metallurgical processing in the form of a semi-finished product and reducing the environmental burden. Ferrosilicon can be obtained by reducing the silicon contained in the studied ferruginous sand and the obtained iron ore agglomerate by over 13%. The need to include iron ore agglomerate in the charge is explained by the fact that oxygen compounds of iron at relatively low temperatures can easily interact with SiO_2 to form silicate melts. The theoretical temperature of silicon reduction by carbon according to the reaction $SiO_2 + 2C = Si + 2CO$ is 1669°C, and the eutectic temperature is 1178°C in the $FeO-SiO_2$ system. When using iron ore materials in the charge during the smelting of ferrosilicon, the processes of melting the charge, rather than reduction, are advanced. With the appearance of silicate melts in the bath of the ferroalloy furnace, the specific electrical resistance of the charge sharply decreases, its components stratify, and silicate slag accumulates, which leads to a breakdown in the furnace operation. Therefore, in connection with the process theory, it is necessary to use the appropriate material that meets the requirements of electric smelting. For this, a thorough study of the mineral formation processes occurring during high-temperature firing in the materials under study (granules, pellets and agglomerates) is necessary.

2. Materials and methods

To work with ferrous sands - waste from alumina production, samples were taken at JSC «Aluminium of Kazakhstan» to obtain iron ore agglomerate in laboratory conditions, in which the optimal parameters for sintering ferrous sands were developed [14] (Figure 1).

Figure 1. Ferrous sands - waste from alumina production

Also, in the course of the research, a thermodynamic analysis of the phase formation processes during agglomeration was carried out using the state diagrams of the $FeO-CaO-Fe_2O_3-Al_2O_3$ and $FeO-MgO-Fe_2O_3-Al_2O_3$ systems and the effect of dolomite additives in the composition of the sinter batch was studied, which made it possible to determine the optimal amount of magnesium oxide in the batch and identify new phases [15]. The chemical composition of ferrous sands and the resulting iron ore agglomerate are given in Table 1.

Table 1. Chemical composition of the samples studied

№	Materials	Fe_{gen}	Fe_2O_3	FeO	SiO_2	Al_2O_3	CaO	MgO	S	P	ppp
1	Ferrous sand is a waste product of alumina production	31.62	56.78	9.18	6.25	12.16	2.54	1.62	1.12	0.064	12.57
2	Iron ore agglomerate (Basicity 1.2)	55.6	31.33	28.9	13.28	6.58	16.5	3.62	0.86	0.13	3.18

The chemical composition of ferruginous sands was determined by X-ray fluorescence analysis on a portable Prospector 2 LE X-ray fluorescence spectrometer (Figure 2) with a measurement range of chemical elements from Mg to U in the range up to 0.01 %.

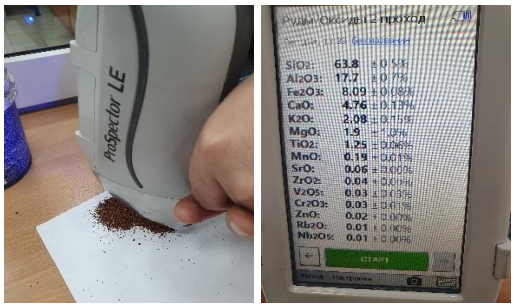

Figure 2. X-ray fluorescence analysis of ferruginous sands

Figure 3 shows samples of iron ore pellets and agglomerate obtained from ferrous sand and waste from alumina production. Optical microscopy in reflected light using a metallographic inverted microscope, METAM LV-32, was used to study the morphology of the agglomerate samples (Figure 4).

(a) (b)

Figure 3. Iron ore pellets (a), iron ore agglomerate (b)

Figure 4. Metallographic inverted microscope METAM LV-32

The micrographs reveal structural features and surface texture characteristic of the sintered phases present in the samples.

3. Results and discussion

In industrial conditions, the main processes of strengthening iron ore raw materials are oxidative roasting granules and pellets using gaseous fuel and agglomeration with solid fuel combustion in the agglomeration layer. Under real roasting conditions, fluxed pellets and agglomerates undergo a similar path of phase transformations at the stage of solid-phase sintering until the appearance of a liquid phase. This path includes dehydration, dissociation and amorphization of minerals of host rocks, as well as decomposition of fluxes with the formation of ferrites.

Differences in the mechanisms of mineral formation of granules, pellets and agglomerates appear at the stage of liquid-phase strengthening and are due to the different role of iron in forming the strengthening melt. In this case, in the agglomerate and pellet, iron is in different valence states, which affects the features of the processes. In the iron-silicate melt of granules and pellets, iron is in a trivalent state and is not a silicate-forming component of the charge. The silicate compositions of the binders in the entire studied range of basicities (0.3-1.5) are located along the $CaO–SiO_2$ bond line, which is visible in the phase diagram of the $CaO–Fe_2O_3–SiO_2$ system. According to the diagram shown in Figure 5, the compositions of the silicate binders are in the crystallization region of iron-free mineral phases: cristobalite (SiO_2), wollastonite ($CaSiO_3$), rankinite ($Ca_3Si_2O_7$) and dicalcium silicate (Ca_2SiO_4). In real pellet compositions, trivalent iron enters the melt from calcium ferrites, which are formed at the solid-phase sintering stage and are the primary source of the strengthening melt.

In the zone of maximum temperatures, the finely dispersed fraction of hematite contained in ferruginous sand passes into a melt. When the pellets are cooled under the existing technological firing mode conditions, the melt solidifies predominantly in a glassy form, retaining some of the iron in the trivalent state. A batch of pellets was produced to compare the processes of mineral formation in pellets and agglomerates made from ferruginous sand. However, difficulties associated with pelletizing ferruginous sand arose during their production, since, according to the theory of pelletizing [16-18], the most unfavorable effect on the process is exerted by the particle size in the range of 0.1-1.6 mm.

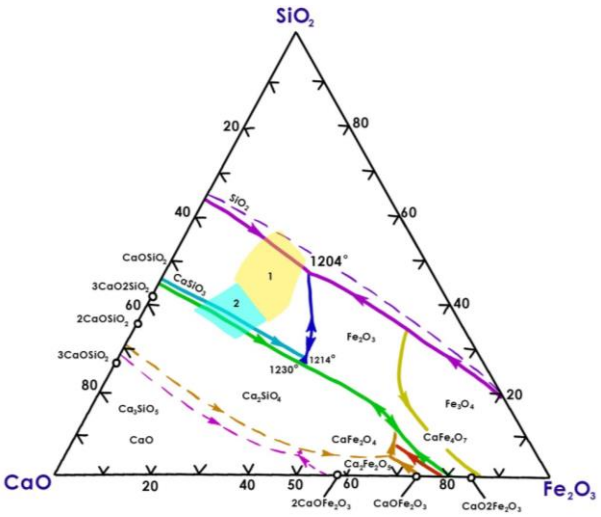

Figure 5. Phase diagram of the CaO - Fe_2O_3 - SiO_2 system. Location of composition areas of silicate binders of fluxed pellets: 1 – compositions providing high strength during reduction of pellets with a SiO_2 content of more than 5%; 2 – the same, with a SiO_2 content of less than 5% [17]

As the data in Table 2 shows, the fractional composition of the studied ferruginous sand corresponds to this range. In this case, the bulk of the ferruginous sand falls on the fraction of 0.2-1.0 mm, making up 63.7% of the total volume.

Table 2. Granulometric composition of ferruginous sands

Fraction, mm	-0.06	-0.2-0.06	-0.5-0.2	-1-0.5	-3-1	-5-3
Units of measurement, %	2.0	14.7	43.2	20.5	6.8	12.8

Finely dispersed iron-containing aspiration dust generated in steelmaking was used to improve the conditions for pelletizing ferruginous sands. The resulting pellets were subjected to firing. During pellet firing at temperatures below the solidus point in air, complete crystallization of the glassy phase occurred with the release of iron in the form of hematite and the formation of iron-free silicate phases. Their composition depended on the basicity of the pellets and corresponded to the crystallization region in the $CaO–SiO_2$ binary system.

During agglomeration, the silicon-containing melt is formed under conditions of excess FeO, which directs the process of mineral formation during the creation of the iron-silicate bond of the agglomerate. Under standard agglomeration conditions, silicate bonds with a basicity of 1.0-1.5 are formed in the olivine field of the $CaO–FeO–SiO_2$ phase diagram, covering a wide range of compositions adjacent to the crystallization region of dicalcium silicate.

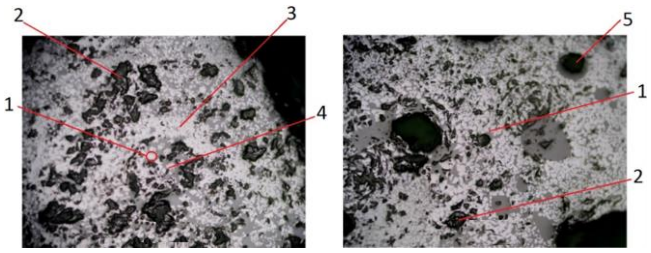

Figure 6. General view of the microstructure of the agglomerate (a, b) x100: 1 – magnetite; 2 – wustite; 3 – magnesia; 4 – hercynite; 5 – pores

Based on Figure 6, it can be noted that the content of non-metallic impurities in magnetite of one genetic variety of iron ore agglomerate remained relatively stable within a specific volume of the sintering batch, but varied significantly at different levels of the sintering cake. The stability of the composition is explained by the fact that only those components of the batch that are within a specific elementary volume are involved in the process of solid solution formation. At the same time, fluctuations in the content of impurities in magnetite of different genetic varieties along the height of the cake are due to the temperature and heat regime of sintering and the amount of liquid phase formed at each level of the sintering batch.

An example is the transformation of grains of the original magnetite into a solid solution of hercynite $FeAl_2O_4$ in magnetite. By analyzing the distribution of zones with different compositions, it is possible to indirectly estimate the state of the ore material in the roasting zone. The composition of the olivine phase in each specific case is determined by the basicity of the melt and the content of divalent iron, which affects its change from calcium-iron olivine, known as ferromonicellite ($CaFeSiO_4$), to ferrous olivine, or fayalite ($FeSiO_4$) [17]. In melts that have been fluxed, the composition does not reach the fayalite phase (Fe_2SiO_4). The maximum content of the fayalite component in the olivine phase can be up to 80%, with 56.5% FeO present in the melt and a minimum melting point of 1130°C, which is confirmed by the data presented in Figure 7. Ferromonticellite and fayalite are two low-temperature phases in the olivine class, with melting points of 1208°C and 1205°C, respectively. Between them, there is a continuous series of solid solutions with a minimum temperature of 1120°C. This corresponds to a composition containing 80% fayalite in a solid solution.

Suppose the melt at the maximum temperatures of the agglomeration process contains high concentrations of divalent iron, which is released as an oxide phase when the agglomerate cools. In that case, its final composition is determined by the oxidation potential of the gas phase.

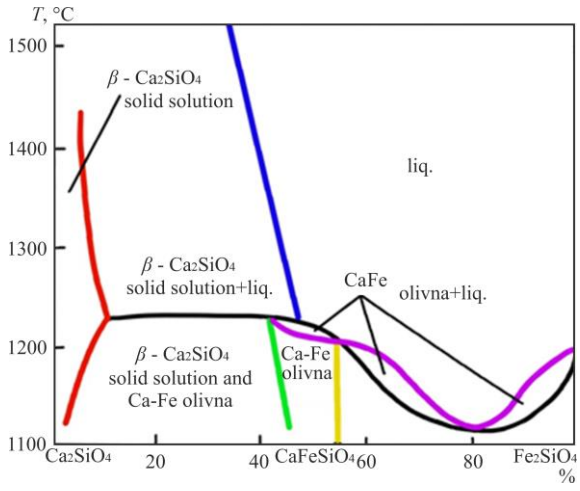

Figure 7. Section of the $CaSiO_4$ - $FeSiO_4$ system [17]

In raw materials of a more complex composition, containing oxides of aluminum contained in ferruginous sands (Table 1) and magnesium, the role of these impurities in forming raw materials is primarily determined by the technological parameters of strengthening [19]. Aluminum oxide, during the firing of pellets, is a component of the binding phases. With different basicity of silicate melts, Al_2O_3 will be part of the ferrite phases or glass. In the composition of silicate binders, Al_2O_3 is an acidic oxide and plays the same role as silica, leading to a decrease in the basicity of the binder. Al_2O_3 is part of the ore, ferrite, and silicate phases during agglomeration. The proportion of aluminum in the composition of various phases at the time of agglomerate formation. The lower the oxidation potential of the gas phase, the more iron oxide and Al_2O_3 in the system in the form of a hercynite solid solution $FeAl_2O_3$ in the magnetite component of the agglomerate. At a high oxidation potential of the gas phase, aluminum remains predominantly in ferrite and silicate phases. The formation of hercynite in a solid solution of magnetite was studied in [18].

4. Conclusions

Magnesium oxide in granules and pellets obtained by oxidative roasting at the stage of liquid-phase strengthening is a source of FeO. Depending on the basicity of the pelletized material, magnesium oxide, together with FeO, is consumed for the construction of silicate phases at a basicity of $CaO/SiO_2 = 0.3$-0.7. It is part of the magnetite solid solution (Fe, Mg) Fe_2O_4, which is formed at the contact of hematite with a magnesium-containing silicate melt at a basicity of pellets above 0.7. Magnesium oxide in pellets leads to the dissociation of trivalent iron. Magnesium oxide and FeO determine the direction of mineral formation in pellets. Since MgO leads to dissociation of trivalent iron only in the melt, and a small amount of iron dissolves in the pellet melt compared to the agglomerate, the newly formed FeO is not enough to change the mineral formation of the pellet binder with a basicity higher than 0.7. Therefore, all divalent iron and magnesium are spent constructing a magnetite solid solution.

During agglomeration, depending on the ratio of divalent to trivalent iron in the melt, which is determined by the oxidation potential of the gas phase, MgO is part of the ore phase or silicates. The more FeO in the melt, the more MgO in the lattice of the magnetite phase.

Thus, the processes of mineral formation in batches, by hardened methods, both during the roasting of granules and pellets, and during agglomeration, have shown that changing the oxidation potential of the gas phase is an effective lever. In this case, not only are the properties of ferrous sand, a waste product of alumina production, improved, but also new bonds and new types of iron ore raw materials are created in the form of granules, pellets, and agglomerates suitable for use as a charge in smelting ferrosilicon.

Author contributions

Conceptualization: AZ; Data curation: PB, AZ; Formal analysis: AZ-a, AZ, PB; Funding acquisition: AZ; Investigation: AZ; Methodology: OZ, AZ; Project administration: AZ, AZ-a; Resources: OZ, AZ; Software: OZ, AZ; Supervision: AZ; Validation: AZ-a, AZ, PB; Visualization: OZ, AZ; Writing – original draft: AZ-a, AZ; Writing – review & editing: OZ. All authors have read and agreed to the published version of the manuscript.

Funding

This research was carried out within the research framework funded by the Science Committee of the Ministry of Science and Higher Education of the Republic of Kazakhstan (grant AR 23488812).

Acknowledgements

The authors would like to thank all colleagues and institutions who contributed to the preparation of this study. Their support and collaboration are gratefully acknowledged.

Conflict of interest

The authors declare no conflict of interest.

Data availability statement

The original contributions presented in this study are included in the article. Further inquiries can be directed to the corresponding author.

References

[1] Ibragimov, A.T., & Budon, S.V. (2010). Razvitie tehnologii proizvodstva glinozema iz boksitov Kazahstana. Pavlodar. *LLP «Dom pechati».*

[2] Zhang, R., Zheng, S., Ma, S. & Zhang, Y. (2011). Recovery of alumina and alkali in Bayer red mud by the formation of andradite-grossularhydrogarnet in hydrothermal process. *Journal of Hazardous Materials*, (189), 827-835. https://doi.org/10.1016/j.jhazmat.2011.03.004

[3] Evan, K. (2016). The history, challenges and new developments in the management and use of bauxite residueю. *Journal of Sustainable Metallurgy*, *2*, 316-331. https://doi.org/10.1007/s40831-016-0060-x

[4] Trushko, V.L., Utkov, V.A. & Bazhin, V.Y. (2017). Topicality and possibilities for complete processing of red mud of aluminous production. *Journal of Mining Institute*, (227), 547. https://doi.org/10.25515/PMI.2017.5.547

[5] Podgorodetsky, G., Shiryaeva, E., Gorbunov, V. & Kozlova, O.A. (2015). Problem of Efficient Red Mud Processing, Search for Solutions. *Ecology and Industry of Russia, 19*(12), 46-53. https://doi.org/10.18412/1816-0395-2015-12-46-53

[6] Zinoveev, D.V., Grudinskii, P.I., Dyubanov, V.G., Kovalenko, L.V. & Leont'ev, L.I. (2018). Global recycling experience of red mud - a review. Part i: pyrometallurgical methods. *Izvestiya. Ferrous Metallurgy, 61*(11), 843-858. https://doi.org/10.17073/0368-0797-2018-11-843-858

[7] Zhaobo, L., & Hongxu, L. (2015). Metallurgical process for valuable elements recovery from red mud – a review. *Hydrometallurgy*, *155*, 29-43. https://doi.org/10.1016/J.HYDROMET.2015.03.018

[8] Kaussen, F., & Friedrich, B. (2015). Reductive smelting of red mud for iron recovery. *Chemie Ingenieur Technik*, *87*(11), 1535-1542. https://doi.org/10.3390/met10010032

[9] Grenerczy, G., & Wegmuller, U. (2011). Persistent scatterer interferometry analysis of the embankment failure of a red mud reservoir using ENVISAT ASAR data. *Natural Hazards*, *59*, 1047-1053. https://doi.org/10.1007/s11069-011-9816-6

[10] Klauber, C., Grafe, M. & Power, G. (2011). Bauxite residue issues: II. Options for residue utilization. *Hydrometallurgy*, *108*(1-2), 11-32. https://doi.org/10.1016/j.hydromet.2011.02.006

[11] Grafe, M., & Klauber, C. (2011). Bauxite residue issues: IV. Old obstacles and new pathways for in situ residue bioremediation. *Hydrometallurgy*, *108*(1-2), 46-59. https://doi.org/10.1016/j.hydromet.2011.02.005

[12] Liu, Y., & Naidu, R. (2014). Hidden values in bauxite residue (red mud): recovery of metals. *Waste Management*, *34*(12), 2662-2673. https://doi.org/10.1016/j.wasman.2014.09.003

[13] Khairul, M. A., Zanganeh, J. & Moghtaderi, B. (2019). The composition, recycling and utilisation of Bayer red mud. *Resources Conservation and Recycling*, *141*, 483-498. https://doi.org/10.1016/j.resconrec.2018.11.006

[14] Xiao, J., Peng, Y., Ding, W., Chen, T., Zou, K., & Wang, Z. (2020). Recovering scandium from scandium rough concentrate using roasting -hydrolysis -leaching process. *Green Separation and Extraction Processes*, *8*(3), 365-380. https://doi.org/10.3390/pr8030365

[15] El-Hussiny, N.A., Mohamed, F.M. & Shalabi, M.E.H. (2011). Recycling of mill scale in sintering process. *Science of sintering*, (43), 21-31. https://doi.org/10.2298/sos1101021e

[16] Zhunusova, A., Zhunusov, A., Bykov, P., Bakirov, A., Zayakin, O. & Kenzhebekova, A. (2024). Research of physicochemical properties of ferrous sands from alumina production. *Acta Metallurgica Slovaka*, *30*(4), 161-166. https://doi.org/10.36547/ams.30.4.2086

[17] Zhunussova, A., Bykov, P., Zhunusov, A., & Kenzhebekova, A. (2024). Research of the production of iron ore sinter from bauxite processing waste. *Kompleksnoe Ispolzovanie Mineralnogo Syra = Complex Use of Mineral Resources*, *329*(2), 73-81. https://doi.org/10.31643/2024/6445.19

[18] Malysheva, T.Ja., Dolickaja, O.A. (2004). Petrografija i mineralogija zhelezorudnogo syr'ja: Uchebnoe posobie dlja vuzov. *Moscow: MISIS.*

[19] Zhunusov, A.K., Bykov, P.O., Kenzhebekova, A.E., Zhunussova, A.K, & Nabawi, R.A. (2024). Study of the isothermal kinetics of reduction of sinter from mill scale. *Kompleksnoe Ispolzovanie Mineralnogo Syra = Complex Use of Mineral Resources*, *328*(1), 59-67. https://doi.org/10.31643/2024/6445.07

$CaO–Fe_2O_3–SiO_2$ жүйесінің күй диаграммасы тұрғысынан темір кенді материалдарының құрылысындағы минерал түзілуінің ерекшеліктері

А. Жунусова[1], П. Быков[1], А. Жунусов[1*], О. Заякин[2], А. Бакиров[1], А. Кенжебекова[1]

[1]*Торайғыров университет, Павлодар, Қазақстан*

[2]*Ресей ғылым академиясының Орал филиалының металлургия институты, Екатеринбург, Ресей*

**Корреспонденция үшін автор: zhunusov_ab@mail.ru*

Аңдатпа. Осы жұмыста газ тәрізді отынды пайдалана отырып, түйіршіктер мен шекемтастарды тотығу арқылы күйдіру және агломерациялық қабатта қатты отынды жағу арқылы агломерациялау кезінде алынған темір кені шикізатын беріктендіру зерттеулерінің нәтижелері келтірілген. Түйіршіктер, шекемтастар мен агломераттарда минерал түзілудің механизмдеріндегі айырмашылықтар сұйық фазалық беріктену сатысында байқалады және бұл темірдің беріктендіретін балқыманың түзілуіндегі әртүрлі рөлімен түсіндіріледі. Бұл жағдайда агломератта және түйіршіктер мен шекемтастарда темір әртүрлі валентті күйде болады, бұл процестердің ерекшеліктеріне әсер етеді. Түйіршік пен шекемтастардағы темір-силикатты балқымада темір үш валентті күйде болады және шикізат құрамындағы силикат түзуші компонент болып табылмайды. Барлық зерттелген негізділік ауқымында (0.3-1.5)

байланыстырғыштардың силикатты құрамы $CaO–SiO_2$ сызығы бойында орналасады, бұл $CaO–Fe_2O_3–SiO_2$ жүйесінің күй диаграммасын қолдану арқылы анықталады. Агломерация кезінде кремний бар балқыма FeO-ның артық мөлшері жағдайында түзіледі, бұл агломераттағы темір-силикатты байланыстырғыштың минерал түзуші процесін бағыттайды. Агломерацияның стандартты жағдайларында 1.0-1.5 негізділіктегі силикатты байланыстар $CaO–FeO–SiO_2$ жүйесінің күй диаграммасындағы оливиндік өрісте түзіледі және құрамдарының кең ауқымын қамтиды. Түйіршіктер мен шекемтастарды күйдіру мен агломерациялау арқылы беріктендірілген шикізаттарда минерал түзілудің жүруі газ фазасының тотығу потенциалын өзгерту – глинозем өндірісінің қалдығы болып табылатын темірлі құмның қасиеттерін жақсартуда ғана емес, сондай-ақ жаңа байланыстырғыштар мен жаңа түрдегі темір кенді шикізаты жасаудың да тиімді тетігі екенін көрсетті.

Негізгі сөздер: *темірлі құм, агломерация, жентектеу, темір кенді агломерат, флюстер.*

Особенности минералообразования в структуре железорудных материалов с позиции диаграммы состояния системы $CaO–Fe_2O_3–SiO_2$

А. Жунусова[1], П. Быков[1], А. Жунусов[1*], О. Заякин[2], А. Бакиров[1], А. Кенжебекова[1]

[1]*Торайгыров университет, Павлодар, Казахстан*

[2]*Институт металлургии Уральского отделения Российской Академии наук, Екатеринбург, Россия*

**Автор для корреспонденции: zhunusov_ab@mail.ru*

Аннотация. В настоящей работе приводятся результаты исследования упрочнения железорудного сырья, полученные при окислительном обжиге окатышей с использованием газообразного топлива и агломерации со сжиганием твёрдого топлива в агломерационном слое. Различия в механизмах минералообразования окатышей и агломерата проявляются на стадии жидкофазного упрочнения и обусловлены различной ролью железа в формировании упрочняющего расплава. При этом в агломерате и окатыше железо находится в разных валентных состояниях, что влияет на особенности процессов. В железосиликатном расплаве окатышей железо находится в трёхвалентном состоянии и не является силикатообразующим компонентом шихты. Силикатные составы связок во всём исследованном диапазоне основностей (0.3-1.5) располагаются вдоль линии соединения $CaO–SiO_2$, которое определяется при использовании диаграммы состояния системы $CaO–Fe_2O_3–SiO_2$. При агломерации кремнийсодержащий расплав формируется в условиях избытка FeO, что направляет процесс минералообразования при создании железосиликатной связки агломерата. В стандартных условиях агломерации силикатные связки с основностью 1.0-1.5 формируются в оливиновом поле диаграммы состояния $CaO–FeO–SiO_2$, охватывая широкий диапазон составов. Процессы минералообразования в шихтах, упрочненными способами, как при обжиге окатышей, так и при агломерации показали, что изменение окислительного потенциала газовой фазы является действенным рычагом на пути не только улучшения свойств железистого песка – отхода глиноземного производства, но и создания, как новых связок, так и новых видов железорудного сырья.

Ключевые слова: *железистый песок, агломерация, спекание, железорудный агломерат, флюсы.*

Publisher's note

All claims expressed in this manuscript are solely those of the authors and do not necessarily represent those of their affiliated organizations, or those of the publisher, the editors and the reviewers.

SATBAYEV UNIVERSITY

Engineering Journal of Satbayev University

Volume 147 (2025), Issue 3, 20-29

https://doi.org/10.51301/ejsu.2025.i3.04

Assessment of the ventilation system and solutions for improving the ventilation network at Khe Cham Coal Mine, Vietnam

C.H. Nguyen[1], T.T. Vu[1,2*], D.T. Le[1,2], S.A. Do[1], C.V. Dao[1,2], P.Q. Le[1,2]

[1]*Hanoi University of Mining and Geology, Hanoi, Vietnam*

[2]*Research Group: Sustainable Development of Mining Science, Technology and Environment (SDM), Hanoi University of Mining and Geology, Hanoi, Vietnam*

**Corresponding author: vutrungtien@humg.edu.vn*

Abstract. Ventilation for underground mines plays an essential role in production activities by ensuring labor safety and maintaining environmental conditions. Mine ventilation is also one of the most effective methods for preventing methane gas and coal dust explosions. Therefore, it is necessary to investigate the ventilation network annually and calculate the overall ventilation requirements for underground mines in the Quang Ninh coalfield. Based on the production plan and ventilation needs of the Khe Cham Coal Mine, the authors surveyed and evaluated the mine ventilation network, thereby proposing solutions to improve the ventilation system and calculating the ventilation parameters for 2025. To achieve the research results presented in this article, the authors used methods such as data collection, analysis and synthesis, field surveys, result analysis and evaluation, combined with numerical modeling using ventilation software to verify calculation results. To ensure ventilation for Khe Cham Coal Mine in 2025, two main fan stations – №1 at level +35 and №2 at level +112 should be operated jointly, with the following calculated working modes: fan station №1 at level +35: airflow of 193.72 m^3/s, air pressure of 448 mmH_2O, impeller angle of 40°; fan station №2 at level +112: airflow of 155.8 m^3/s, air pressure of 419.5 mmH_2O, impeller angle of 35°. Based on the analysis of data collected at the Khe Cham Coal Mine, the paper assesses the overall ventilation status of the mine. It proposes solutions to improve the ventilation network, ensuring safety during production activities. Additionally, it determines the combined working mode of the two main fan stations, providing a foundation for developing the general ventilation plan for Khe Cham Coal Mine in 2025.

Keywords: *coal mine, ventilation system, airflow, air pressure, Khe Cham Coal Mine.*

Received: 12 January 2025
Accepted: 15 June 2025
Available online: 30 June 2025

1. Introduction

The main task of general ventilation for underground coal mines is to provide sufficient and necessary clean air for people working in the mine according to regulations [1]. Mine ventilation contributes to diluting the concentration of toxic and explosive gases to the allowable safety limit, diluting the concentration of dust generated during mine operations to the permissible limit, and removing it from the mine. At the same time, it also contributes to improving the microclimate conditions at working locations in the mine [2]. As mentioned in many studies, calculating and selecting mine ventilation methods is an essential problem. It depends on many factors, including the mine gas factor and mine class, which are among the factors that need to be considered [3]. Calculating general ventilation for mines is difficult, partly due to the extensive mine tunnel system, simultaneous exploitation of many longwalls, and different exploitation levels, which leads to complex ventilation diagrams [4, 5].

Due to changes in the tunnel system in underground coal mines, the mine output also changes annually to match the actual production. Therefore, it is necessary to periodically inspect and survey the mine ventilation network every year to ensure ventilation conditions and safety in the mine. There are many studies on mine ventilation calculation and mine ventilation network inspection. Some typical studies on ventilation inspection and solutions [6, 7], mine ventilation model [8, 9], optimal calculation of ventilation network and adjustment of mine airflow [10, 11, 12, 13], solutions to stabilize mine ventilation network, reduce airflow leakage and balance airflow in underground coal mines [14, 15, 16]. In addition, some other typical studies related to adjusting air pressure balance and ventilation for mechanized mining longwall [17, 18, 19].

In the Quang Ninh coal mine area, Vietnam, ventilation calculations and mine ventilation network inspections are carried out regularly. In recent years, several typical studies related to ventilation solutions have been conducted at Ha Lam, Quang Hanh, Duong Huy, Ha Long and Cam Thanh Coal Mines [20, 21, 22, 23, 24], studies to determine the reasonable working mode of the main fan have been conducted at Thong Nhat and Nam Mau Coal Mines [25, 26], and studies on the application of ventilation calculations using software [27, 28].

nguyenhongcuong@humg.edu.vn, vutrungtien@humg.edu.vn, t.d.le@humg.edu.vn, doanhson@humg.edu.vn, daovanchi@humg.edu.vn, lequangphuc@humg.edu.vn
Engineering Journal of Satbayev University. eISSN 2959-2348. Published by Satbayev University

In 2024, Khe Cham Coal Mine operated with a production capacity of 1.8 million tons, with nine longwalls working simultaneously. The mine is developing tunnels and extracting coal from levels −300 to −100. Two main fan stations provide general mine ventilation: №1 at level +35 and №2 at level +112.

– fan station №1 at level +35: equipped with a 2K56-№30 fan, impeller angle of 35°;

– fan station №2 at level +112: equipped with a 2K56-№30 fan, impeller angle of 35°.

The current mine ventilation situation in 2024 shows that the general ventilation situation of the mine is facing many difficulties, and it is often necessary to maintain 3-4 auxiliary fan stations in the mine to meet the ventilation requirements, which leads to potential risks of unsafe production. The production plan in 2025 will continue to maintain exploitation with an output of 1.8 million tons. To ensure the production plan, it is necessary to dig nearly 16,000 meters of tunnel, prevent and cut thousands of meters of tunnel, and exploit 10 longwalls operating simultaneously.

The above domestic and foreign studies have all mentioned the method of calculating mine ventilation, solutions to improve mine ventilation efficiency, and solutions to balance mine air pressure. However, the research and survey of mine ventilation network, as well as ventilation calculation for Khe Cham Coal Mine in 2025 have not been carried out. Therefore, it is necessary to assess the current status and determine the working mode of fan stations for Khe Cham Coal Mine to ensure safety in production and the working environment. The research results of the paper are the basis for application in actual production at Khe Cham Coal Mine.

2. Materials and methods

2.1. Study area

The study was conducted at the Khe Cham Coal Mine, located in Mong Duong Ward, Cam Pha City, Quang Ninh Province, Vietnam. The mine is situated approximately 20 km north of the Cam Pha city center, along the left side of Route 18A from Ha Long to Mong Duong [29]. It is bordered by the Bac Huy fault to the north, Khe Cham II-IV Coal Mine to the south, Khe Cham I Coal Mine to the east, and Khe Tam Coal Mine to the west. The location of the Khe Cham Coal Mine is illustrated in Figure 1.

Figure 1. Location map of the Khe Cham Coal Mine (modified from [30])

2.2. Current status of the Khe Cham Coal Mine ventilation system diagram

In 2024, Khe Cham Coal Mine operated nine longwalls simultaneously, distributed across three seams: 14.5, 14.4, and 14.2 [31].

Coal seam 14.5 included five longwalls (14.5-33.1, 14.5-28A, 14.5-28B, 14.5-28.1, and 14.5-12.5), all exploited using drilling and blasting technology with chain support. The operating levels for these longwalls were as follows:

– 14.5-33.1: from −126 to −158;

– 14.5-28A: from −95 to −143;

– 14.5-28B: from −126 to −155;

– 14.5-28.1: from −136 to −170;

– 14.5-12.5: from −269 to −275.

Seam 14.4 included one longwall (14.4-23), exploited using drilling and blasting technology with chain support, operating from −140 to −162.

Coal seam 14.2 included three longwalls:

– 14.2-12, exploited using fully mechanized technology with shield support, from −182 to −208;

– 14.2-10, exploited using drilling and blasting technology with chain support, from −169 to −173;

– 14.2-1, exploited using drilling and blasting technology with chain support, from −182 to −213.

To ensure ventilation for the nine simultaneously operating longwalls and airflow consumption areas mentioned above, Khe Cham Coal Mine applies the exhaust ventilation method based on a side ventilation diagram, with the main fan stations located at +35 and +112 levels, as detailed below (Figure 2). Complex multi-level ventilation system is important for maintaining air quality, diluting hazardous gases, and ensuring the safety of miners across all active longwalls.

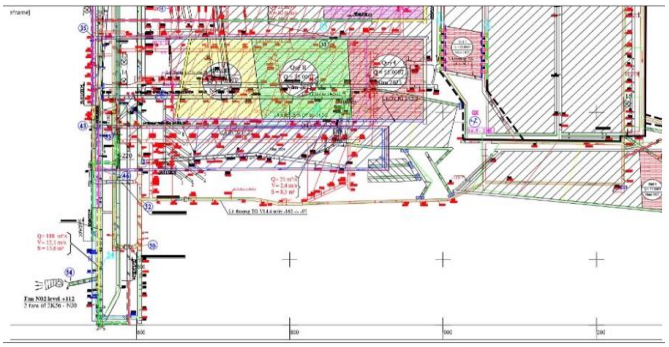

(a)

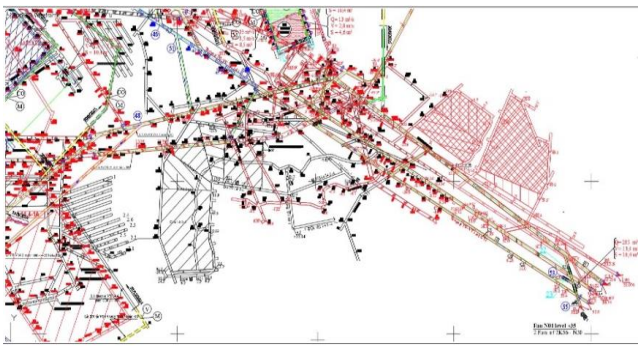

(b)

Figure 3. The ventilation system diagrams of Khe Cham Coal Mine [31]

The diagrams in Figure 2 illustrate the airflow organization, the arrangement of the main fan stations, and the ventilation pathways supplying fresh air to the working longwalls.

Fan station №1 equipped with a 2K56-№30 fan (one working fan and one standby fan), installed at the +35 level. Fresh air enters through the auxiliary inclined shaft, descends to the shaft station at the −300 level, and passes through the transport brake incline from +25 to −90. It then follows the brake inclines and haulage levels to the consumption areas of Seam 14.5 (14.5-33.1 longwall), Seam 14.4 (14.4-23 longwall), and Seam 14.2 (14.2-12 and 14.2-10 longwalls), reaches the ventilation level, and exits through the upper ventilation brake incline to the exhaust fan station at the +35 level.

Fan station №2 equipped with a 2K56-№30 fan (one working fan and one standby fan), installed at the +112 level. Fresh air enters through the auxiliary inclined shaft, descends to the shaft station at the −300 level, and passes through the transport brake incline from −168 to −145. It then follows the brake inclines and haulage levels to the consumption areas of Seam 14.5 (14.5-28A, 14.5-28B, 14.5-28.1, and 14.5-12.5 longwalls) and Seam 14.2 (14.2-1 longwall), reaches the ventilation level, and exits through the upper ventilation brake incline to the exhaust fan station at the +112 level.

2.3. Research methods

The study employed a combination of field measurements, data analysis, and numerical modeling techniques to assess the ventilation system at Khe Cham Coal Mine.

Specialized measuring equipment was utilized to collect field data, including air speed meters; Japanese Aneerroid S8 barometers; temperature and humidity meters manufactured in Japan and China; and handheld gas and air meters produced in Poland, Germany, and China. Measurements and surveys were conducted at critical locations within the mine, including the two main fan stations (№1 at +35 level and №2 at +112 level), longwall faces, preparation roadways, and large openings. A comprehensive synthesis analysis was performed based on the data collected during field surveys. The data were systematically evaluated and compared to identify ventilation characteristics, airflow distribution patterns, and potential issues within the existing ventilation network.

To supplement field observations and enhance the reliability of the analysis, two ventilation simulation software packages were employed PATH Network Diagram Software and Kazamazu Ventilation Software (Japan).

The PATH software simulated the mine ventilation network, particularly under complex conditions. Each ventilation diagram was represented as a PATH network, allowing the determination of air pressure values across all flows passing through the network nodes. The maximum air pressure within the mine ventilation system was identified based on these calculations.

Kazamazu software was applied to accurately model and analyze the working modes of the main fans. The key functionalities of the Kazamazu software included identifying the main components of the mine ventilation network; determining system limitations and critical points; editing and analysis of simulation results and analysis of standard airflow distribution across the ventilation network.

These combined research methods provided a comprehensive basis for evaluating the current ventilation status and for developing proposals to optimize the ventilation system at Khe Cham Coal Mine.

3. Results and discussion

3.1. Assessment of the current status of the ventilation system of Khe Cham Coal Mine (2024)

3.1.1. Assessment of ventilation of the longwalls

Regarding the airflow direction in the longwalls, the ventilation pattern is generally from bottom to top, which complies with safety regulations for mines with explosive gas conditions. In some longwalls where the airflow moves from top to bottom, additional fresh air is supplied to dilute methane concentrations. However, it is recommended that the dust control regime in these areas be closely monitored to ensure safe working conditions.

Regarding the airflow and airspeed through the longwalls, the results of the calculations and field measurements of the required airflow are presented in Table 1.

Table 1. Assessment of airflow and speed through the longwalls

№	Name of longwall	Airflow (m^3/s)			Speed of air, m/s			
		Field	Maximum	Assessment	Cross-section, m^2	Field	Allowing	Assessment
1	14.5-28.B	6.9	12	insufficient	4.6	1.5	0.25-4	Enough
2	14.4-12	7.82	21			1.7		
3	14.5-28.A	9.98	14			1.4		
4	14.4-15	10.12	12			2.2		
5	14.2-10.2	6.99	12			1.52		
6	14.4-16	8.28	12			1.8		
7	14.4-23	6.44	10			1.4		
8	14.2-1	7.82	11			1.7		

Analysis of the data in Table 1 shows that the airflow passing through the longwalls in all eight surveyed longwalls does not meet the required standards. Considering losses through the worked-out areas and the pre-digging brake inclines, the airflow should reach at least 70% of the calculated airflow values. In particular, the 14.4-12 longwall demonstrates a significant shortfall, lacking approximately 50% of the maximum required airflow. Regarding the composition of toxic and harmful gases in the longwalls, automatic centralized monitoring data and actual field measurements indicate that the concentrations of toxic gases (CH_4, CO_2) are within allowable limits. However, in the 14.5-28.A longwall, CO_2 emissions into the working area have been detected. In this case, it is necessary to provide additional airflow into the longwall and install a temporary ventilation door if there is insufficient space to construct a permanent crosswall.

This measure would help prevent air leakage from the exploited area, thereby reducing the ingress of CO_2 into the longwall. Regarding microclimate conditions in the longwalls, the measurement and survey results show that the air temperature generally remained within allowable limits but was close to the upper threshold. Therefore, measures such as mist spraying and increasing fresh air intake into the mine are recommended to lower the temperature and enhance airflow through the longwalls. Additionally, in 2025, longwalls with opposite airflow directions, such as 14.4-16 and 14.2-9, will require adjustments, including reducing the slope of the longwalls and adding fresh air to the polluted airflow before it mixes with the common return air.

Regarding booster fans for longwall ventilation, while this solution provides timely support for production without needing pre-digging brake inclines and rim roadways to supply and remove air, it also presents several disadvantages. Using booster fans significantly increases electricity consumption, as each longwall requires two FBD2×30 kW fans operating continuously. Moreover, reversing the airflow in the event of an incident becomes more difficult. Importantly, electric motor-driven booster fans cannot effectively prevent the ignition of methane gas in mines with explosive gas hazards. Consequently, while the current solutions are effective in the short term, they are considered temporary. They must be replaced by the proper excavation of ventilation routes and the calculation of fresh air supply for the respective longwalls.

3.1.2. Assessment of the longwalls ventilation

The measurement and survey data on the ventilation status of the preparation roadways are presented in Table 2.

Table 2. Assessment of airflow and speed through the preparation roadways

№	Name of roadways	Measurement results			Q calculation result (m³/s)	Assessment
		V, m/s	S, m²	Q, m³/s		
1	Haulage level of 14.5-29A	0.3	9.3	2.79	2.8	Enough
2	Haulage level of 14.5-24.1		9.3	2.79	2.2	Enough
4	Ventilation level of 14.2-2		7.8	2.34	2.6	Insufficient
5	Ventilation level of 14.5-35A		9.3	2.79	2.8	Enough
6	Haulage level of 14.5-10.2		9.3	2.79	2.8	Enough
7	Haulage level of 14.5-35A		9.3	2.79	2.8	Enough
8	Ventilation level of 14.2		7.8	2.34	2.6	Insufficient
9	Haulage level of 14.5-36.1		9.3	2.79	2.8	Enough
10	Ventilation level of 14.5-36.1		9.3	2.79	2.8	Enough
11	Haulage level of 14.5-33.2		9.3	2.79	2.8	Enough
12	Haulage brake incline of 14.5-37		9.3	2.79	2.8	Enough
13	Haulage level of 14.5-21.1		7.2	2.16	2.2	Enough
14	Haulage level of 14.5-24.1		7.2	2.16	2.2	Enough

Analysis of the data in Table 2 shows that most of the preparation roadways meet the ventilation requirements. However, two ventilation roadways, specifically the Ventilation level of 14.2-2 and the Ventilation level of 14.2, exhibit insufficient airflow compared to the calculated airflow requirements. These areas require additional ventilation measures to ensure compliance with safety standards and maintain suitable working conditions.

Most roadways have average ventilation lengths ranging from 100 to 500 meters, thus ventilation operations do not face significant difficulties. The fans' locations comply with the regulations, adequate ventilation capacity is sufficient, and the airflow sufficiently meets the requirements for mine excavation activities.

The installed booster fans are in good working condition. Ventilation ducts are correctly installed and maintained under the ventilation methods applied at the mine. The airflow supplied to the working faces generally meets the required levels, and the microclimate conditions at the faces are within acceptable limits as regulated. However, in some working faces, insufficient airflow has been observed. Therefore, it is necessary to inspect the pipe connection points and the overall condition of the ventilation pipes to identify and rectify any deficiencies promptly.

3.1.3. Assessment of the longwalls ventilation

The ventilation works of the mine, as identified during the survey, include the fan station houses, fan drifts, ventilation doors, ventilation doors with adjustable regulators, ventilation gates, and partitions.

The fan stations №1 and №2 are solidly and firmly constructed, providing stable support for the mine ventilation system. The quality of the fan drifts ensures effective airflow, contributing to the overall efficiency of the ventilation network. The ventilation doors throughout the mine are arranged reasonably, with a solid structure that effectively regulates airflow within the mine.

The ventilation gates, installed to prevent air leakage at the two main fan stations, are of good quality and maintain air leakage within the allowable limit of Q_r = 5 m³/s, as regulated. Additionally, these ventilation works contribute significantly to preventing air leakage into the exploited areas, thus maintaining safe and efficient ventilation conditions throughout the mine.

3.1.4. Assessment of the working capacity of fan stations

The results of calculations, measurements, and surveys of the working modes of the main fans at the two fan stations are presented in Table 3.

Table 3. Working modes of the main fans

Stations	№1	№2
Name of fans	2K56-№30	2K56-№30
Impeller angle, degree	35	30
Working mode by calculation: – Airflow, m³/s; – Air pressure, mmH_2O	 165 305	 140 230
Working mode according to measurement and survey: – Airflow, m³/s; – Air pressure, mmH_2O	 182.04 182.04	 270 160

Analysis of the data presented in Table 3 shows that the two main fan stations are operated in association to create air pressures of 270 mmH_2O and 160 mmH_2O for stations №1 and №2, respectively. These air pressures are within the normal operating range of the installed fans.

The measurement results indicate that when both fans are operated jointly, the total airflow reaches 265 m³/s. However, the maximum air pressure at fan station №1, measured at 270 mmH_2O, is significantly lower than the calculated value and the rated capacity of the fan. Therefore, the actual working mode of the two fans does not fully meet the optimal performance parameters. Nevertheless, the system can be adjusted to increase the airflow into the mine, thereby improving ventilation efficiency.

3.2. Proposed solutions to improve the ventilation network to ensure safety

3.2.1. General viewpoint

In order to develop an effective solution for completing the general ventilation system of the entire mine, it is necessary to unify the overall approach and implement the following specific technical ventilation measures:

– ensure that sufficient airflow is provided to all consumption areas of the mine;

– avoid placing local fans in dirty air tunnels to ventilate the longwalls, as this could compromise air quality and ventilation efficiency;

– in longwalls with opposite airflow directions, fresh air must be introduced into the polluted airflow to improve air quality during its passage through the common return airways.

3.2.2. Proposed solutions

To address the ventilation issues identified above, the following solutions are recommended:

– excavate a brake incline in front of the 14.5-36 longwall area to provide a fresh air supply;

– excavate a rim roadway to direct polluted air from the ventilation level of 14.4-17 to the haulage brake incline between levels −145 and −268 of Seam 14.2;

– excavate a rim roadway from the ventilation level of 14.2-2 to the middle gate of Seam 14.2 to improve ventilation;

– excavate a rim roadway from the haulage brake incline between levels −83 and −150 to the haulage level of 14.2-9 of Seam 14.2 to supply fresh air to the 14.2-9 longwall;

– excavate a rim roadway from the ventilation level 14.5-29A to the haulage brake incline between levels −100 and −160 of Seam 14.4.

– perform calculations and adjustments of the ventilation network to establish a reasonable and optimized ventilation mode for the mine.

3.3. General ventilation calculation for Khe Cham Coal Mine in 2025

3.3.1. Determining of consumption places

Consumption places in Khe Cham Coal Mine include the airflow supplied to longwalls, dead-end, and large opening (power stations) calculated according to the mining and tunneling plan (Tables 4-6).

Table 4 summarizes the longwalls planned for simultaneous operation in 2025 at Khe Cham Coal Mine, including their daily production outputs. These data are essential for determining the required ventilation airflow to ensure safe mining operations.

Table 4. Longwall mining plan

№	Longwall	Output, tons/day-night
1	14.5-37.1	600
2	14.05.1932	646
3	14.04.2017	547
4	CGH 14.2-9	880
5	14.5-33.A	584
6	CGH 14.2-2	1000
7	14.5-12.5A	600
8	14.5-29.A	749
9	14.5-36.1	500
10	14.2-11.1	560

Table 5. Prepared a tunnel excavation plan

№	Tunnel/Heading	Area, m²
1	Ventilation level of 14.5-28B	13.1
2	Haulage level of 14.5-28B	12.5
3	Ventilation level of 14.5-36.2	13.1
4	Opening heading of 14.5-36.2	12.5
5	Haulage level of 14.5-39	13.1
6	Opening heading of 14.5-39	12.5
7	Opening heading of 14.4-21	12.5
8	Ventilation level of 14.2-3	16.1
9	Opening heading of 14.2-3	16.1
10	Ventilation level of 14.2-12.1	13.1
11	Opening heading of 14.2-12.1	12.5
12	Ventilation level of 14.2-14	11.2
13	Haulage level of 14.2-14	11.2
14	Drainage roadway at −290 level	22
15	Ventilation-haulage crosscut at −280 (North side)	13.1
16	Ventilation incline from −180 to −280 levels	16.1

Table 6. Large openings requiring ventilation

№	Facility	Capacity, kW
1	Fan station at +35 level	2750
2	Pumping station at −90 level	1350
3	Pumping station at −220 level	700
4	Pumping station at −160 level	700
5	Fan station at +112 level	4650
6	Pumping station at −300 level	3750
7	Pumping station at −200 level	900

Table 5 presents the prepared tunnel headings, excavations, and their cross-sectional areas. Table 6 outlines the major large openings, such as fan and pumping stations, requiring ventilation in the mine. These facilities are critical for calculating the airflow needed to maintain appropriate microclimate and operational conditions.

3.3.2. Calculating the general airflow and air pressure for the entire mine

The general airflow requirement for Khe Cham Coal Mine is calculated using the following formula [32]:

$$Q_m = 1.1 \cdot \left(1.1 \cdot \sum Q_{lc} + \sum Q_{cb} + \sum Q_{ht} + \sum Q_r\right), \text{ m}^3/\text{s}, \quad (1)$$

where: 1.1 is the coefficient referring to the possibility of uneven air distribution; $\sum Q_{lc}$ is total required airflow for ventilating the longwalls (m³/s); $\sum Q_{cb}$ is total required airflow for ventilating the dead-end tunnels (m³/s); $\sum Q_r$ is total required airflow for ventilating the large openings (m³/s); $\sum Q_{ht}$ is total airflow leakage through ventilation structures (m³/s). The results of calculating the total required airflow for consumption places are shown in Table 7.

Table 7. Table of calculation results of the required airflow of consumption places

№	Name of consumption places	Required airflow, m^3/s	№	Name of consumption places	Required airflow, m^3/s
I	Longwall, Q_{lc}		II	Dead end, Q_{cb}	
1	Longwall of 14.5-37.1	13	1	Ventilation level of 14.5-28B	3.3
2	Longwall of 14.5-32	13	2	Ventilation level of 14.5-28B	3.2
3	Longwall of 14.4-17	11	3	Ventilation level of 14.5-36.2	3.3
4	Longwall of CGH 14.2-9	18	4	Opening heading of 14.5-36.2	3.2
5	Longwall of 14.5-33.A	12	5	Haulage level of 14.5-39	3.3
6	Longwall of CGH 14.2-2	21	6	Opening heading of 14.5-39	4.9
7	Longwall of 14.5-12.5A	13	7	Opening heading of 14.4-21	3.3
8	Longwall of 14.5-29.A	16	8	Ventilation level of 14.2-3	4.1
9	Longwall of 14.5-36.1	10	9	Opening heading of 14.2-3	4.8
10	Longwall of 14.2-11.1	12	10	Ventilation level of 14.2-12.1	3.4
	$\sum Q_{lc}$	139	11	Haulage level of 14.2-12.1	3.9
III	Large opening, Q_{ht}		12	Ventilation level of 14.2-14	2.8
1	Pumping station of -90 level	9	13	Haulage level of 14.2-14	3.4
2	Pumping station of -220 level	5	14	Drainage roadway of –290 level	5.7
3	Pumping station of -160 level	5	15	Ventilation- haulage crosscut of –280 level at North side	3.4
4	Pumping station of –300 level	25	16	Ventilation incline of –180 / –280 level	4.1
5	Pumping station of –200 level	6		$\sum Q_{cb}$	61.5
	$\sum Q_{ht}$	50	IV	Airflow leakage ($\sum Q_r = 10\% \sum Q_{lc}$)	13.9

From the results presented in Table 7, substituting the values into Equation (2), the general airflow requirement for the mine is calculated as follows:

$$Q_m = 1.1 \cdot \left(1.1 \cdot 139 + 61.5 + 50 + 13.9\right) \approx 306 \ \text{m}^3/\text{s}, \quad (2)$$

Based on the calculation results of airflow for the mine $Q_m = 306$ m^3/s, proceed to distribute airflow to consumption places. Based on the principle of standard airflow distribution, the airflow distribution results are shown on the ventilation diagram in Figure 3.

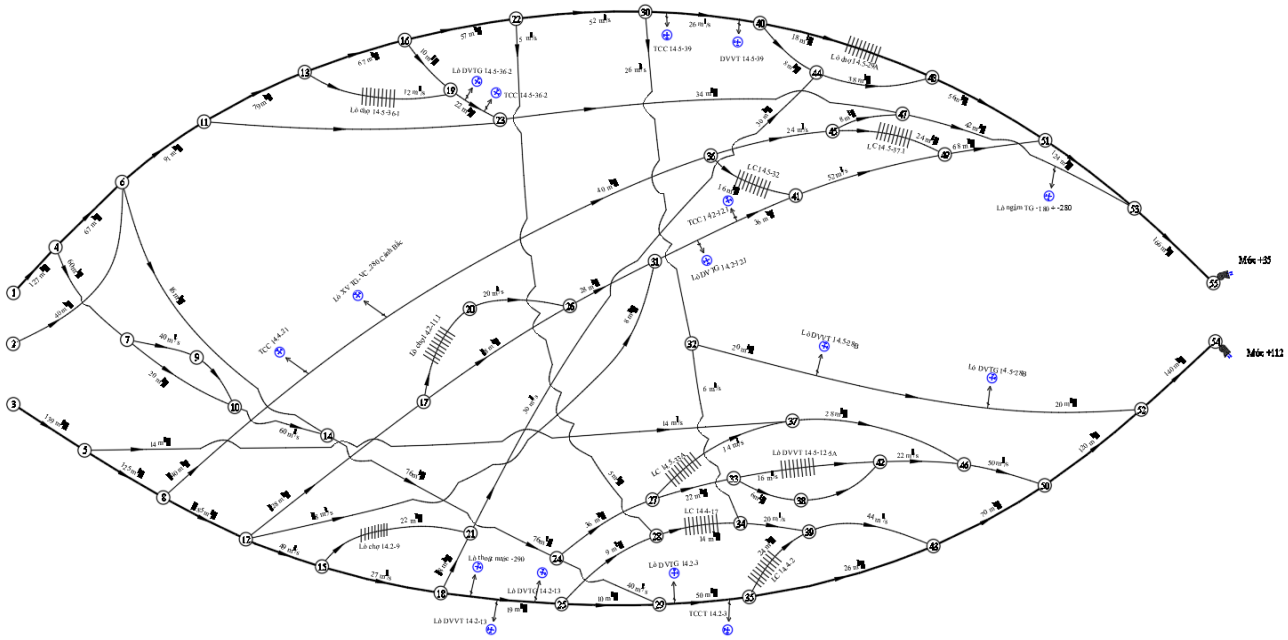

Figure 3. Ventilation diagram of Khe Cham Coal Mine in 2025

The general air pressure of the mine is calculated using the following formula [32]:

$$H = R \cdot Q^2, \ \text{mmH}_2\text{O}. \quad (3)$$

where: R is aerodynamic resistance of the tunnel, $k\mu$; Q is airflow through the tunnel, m^3/s.

When designing the mine ventilation system, the general aerodynamic resistance is determined based on the flow with the maximum air pressure, while other flows are adjusted accordingly. To calculate the general air pressure of the mine, it is necessary to determine the air pressure for all flows within the ventilation network. However, identifying the flow with the maximum air pressure can be very challenging when the complex network contains multiple nodes.

The PATH network diagram software was applied in this study to address this. Based on the ventilation diagram constructed in PATH, a matrix was generated to calculate and identify the flow corresponding to the maximum air pressure using the PATH Table. According to the calculation results, the flow passing through the nodes 3-5-8-12-15-18-25-29-35-39-43-50-52-54 (as shown in the ventilation diagram in Figure 3) exhibited the highest air pressure, with a value of $H_{max} = 363.05$ mmH_2O. Therefore, the general air pressure of the mine is determined as: $H_m = H_{max} = 363.05$ mmH_2O. These results form the basis for selecting, adjusting, and operating the main fans to ensure stable and efficient ventilation throughout Khe Cham Coal Mine in 2025.

3.3.3. Determining the appropriate working mode of the main fans

The appropriate working mode of the main fans must meet several requirements: it should ensure the required airflow and air pressure, operate within the practical and stable region of the fan characteristic curves, and maintain overall stability in the mine's production process.

Based on the 2025 ventilation plan results, the total required airflow for Khe Cham Coal Mine was determined to be 306 m³/s. According to the ventilation diagram in Figure 3, the airflow requirements were distributed between the two main fan stations, with fan station №1 requiring $Q_1 = 166$ m³/s and fan station №2 requiring $Q_2 = 140$ m³/s. Similarly, the air pressure requirements were determined based on the PATH network diagram analysis results. The calculated pressures necessary to maintain proper airflow through the ventilation network were $H_1 = 352.07$ mmH_2O for fan station №1 and $H_2 = 363.05$ mmH_2O for fan station №2 [33].

The appropriate working modes of the main fans were determined based on these airflow and air pressure values. The fans must operate with parameters that satisfy the ventilation demands and ensure efficient energy use and reliable functioning throughout the mine's operations. The calculated operating parameters for the main fans are summarized in Table 8.

Table 8. Working mode of the main fan stations of Khe Cham Coal Mine in 2025

Stations	Name of fans	Airflow (Q), m³/s	Air pressure (H), mmH_2O	Engine power, KW	Impeller angle, degree
№1 level +35	2K56-№30	182	415	1250	40
№2 level +112	2K56-№30	154	408.1	1250	35

Thus, the selected operating parameters for the main fans ensure that the ventilation system will meet both the production needs and the safety requirements of Khe Cham Coal Mine in 2025.

3.3.4. Use ventilation software to verify calculation results

To re-check the operating capacity of the fan stations to meet the calculated airflow and air pressure requirements, Kazamaru ventilation calculation software must be used to check and determine the reasonable working mode of the fan stations. Based on the calculation results of the airflow, air pressure of the ventilation network, and the impeller angle of the fans, use Kazamazu ventilation software (Japan) to determine the main fans' working mode accurately. Enter the resistance parameters of the roadway adjusted according to the PATH network, the characteristics of the 2K56-№30 fan into the Kazamazu software for calculation. The airflow results are shown in Figure 4, and the fan working points in Figure 5.

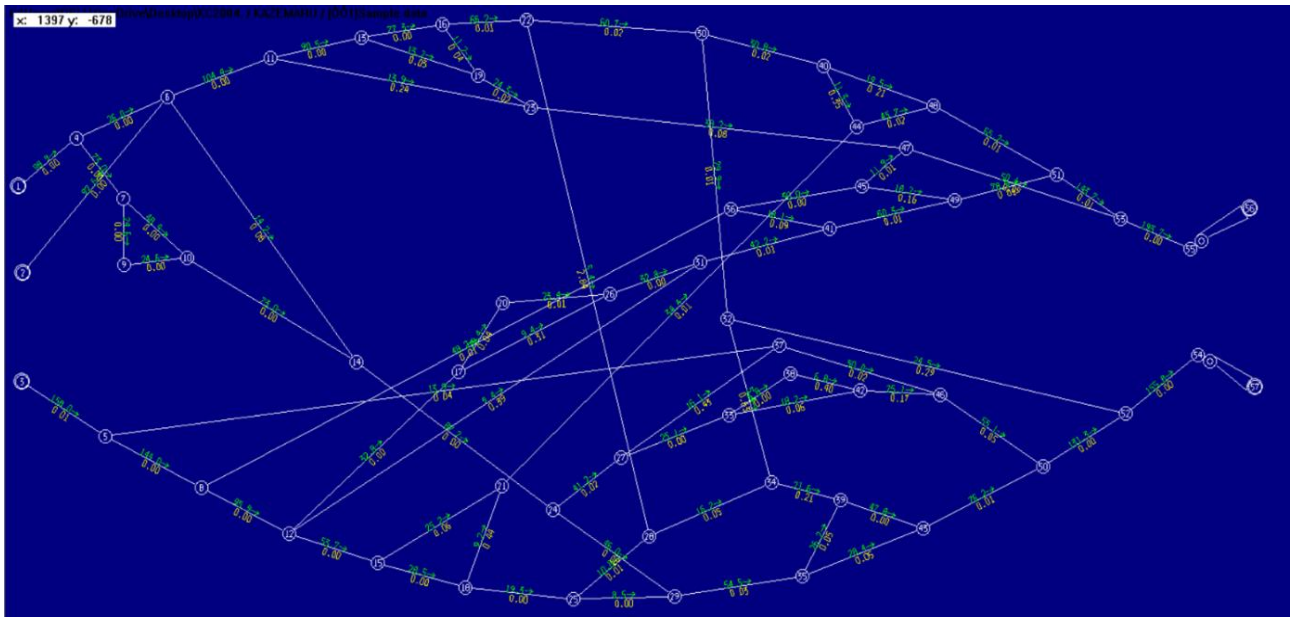

Figure 4. Diagram to determine the actual airflow of combined working fans using Kazamazu software

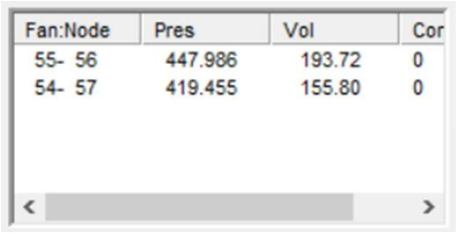

Figure 5. Working parameters of fans №1 and №2 in 2025 using software

Thus, the software results demonstrate that the reasonable working points of the fans are consistent with the design calculations, as shown in Table 9.

Table 9. Table of calculation of airflow and air pressure after putting the fans into use (using calculation software)

Stations	Name of fans	Airflow (Q), m³/s	Air pressure (H), mmH_2O
№1 level +35	2K56 - №30	193.72	447.986
№2 level +112	2K56 - №30	155.8	419.455

Through checking the airflow and air pressure of the flows, it was verified that the performance of the fans meets the requirements compared to the initial calculation results. This confirms that the selected working modes for the main fan stations are adequate to ensure stable and safe ventilation at Khe Cham Coal Mine in 2025.

5. Conclusions

Khe Cham Coal Mine, one of the largest underground mines in Vietnam, is characterized by complex geological conditions and is classified as a type II mine according to methane gas risk classification. The survey results, field measurements, and ventilation calculations conducted in 2024 indicate that the general ventilation status and microclimate conditions in the mine largely meet the required standards. However, the temperature at the longwalls remains high, reaching approximately 29°C, and insufficient airflow was recorded at several longwalls, particularly at the fully mechanized longwall faces, necessitating additional airflow to ensure operational safety.

The PATH network diagram software proved suitable for calculating airflow pressure values across the ventilation network. Additionally, the application of Kazamazu ventilation software significantly enhanced the reliability of determining the combined working mode of the main fan stations. The analysis of the ventilation network in 2025 using these software tools yielded the following results: for fan station №1 at level +35, an airflow of 193.72 m^3/s, an air pressure of 448 mmH_2O, and an impeller angle of 40° were determined; for fan station №2 at level +112, an airflow of 155.8 m^3/s, an air pressure of 419.5 mmH_2O, and an impeller angle of 35° were identified.

To ensure proper ventilation and maintain fire safety concerning methane gas, it is essential to organize excavation works, including pre-digging brake inclines and rim roadways, to introduce fresh air into the longwalls and properly discharge polluted air. These measures are necessary to maintain safe ventilation patterns in the longwall areas.

Survey results also indicate that the resistance in some branches of the ventilation network has increased by 20% to 50% compared to the calculated values. This increase is attributed to the narrowing of ventilation and transportation tunnels over time. Therefore, regular inspection of the tunnels' cross-sectional areas is required to implement timely measures for improving ventilation efficiency.

Finally, during the mining process, it is necessary to continuously monitor and inspect the ventilation system, temperature, mine gas concentrations, and overall mine resistance, with particular attention to airflow distribution in the branches serving the longwalls.

Author contributions

Conceptualization: CHN, TTV; Data curation: DTL, CVD; Formal analysis: SAD, PQL; Investigation: CHN, TTV; Methodology: TTV; Project administration: CHN, TTV; Resources: DTL, SAD; Supervision: TTV; Validation: CVD, PQL; Visualization: SAD; Writing – original draft: CHN, TTV, SAD; Writing – review & editing: TTV, DTL, CVD, PQL. All authors have read and agreed to the published version of the manuscript.

Funding

This research received no external funding.

Acknowledgements

The authors express their gratitude to Dr. Thao Van Le, project manager "Investigation and proposal of solutions to improve the ventilation network of Khe Cham Coal Mine - Khe Cham Coal Company - TKV" at the Center for Mining Science Technology and Environment, Hanoi University of Mining and Geology has created favorable conditions for the authors to complete this research. At the same time, the authors also thank the staff of the Department of Engineering and Technology of the Khe Cham Coal Mine for creating favorable conditions for data collection and field survey.

Conflicts of interest

The authors declare no conflict of interest.

Data availability statement

The original contributions presented in this study are included in the article. Further inquiries can be directed to the corresponding author.

References

[1] Minister of Industry and Trade, Vietnam (2011). National Technical Regulation QCVN 01:2011/BCT on safety in underground coal mining. Retrieved from https://lawnet.vn/tcvn/QCVN-01-2011-BCT-an-toan-trong-khai-thac-than-ham-lo-DC1A9.html

[2] Tran, X.H., Le, V.T., & Dao, V.C. (2019). Mine Ventilation for Tunnels, Traffic Tunnels and Fans. Construction Publishing House, Hanoi.

[3] Dao, V.C., Tran, X.H., & Vu, T.T.D. (2024). Determining the required airflow during non-working days and the optimal operating mode of the main fan for underground coal mine. N*ational conference on earth sciences and natural resources for sustainable development (ERSD 2024).* 820-828.

[4] Dao, V.C., & Le, T.D. (2021). Study on general characteristics of main ventilation fan stations and their connection to fan drift at vinacomin underground coal mines. *Mining Industry Journal,* (4), 64-70.

[5] Dao, V.C., Le, T.D., & Tran, X.H. (2022). Determination of actual characteristic curve of main ventilation fan at Quang Ninh underground coal mines using field measurement method. *Vietnam Journal of Earth Sciences*, *44*(2), 165-180. https://doi.org/10.15625/2615-9783/16761

[6] Zhong, D., Wang, L., Wang, J., & Jia, M. (2020). An Efficient Mine Ventilation Solution Method Based on Minimum Independent Closed Loops. *Energies*, 13(22), 5862-5862. https://doi.org/10.3390/en13225862

[7] Wang, Z., Ren, T., Ma, L., & Zhang, J. (2018). Investigations of ventilation airflow characteristics on a longwall face – a computational approach. *Energies*, *11*(6), 1564. https://doi:10.3390/en11061564

[8] Liang, Y., Zhang, J., Ren, T., Wang, Z., & Song, S. (2018). Application of ventilation simulation to spontaneous combustion control in underground coal mine: A case study from Bulianta colliery. *International Journal of Mining Science and Technology*, *28*(2), 231-242. https://doi.org/10.1016/j.ijmst.2017.12.005.

[9] Brovko, D., Makareiko, R., Sakhno, S., Yanova, L., & Pischikova, O. (2024). Modeling the stability of air flows in inclined workings in case of fire. *Mining of Mineral Deposits*, 18(3), 52-62, https://doi.org/10.33271/mining18.03.052

[10] Sui, J., Yang, L., Zhu, Z.L., Fang, H., & Hua, Z. (2011). Mine Ventilation Optimization Analysis and Airflow Control Based on Harmony Annealing Search. Comput. *6*, 1270-1277.

[11] Zeqiri, I., Gashi, J., Brahimaj, F., & Zeqiri, R. (2022). Effectiveness of ventilation regulation in a simple diagonal system of underground mines. *Mining of Mineral Deposits*, *16*(2), 81-86. https://doi.org/10.33271/mining16.02.081

[12] Mykhailenko, O., Karabut, N., Doskoch, V., Burtseva, O., Kuznetsov, V., Tsvirkun, S., & Kolomits, H. (2025). Modeling of Wind Speed Distribution in Urban Environment for the Applica-

tion of Wind Energy Potential Estimation: Case Study. *TEM Journal*, *14*(1).107-116, https://doi.org/10.18421/TEM141-10

[13] Falshtynskyi, V.S., Dychkovskyi, R.O., Lozynskyi, V.H., Saik, P.B., & Lozynska, M. I. (2025). Substantiating applicability of Western Donbas coal seams (Ukraine) for underground coal gasification. *Engineering Journal of Satbayev University, 147(*1), 31-42.https://doi.org/10.51301/vest.su.2025.i1.05

[14] Jia, T.G., Wang, S.G., Qu, G.N., & Jia, B.S. (2012) Research on the Influence of Airway Sensitivity on the Airflow Stability of Mine Ventilation System. *Journal of Mining & Safety Engineering*, *29*(1), 140-143.

[15] Dang, P.T., Malanchuk, Z., & Zaiets, V. (2021). Investigation of resistance and air leakage of auxiliary ventilation ducting in underground mine in Quang ninh. *E3S Web of Conferences*, *280*, 08002. https://doi.org/10.1051/e3sconf/202128008002

[16] Spodyniuk N., Gulai B., Zhelykh V., & Shapoval, S. (2019). Leveling of pressure flow of radial ventilator in mine ventilation system. *Naukovyi Visnyk Natsionalnoho Hirnychoho Universytetu*, (6), 80-86. https://doi.org/10.29202/nvngu/20196/12

[17] Hassen, Anwar Endris. (2021). Flow Characterization in Mine Ventilation Fan Blade Design Using CFD. *Journal of Sustainable Mining*, *20*(3), 144-156. https://doi.org/10.46873/2300-3960.1063

[18] Słota, Krzysztof and Słota, Zbigniew. (2023). Ventilation of tunnels during drilling using a forcing ventilation system – a case study. *Journal of Sustainable Mining*, *22*(4), 309-315. https://doi.org/10.46873/2300-3960.1396

[19] Zhou, F.B., Liu, Y.S., Liu, Y.K., & Zhang, Z.G. (2012). The Relationship Between 'U+I' Ventilation System of Fully Mechanized Top Coal Caving Face and Coal Spontaneous Combustion. *Journal of Mining & Safety Engineering*, *29*(1), 131-134. http://ckxb.cumt.edu.cn/EN/Y2012/V29/I1/131

[20] Dao, V.C., Tran, X.H., & et al. (2019). proposes a reasonable ventilation solution to ensure the production plan of Ha Lam Coal Mine in the period of 2019-2023. *Mining Industry Journal,* (2), 72-75.

[21] Dao, V.C., & Tran, X.H. (2020). Study on status and solution to improve the ventilation system of Quang Hanh coal mine. *Journal of Mining and Earth Sciences*, *61*(4), 110-117. http://doi.org/10.46326/JMES.2020.61(4).12

[22] Dao, V.C., Le, T.D., Vu, T.T.D., & Nguyen, H. C. (2021). Research, Calculation and Proposal of Ventilation Solution for Duong Huy Coal Mine when Mining Down to -250 m Depth. *Journal of the Polish Mineral Engineering Society*, *1*(2), 513-520. https://doi.org/10.29227/IM-2021-02-49

[23] Nguyen, H.C., Nguyen, C.K., & et al. (2021) Ventilation solution to undergroud mining site in Cao Thang mine area, Hon Gai Coal Company. *Journal of Mining and Earth Sciences*, 62(5a), 45-53. http://doi.org/10.46326/JMES.2021.62(5a).06

[24] Nguyen, C. K., Nguyen, V. T., Nguyen, P. H., & Nguyen, V. Q. (2021). A Solution to Ensure Ventilation when Expanding the Area of Cam Thanh Underground Coal Mine, Ha Long Coal Company, Vietnam. *Journal of the Polish Mineral Engineering Society*, *1*(2), 533-542. https://doi.org/10.29227/IM-2021-02-51

[25] Dao, V.C., Tran, X.H., & Le, T.D. (2021). Determination of reasonable working mode for main fan stations during pilot operation of fan station VO -22/14AR in Lo Tri area, Thong Nhat Coal Mine. *Journal of Mining and Earth Sciences*, *62*(4), 15-20. http://doi.org/10.46326/JMES.2021.62(4).02

[26] Dao, V.C., Nguyen, H.C., & Le, Q.P. (2024). Evaluation of actual working capacity of main fans and proposed solutions to improve the wind network in Nam Mau coal mine. N*ational conference on earth sciences and natural resources for sustainable development (ERSD 2024)*, 829-834.

[27] Tran, X.H., Dang, V.C., & Dao, V.C. (2014). Improve reliability calculation of wind and network solutions assurance coal mine ventilation filling opening. *Journal of Mining and Earth Sciences*, (46), 62-66.

[28] Duy Huy, N., Cao Khai, N., Van Thinh, N., Van Quang, N., Minh Chien, N., & Khac Duy, N. (2022). Simulating and Predicting Escape Routes for Ventilation Network of Duong Huy Coal Company using Ventsim DESIGN Software. *Inżynieria Mineralna*, *2*(50), 151-157. http://doi.org/10.29227/IM-2022-02-20

[29] Khe Cham Coal Company – TKV. (2020). Explanation of features of geological conditions of Khe Cham Coal Mine. *Quang Ninh, Vietnam: Department of Geodesy and Geology*

[30] Quang Ninh Portal, Quang Ninh Maps. (2025). *Retrieved from:* https://www.quangninh.gov.vn/sites/en-us/Trang/Default.aspx.

[31] Khe Cham Coal Company – TKV. (2024). Explanation of design drawings of Khe Cham Coal Mine ventilation diagram in 2024 and mine ventilation plan in 2025. *Quang Ninh, Vietnam: Department of Mining Technology*

[32] Tran, X.H., Dang, V.C., Nguyen, C.K., & Nguyen, V.T. (2014). Mine Ventilation Course. *Science and Technology Publishing House, Hanoi*

[33] Le, V.T. (2024). Project report: Investigation and proposal of solutions to improve the ventilation network of Khe Cham Coal Mine – Khe Cham Coal Company - TKV. *Center for Mining Science Technology and Environment, Hanoi University of Mining and Geology*

Вьетнам, Хэ-Чам көмір шахтасының желдету жүйесін бағалау және желдету желісін жақсарту бойынша ұсыныстар

К.Х. Нгуен[1], Т.Ч. Ву[1,2*], Д.Т. Ле[1,2], Ш.А. До[1], Ч.В. Дао[1,2], Ф.К. Ле[1,2]

[1]*Ханой тау-кен және геология университеті, Ханой, Вьетнам*

[2]*Ғылыми-зерттеу тобы: Тау-кен ғылымының, технологияның және қоршаған ортаның тұрақты дамуы (SDM), Ханой тау-кен және геология университеті, Ханой, Вьетнам*

**Корреспонденция үшін автор: vutrungtien@humg.edu.vn*

Аңдатпа. Жерасты игеру кезінде желдету өндірістік қызметте маңызды рөл атқарады, бұл еңбекке қауіп төндірмейді және қоршаған ортаның тиісті жағдайларын сақтайды. Сонымен қатар, желдету метан мен көмір шаңының жарылуын болдырмаудың ең тиімді әдістерінің бірі болып табылады. Осыған байланысты жыл сайын желдету желісін зерттеп, Куангнинь көмір бассейнінің жерасты шахталары үшін жалпы желдету қажеттіліктерін есептеу қажет. Хе-Чам көмір шахтасының өндірістік жоспары мен желдету қажеттілігін ескере отырып, авторлар шахтаның желдету желісін зерттеп, бағалады, желдетудің си-жүйесін жақсарту бойынша шешімдер ұсынды, сондай-ақ 2025 жылға арналған желдету параметрлерін есептеді. Осы мақалада келтірілген нәтижелерге қол жеткізу үшін деректерді жинау, талдау және синтездеу әдістері, далалық зерттеулер, нәтижелерді талдау және бағалау, сондай-ақ есептеулерді тексеру үшін мамандандырылған желдету бағдарламалық жасақтамасын қолдана отырып сандық

модельдеу қолданылды. Хе-Чам көмір шахтасының желдетілуін қамтамасыз ету үшін 2025 жылы екі негізгі желдеткіш станцияның бірлескен жұмысы ұсынылады - көкжиектегі №1 +35 және гори-қолшатырдағы №2 +112. Олардың жұмысының есептік режимдері келесідей: көкжиектегі №1 желдеткіш станциясы +35-ауа шығыны 193.72 м^3/с, қысым 448 мм су. қалақтардың бұрылу бұрышы 40°; горизонттағы № 2 желдеткіш станциясы +112-ауа шығыны 155.8 м^3/с, қысым 419.5 мм су. ст., иық пышақтарының айналу бұрышы 35°. Чам шахтасында жиналған деректерді талдау негізінде мақалада желдетудің жалпы жағдайына баға беріліп, тау-кен жұмыстарын жүргізу кезінде қауіпсіздікті қамтамасыз ететін желдету желісін жетілдіру шаралары ұсынылған. Сондай-ақ, үкі-екі негізгі желдеткіш станцияның жергілікті жұмыс режимдері анықталды, бұл Хе-Чам шахтасының 2025 жылға арналған жалпы желдету жоспарын жасауға негіз болады.

Негізгі сөздер: *көмір шахтасы, желдету жүйесі, ауа ағыны, ауа қысымы, көмір шахтасы.*

Оценка вентиляционной системы и предложения по улучшению вентиляционной сети угольной шахты Кхе-Чам, Вьетнам

К.Х. Нгуен[1], Т.Ч. Ву[1,2*], Д.Т. Ле[1,2], Ш.А. До[1], Ч.В. Дао[1,2], Ф.К. Ле[1,2]

[1]*Ханойский университет горного дела и геологии, Ханой, Вьетнам*
[2]*Научно-исследовательская группа: Устойчивое развитие горной науки, технологий и окружающей среды (SDM), Ханойский университет горного дела и геологии, Ханой, Вьетнам*

**Автор для корреспонденции: vutrungtien@humg.edu.vn*

Аннотация. Вентиляция при подземной разработке играет важнейшую роль в производственной деятельности, обеспечивая безопасность труда и поддержание надлежащих условий окружающей среды. Кроме того, вентиляция является одним из наиболее эффективных методов предотвращения взрывов метана и угольной пыли. В связи с этим необходимо ежегодно исследовать вентиляционную сеть и рассчитывать общие вентиляционные потребности для подземных шахт угольного бассейна Куангнинь. Учитывая производственный план и потребности в вентиляции угольной шахты Кхе-Чам, авторы провели обследование и оценку вентиляционной сети шахты, предложили решения по улучшению системы вентиляции, а также рассчитали вентиляционные параметры на 2025 год. Для достижения результатов, представленных в данной статье, использовались методы сбора, анализа и синтеза данных, полевые обследования, анализ и оценка результатов, а также численное моделирование с применением специализированного вентиляционного программного обеспечения для верификации расчетов. Для обеспечения вентиляции угольной шахты Кхе-Чам в 2025 году рекомендуется совместная работа двух главных вентиляторных станций - №1 на горизонте +35 и №2 на горизонте +112. Расчетные режимы их работы следующие: вентиляторная станция №1 на горизонте +35 – расход воздуха 193,72 м³/с, давление 448 мм вод. ст., угол поворота лопаток 40°; вентиляторная станция №2 на горизонте +112 – расход воздуха 155,8 м³/с, давление 419,5 мм вод. ст., угол поворота лопаток 35°. На основании анализа данных, собранных на шахте Кхе-Чам, в статье дана оценка общего состояния вентиляции и предложены меры по совершенствованию вентиляционной сети, обеспечивающие безопасность при ведении горных работ. Также определены совместные режимы работы двух основных вентиляторных станций, что служит основой для разработки общего плана вентиляции шахты Кхе-Чам на 2025 год.

Ключевые слова: *угольная шахта, вентиляционная система, расход воздуха, давление воздуха, угольная шахта Кхе-Чам.*

SATBAYEV UNIVERSITY

Engineering Journal of Satbayev University

Volume 147 (2025), Issue 3, 30-39

https://doi.org/10.51301/ejsu.2025.i3.05

Innovative approaches to the processing of ash and slag materials from the fuel and energy sector in the context of sustainable development

S.M. Nurmakova[1], U.K. Sarsembin[1], A. Dalbanbay[1], G.K. Abilova[2], B.K. Tusupova[3*], L.S. Kurbanova[3], G.B. Zharkimbaeva[1], M. Shanbayev[4]

[1]*Satbayev University, Almaty, Kazakhstan*
[2]*K. Zhubanov Aktobe regional university, Aktobe, Kazakhstan*
[3]*Al-Farabi Kazakh National University, Almaty, Kazakhstan*
[4]*G. Daukeev Almaty University of Power Engineering and Telecommunications, Almaty, Kazakhstan*

**Corresponding author: tussupova@yandex.ru*

Abstract. The whole world aims to reduce coal consumption, but despite such a policy, there are countries where its consumption continues to grow (China, India). If coal consumption grows, the volume of ash and slag waste (materials) that must be utilized and processed to obtain final products grows. The main elements included in the by-product of coal combustion are SiO_2, Al_2O_3, and Fe_2O_3. The paper provides a review of the use and processing of ash and slag materials for recycling as well as potential directions for their disposal: as well as potential directions for their disposal: cement production, geopolymer, in zeolite synthesis, microsphere separation, in agriculture, in land reclamation, in phytoremediation as reagents for water purification, in road construction for backfilling abandoned mines. The authors employed physicochemical analysis methods to confirm that the primary components of the material are SiO_2 (65.9%) and Al_2O_3 (22.5%). It has been established that a high proportion of silicon and aluminum can be an effective raw material for construction and geopolymer materials, as well as in the production of ceramic products. Availability of Fe_2O_3 (5.54%) suggests possibilities for its use in catalytic processes and pigment production. The alkaline reaction of the aqueous extract of the ash (pH = 9.25) correlates well with its chemical composition and confirms the presence of active alkaline components in the material. This alkaline nature of the ash favors geopolymerization processes and increases the material's reactivity when interacting with acidic activators. Additionally, the minor presence of TiO_2 (1.11%) may improve the mechanical properties of ash-based materials.

Keywords: *circular economy, green economy, industrial waste, ash and slag dumps, greenhouse gases, fly ash, ash and slag materials, fuel slag, ash and slag mixture.*

Received: 26 February 2025
Accepted: 15 June 2025
Available online: 30 June 2025

1. Introduction

Kazakhstan has committed itself to the international community to accelerate the reduction of the share of natural hydrocarbons in the country's energy balance, namely, replacing coal as the least environmentally friendly energy source. And this fact plays a huge role in strengthening the climate agenda (SDG 13), thereby calling for abandoning hydrocarbon energy sources in the future and achieving carbon neutrality by 2060 [1], linking this with alternative energy. However, another side to this issue is the low reliability of these energy resources, which depend on unstable weather conditions in Kazakhstan. Another fact of «acceptance» of coal is the final agreement following the UN Climate Conference (COP 26), which recorded a deal to «gradually reduce» rather than «stop» coal consumption. The agreement also calls for intensifying efforts to reduce the volume of electricity production at coal-fired power plants. Still, it specifies that this only applies to those that do not have carbon dioxide capture technologies. By the Decree of the President of the Republic of Kazakhstan dated June 10, 2024, amendments were made to the transition to a green economy. The document stated that .... «The transition to a green economy is the main way to achieve the SDGs, fulfilling the promised contribution of Kazakhstan to reducing greenhouse gas emissions under the Paris Agreement while ensuring economic and environmental sustainability...». Coal energy remains a significant sector of industry, ensuring energy savings for most settlements and industrial sectors. However, the volume of accumulated slag materials reaches more than 30 million tons, and this problem is acute in the transition of the legislative and regulatory environmental framework to international standards. Another critical aspect of ecological sustainability for coal energy is the concept of a Circular Economy, aimed at eliminating the dependence of economic growth on the vol-

s.nurmakova@satbayev.university; u.sarsembin@satbayev.university; a.dalbanbay@satbayev.university; guzelab82@mail.ru; tussupova@yandex.ru; k_lau@mail.ru; g.zharkimbayeva@satbayev.university; Shmaks_87@mail.ru
Engineering Journal of Satbayev University. eISSN 2959-2348. Published by Satbayev University

ume of natural resources and the transition from a linear economy to a circular one. This can be achieved by using existing funds and assets, materials and reserves, i.e., by reducing the volume of raw materials consumption and reducing the amount of waste generated [2].

Using coal as a primary fuel source results in a considerable amount of waste, depending on the method of capture and removal, such as slag, fly ash, and other by-products that must be disposed of and processed by the natural resource user. In a few countries, ash and slag materials (ASM) are a by-product of coal combustion, which, due to the wide variety of solid fuels, different combustion conditions, as well as different methods of capture and removal, differ in chemical and mineralogical composition, physical properties, melting point, radioactivity and other characteristics [3].

According to the legislation of Kazakhstan, namely Article 130 [4], ash and slag are classified as «technogenic mineral formations (TMF) of energy production in the production of electric and (or) thermal energy by generating units». According to the Waste Classifier, ash and slag are non-hazardous waste. That is, we can observe a contradiction in the regulatory framework of the Republic of Kazakhstan, where ash and slag are classified as both TMF and «waste». For successful management of ash and slag at the enterprises of the fuel and energy complex of the Republic of Kazakhstan, the first step should be a legislative change in the status of ash and slag and the use of the term «ash and slag materials» or «by-product of coal combustion», which can be used in various sectors of the economy of the Republic of Kazakhstan.

2. Materials and methods

During the combustion of solid fuel, and depending on the method of capture and removal, the following coal combustion by-products are formed:

1) fly ash – finely dispersed material (particle size from 3-5 to 100-150 μm), formed from the mineral part of pulverized fuel, captured by special devices from the flue gases of thermal power plants;

2) fuel slag – aggregated and fused ash particles from 0.15 to 40 mm in size;

3) ash and slag mixture – a mixture of fly ash and slag formed during their joint removal to the dump.

The formed coal combustion by-products (CCB) are shown in Figure 1, and their main types are shown in gaseous and solid states.

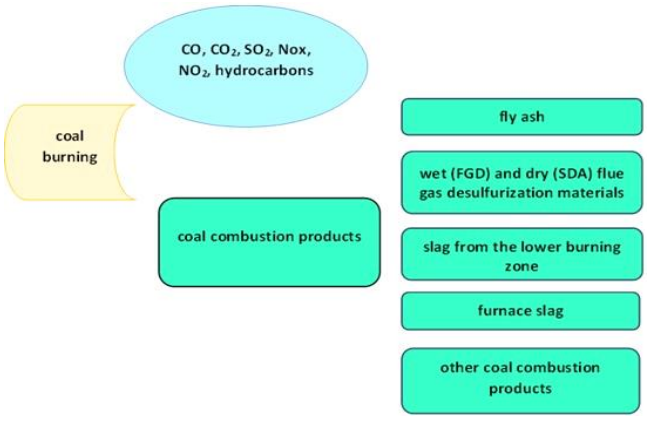

Figure 1. Classification of coal combustion products according to WWCCPN [5]

Solid CCBs include fly ash, slag from the lower combustion zone, fuel slag, fluidized bed (FB) ash, and flue gas desulphurization products formed by dry and wet methods [6]. Here are several key areas where ash and slag materials can effectively utilize.

2.1. Use of CCBs in the production of construction materials

ASM has found the most excellent application in construction in cement and concrete technologies. Using ash and slag reduces the cost of production of construction materials (cement, dry mortar, concrete, foam blocks, bricks, paving slabs). To reduce the environmental impact associated with cement production (concrete), the use of other additives to cement, in addition to Portland cement clinker, is currently increasing. Ash and slag can be used as additives. The primary process in cement and concrete production technology leads to significant CO_2 emissions during the decomposition of limestone into calcium oxide at high temperatures created during combustion. For each kg of cement produced, there is 0.5-0.9 kg of fly ash, which, according to the authors, is one of the best solutions for reducing the consumption of fossil mineral resources, because a large amount of ash and slag can be obtained at a low price. Instead of disposing of ash and slag at landfills, they can be used in cement production, which is effective from an environmental and economic point of view and meets sustainable development goals.

This paper [7] discusses the use of fly ash in cement production. Study [8] presents data on the application of fly ash in concrete and the effect of a specific percentage content on fresh and hardened concrete (mechanical properties and durability, microstructure of fly ash, impact of the type and size of fly ash particles). In addition to fly ash with a high SiO_2 content, granulated blast furnace slag (GBFS) can also be used as an additive to Portland cement clinker [9-15]. The use of GBFS began in 1865 in Germany, while fly ash dates back to the beginning of the 20th century [16, 17]. The world production of these industrial by-products is approximately 900-1000 million tons for fly ash and about 140-330 million tons for blast furnace slag [18]. Both discussed components, like Portland cement clinkers, are produced in a high-temperature process and are commonly used as central components in cement and/or as concrete components.

The utilization rate of granulated blast furnace slag in the composition of cement and concrete is more than 90%, while fly ash is around 30% [19]. The relatively low utilization of fly ash is due to its variable quality and different coal combustion methods, such as combining coal combustion with a dry flue gas desulphurization process in fluidized bed boilers, etc. Study [20] analyzes the main trends regarding fly ash and granulated slag use in cement, concrete and other binder composites. Attention is also given to the properties and potential applications of using fly ash in cement composites as a product of other coal combustion methods and ash obtained from the combustion of alternative fuels, mainly biomass.

Information about «green concrete» is mentioned in the article [21]. The authors developed a technology for processing fly ash and carbon dioxide into a new type of concrete. «Green» concrete was created from a semi-dry mixture of fly ash by pressing, and then it was cemented and hardened by a hydration reaction and accelerated carbonation. The authors studied the role of Na_2CO_3 activation by «accelerated carbonation» during chemical reactions and phase

transformations, by changing the mechanical properties and microstructure of new concrete from waste. Accelerated carbonation (up to 4 hours) improved the mechanical strength and microstructural integrity of concrete from fly ash, which worked more effectively with the addition of Na_2CO_3. As a result of activation of the fly ash mixture with sodium carbonate, various hydration products were obtained due to increased alkalinity and dissociated $CO3^{2-}$ ions. Therefore, accelerated carbonation transformed the initial hydration products, contributing to natural hardening (carbonation)—microscopic crystalline phases formed by carbonation mixed with hydrated matrix phases. As a result, the carbonate products formed in situ acted as cementing agents. They contributed to creating a new cement-like and binding microstructure in concrete obtained from waste without using traditional cement. The work's experimental part confirmed this method's technical efficiency, demonstrating the potential for recycling significant volumes of solid waste from landfills. The process allows for producing new types of cement-free carbon-activated concrete, which opens prospects for more environmentally friendly, urban and infrastructural construction.

The production of geopolymers is another area of the construction industry. Anti-slip materials are formed due to the alkaline activation of inorganic compounds rich in Al_2O_3 and SiO_2. This process includes the formation of a three-dimensional structure of SiO_4 and AlO_4. Geopolymer is a modified binder for Portland cement concrete obtained from fly ash. It exhibits high heat and chemical resistance, making it an excellent choice for constructing rigid pavements at air bases [22].

In study [23], fly ash is used for the production of bricks, the content of which improves the compressive strength of the brick and improves its frost resistance

The use of CCBs in road construction is a well-known fact, which is regulated by regulatory documents:

– GOST 9128-97 Asphalt concrete mixtures for roads, airfields and asphalt concrete.

– GOST 23558-94 Crushed stone-gravel-sand mixtures and soils treated with inorganic road and airfield construction binders.

– GOST 30491-97 Organic and mineral mixtures and soils reinforced with organic binders for road and airfield construction.

– ODM 218.2.031-2013 Methodological recommendations for using fly ash and ash-slag mixtures from coal combustion at thermal power plants in road construction.

2.2. Use of CCBs as backfill material in mines

Voids formed during the underground extraction of mineral resources in depleted mines can lead to artificial disasters, such as flooding due to subterranean water breakthroughs or earthquakes caused by mine collapses. Depleted mine spaces are often filled with a mixture of cement, sand, and gravel; however, this method is expensive and does not always restore the required strength and structure of the rock mass. As an alternative solution, industrial waste mixtures known as backfilling material fill abandoned mine spaces [24]. This waste mass helps prevent ground subsidence, increases the stability of underground structures by managing rock pressure, and prevents deformation of the overlying strata up to the surface. It also eliminates ore liquefaction, optimizes waste disposal methods, and offers numerous other advantages [25-30]. Backfilling materials may include mine tailings and special binders prepared at the surface. Naturally, any neutral industrial waste can be used for this purpose (e.g., fly ash and slag materials, construction waste, etc.). The advantages of this technology include easier roof control during ore extraction and the utilization of industrial waste at mining sites.

Backfill materials can be divided into two main groups. The first is cementless backfill material, and the second is cement [31, 32]. When using backfill material without cement, the waste material is filled without adding any binder. When using cemented backfill, a specific binder, such as Portland cement, is added to the solid waste mixture [33].

One type of cemented backfilling material is paste backfill [33-35]. A significant number of studies in the field of waste management focus on various binders and alternative pozzolanic materials [33], one of which is paste backfill. This material has been widely adopted worldwide and is currently in high demand. The advantages of paste backfill lie in its technical and economic benefits and its ability to incorporate large volumes of industrial waste compared to other backfilling technologies used in mining. Globally, more than 100 mines utilize this backfilling method [36].

In the study [37], the authors demonstrated that there are research results on the development of paste backfill for mines using tailings, fly ash, and slag. The potential for applying paste backfill in underground mines worldwide, particularly in India, was highlighted. It was noted that many studies have been conducted on strength properties, structural changes, economic feasibility, and leaching behavior of backfilling materials. However, the question of how strength evolves remains open.

2.3. Use of CCBs in agriculture, land reclamation and phytoremediation

Flue Gas Desulfurization Gypsum is a gypsum obtained by cleaning the flue gases of thermal power plants from SO_2 and SO_3 using the lime method with $Ca(OH)_2$:

$$SO_2+Ca(OH)_2+½O_2 \rightarrow CaSO_4 \cdot 2H_2O.$$

The resulting $CaSO_4 \cdot 2H_2O$ (calcium sulfate dihydrate) is an analogue of natural gypsum widely used in agriculture as a fertilizer.

In the study [38], the authors compare FGD gypsum's and natural gypsum's chemical properties, showing that these substances exhibit similar behavior and effects on the studied crops. However, FGD gypsum, which has a finer particle size, possesses a higher degree of purity than natural gypsum.

There are three main uses of gypsum in agriculture, according to the US EPA. (2008) Agricultural uses for flue gas desulfurization (FGD) gypsum, EPA530-F-08-009 [39]:

1. Source of nutrients for plants;

2. To improve the physical and chemical properties of the soil;

3. To change the structure of the soil. This promotes the formation of large soil aggregates, thereby reducing soil erosion and leaching of nutrients. It also supports rapid water absorption, reducing surface runoff of sediments with pesticides and other pollutants, preventing them from entering water resources.

As an example of nutrient application, studies on the yield of alfalfa and soybeans can be cited [38], where yields increased following the application of FGD gypsum. FGD gypsum was also studied on alfalfa crops [40], revealing that

yields improved on soils with an acidic subsoil layer without affecting the concentration of heavy metals. However, the fluoride concentration in the plant biomass was reduced, leading to a «significant decrease in health risks for animals feeding on these plants». It was noted that using gypsum in highly sandy soils may increase the leaching rate of magnesium (Mg) and potassium (K) through the soil profile, potentially resulting in deficiencies of these nutrients.

The study [41] demonstrated the benefits of applying FGD gypsum and humic acid to improve the physicochemical properties of soil and enhance canola crop productivity.

According to Buckley, M.E., & Wolkowski, R.P., soybean yields increased with gypsum application rates up to 1.2 tons per hectare, but exceeding this rate led to a decline in yields to levels observed in the control plots (without fertilizer application) [42].

In study [43], an evaluation was conducted based on two summer experiments on using FGD gypsum to effectively reclaim flood-prone lands with high salinity and improve herbaceous and woody plant growth on these lands. The rate and extent of reclamation were assessed, driven by the accelerated desalination process resulting from the exchange of calcium ions (Ca^{2+}) with sodium ions (Na^{+}).

However, an alternative perspective is presented in [44], which states that the content of essential nutrients such as nitrogen, phosphorus, potassium, sulfur, calcium, and magnesium is low in waste materials, making fly ash and slag «biologically sterile». The lack of plant-available organic substances, particularly the low content of humic acids in ash and slug waste, indicates that their use as a nutrient source for plants is limited. The use of ash and slag waste as a substitute for traditionally applied liming materials for periodic and maintenance liming of acidic soils is also restricted. Studies [45] show that applying ash and slag waste may improve soil structure and water-physical properties. However, its use as a soil conditioner should be evaluated case by case, due to the potential for exceeding provisional permissible concentrations of arsenic and cadmium, which are classified as Class I hazardous elements. Study [46] also explores fly ash as a soil additive, emphasizing its physical characteristics, including structure, water retention capacity, bulk density, and pH, making it a promising material for agricultural purposes. Despite its potential benefits for agricultural use, including addressing nutrient deficiencies and pest control, fly ash can also contain toxic heavy metals and radioactive elements. Therefore, the amount and method of fly ash application depend on factors such as soil type, crop variety, prevailing agroclimatic conditions, and the specific properties of the ash itself. Another critical aspect of such studies is monitoring both qualitative and quantitative soil parameters, plant growth, and the content and bioaccumulation of heavy metals in environmental components due to excessive fly ash application [45-47].

Another promising direction for using coal combustion by-products (CCB) is phytoremediation, which is used to restore degraded lands, such as ash disposal sites. This technology involves using local or native plant species (shrubs, trees, grasses, aquatic plants) and associated microorganisms, as well as chelating agents to enhance the uptake of metals from waste by plants [47, 48]. The review [49] proposes the reclamation of ash and slag disposal sites through vegetation, shrub plantings, and microbial inoculants. Microbial consortia play a crucial role in the physicochemical transformation of ash materials, while the application of organic substances promotes the establishment of plant cover. The morphological, physiological, and antioxidant responses of plants grown on ash disposal sites are examined in detail. The review identifies plant species demonstrating high biomass production, strong nitrogen-fixing capabilities, and soil microbial diversity development support. These studies focus on the challenge of restoring vast areas of ash dumps to foster ecosystem resilience and return degraded lands to productive use – an approach aligned with the principles of the circular economy.

3. Results and discussion

Ash and slag materials (ASM), according to the Subsoil Use Code of the Republic of Kazakhstan, are classified as man-made mineral formations – products of pyrotechnological processes occurring in the combustion chambers of thermal power plants (TPPs). Depending on the type of solid fuel and the physicochemical processes occurring in these boiler units, ash and slag formation can occur without melt formation, partial melting, or complete melting of the original components. The release of gaseous and vaporous substances, decarbonization, melting, crystallization, and silicate formation of the initial raw material accompany this. Thus, the choice of utilization methods for ASM depends on its composition, fuel characteristics, and physicochemical and mechanical properties. The research used ash and slag materials from TPP-2, which were removed as slurry and pumped through a pipeline system to a designated area («map») of the ash and slag disposal site.

X-ray phase analysis of fly ash from the thermal power plant (Figure 2) showed that its crystalline structure predominantly consists of the following mineral phases: mullite ($Al_{4.64}Si_{1.36}O_{9.68}$, 47.4%), quartz ($SiO_2$, 41.0%), magnetite ($Fe_{2.946}O_4$, 3.7%), maghemite ($Fe_2O_3$, 3.5%), calcite ($CaCO_3$, 2.9%), and titanium dioxide (TiO_2, 1.6%). The predominance of aluminosilicate minerals (mullite and quartz) is due to the high content of SiO_2 and Al_2O_3 in the original coal. At the same time, the presence of iron oxides (magnetite, hematite), calcium (calcite), and titanium reflects the composition of the ash-forming components of the fuel. The identified phase composition of fly ash determines its physicochemical properties and potential application areas, for example, as a raw material for producing geopolymers, ceramics and construction materials.

X-ray fluorescence (XRF) analysis revealed that the main components of fly ash are SiO_2 (65.9%) and Al_2O_3 (22.5%). The high proportion of silicon and aluminum suggests that ash may be an effective raw material for building geopolymer materials and some ceramic applications. The presence of Fe_2O_3 (5.54%) opens up possibilities for its use in catalytic processes and pigment production.

The presence of alkaline earth and alkali metal oxides - CaO (1.94%), MgO (0.572%), Na_2O (0.913%) and K_2O (0.559%) causes the alkaline reaction of the aqueous extract of ash (pH = 9.25). This pH value correlates well with the chemical composition and confirms the presence of active alkaline components in the material. The alkaline nature of ash favors geopolymerization processes and increases the material's reactivity when interacting with acidic activators.

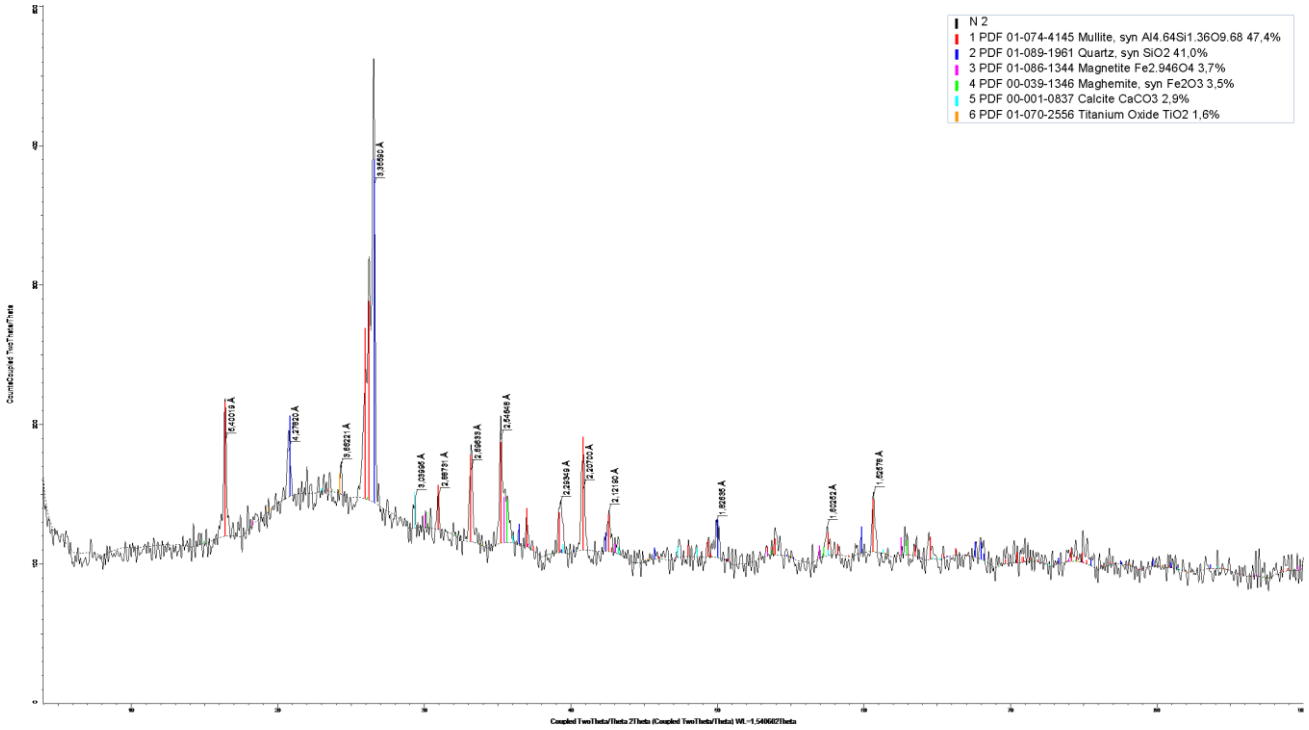

Figure 2. X-ray phase analysis of thermal power plant ash

TiO_2 (1.11%) can improve the mechanical properties of ash-based materials. The revealed ratio of the main components and the alkaline nature of the material determine the main areas of its practical application:

– as a precursor for the synthesis of geopolymers,

– as an active mineral additive in building mixtures,

– as a raw material for the production of ceramic materials,

– as a potential component of catalytic systems.

Ash and slag waste from the combustion of Ekibastuz coal at the Thermal Power Plant-2 in Almaty has the composition shown in Table 1.

Table 1. Results of X-ray fluorescence analysis of the main elemental composition of the initial samples of ash and slag waste at TPP-2 in Almaty

Sample name	Composition, %											
	K	Ca	Ti	Sr	Mn	Si	Fe	O	Zn	Al	Zr	C
Ash slag	0.185	1.72	1.06	0.017	0.17	23.91	8.75	49.9	0.006	11.3	0.016	1.75
Fine ash	0.166	1.14	1.12	0.016	0.067	24.3	2.58	50.47	0.03	12.45	0.017	6.64
Slag	0.174	1.49	1.43	0.031	0.08	26.02	4.54	52.2	0.02	12.89	0.02	0.19

As can be seen from the table, ash and slag contain the most silicon, aluminum, and iron. The bulk density of ash and slag is 1.07 g/cm^3; the sieve analysis results are presented in Table 2.

Table 2. Results of the sieve analysis of waste from Almaty TPP-2

Size, mm	Outlet, %
+1	0.044
0.5-1	0.044
0.2-0.5	7.08
0.1-0.2	35.1
0.071-0.1	23.7
-0.071	34.0
Total	100

The primary particle size class is -0.2+0 mm (92.83%). Considering the required size class (-0+0.74 mm), during the processing of technogenic raw materials, the proportion of material that involves grinding will not exceed 66.0%.

The study of aluminosilicate microspheres in ash and slag waste was carried out using a JEOL scanning electron microscope (Japan), equipped with an energy-dispersive X-ray analyzer «JCM-6000 PLUS» (Figures 3, 4).

Aluminosilicate microspheres are glass-crystalline aluminosilicate beads formed during high-temperature flame combustion of coal. They are the most valuable components of ash waste from thermal power plants. These are hollow, nearly perfectly shaped silicate spheres with smooth surfaces, ranging in diameter from 10 to several hundred micrometers, with an average of about 100 μm. This raw material is valuable for the production of construction materials. It can also be used as an inert material without additional processing.

Free aluminosilicate microspheres make up about 30% of the sample volume, while most of the sample consists of fragments of loose porous slags and, less frequently, individual crystals. In many cases, accumulations of the smallest microspheres are observed in the pores of the slag.

The size of aluminosilicate microspheres typically ranges from 1-3 micrometers (and fractions of a micrometer) up to 30-40 μm and rarely up to 100 μm. In addition to aluminosilicate microspheres, the sample also contains iron-rich microspheres (which appear light gray in the images). Alongside perfectly spherical formations, ellipsoidal, bulbous, globular shapes, «sphere-in-sphere» structures, fused aggregates of two or more spheres, and broken spheres and hemispheres.

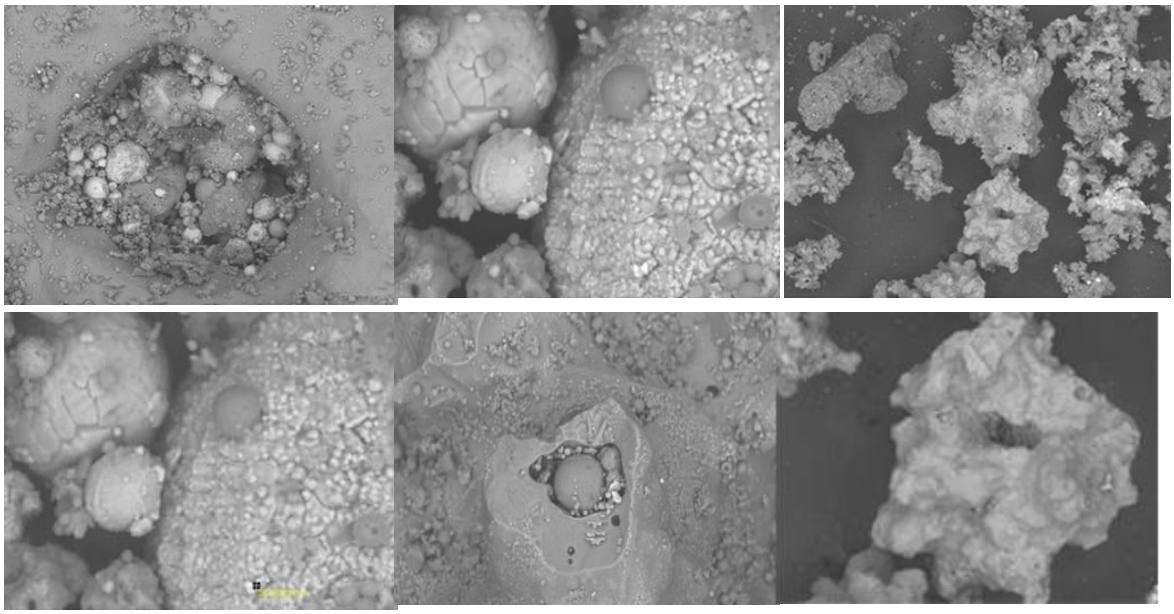

Figure 3. Slag particles

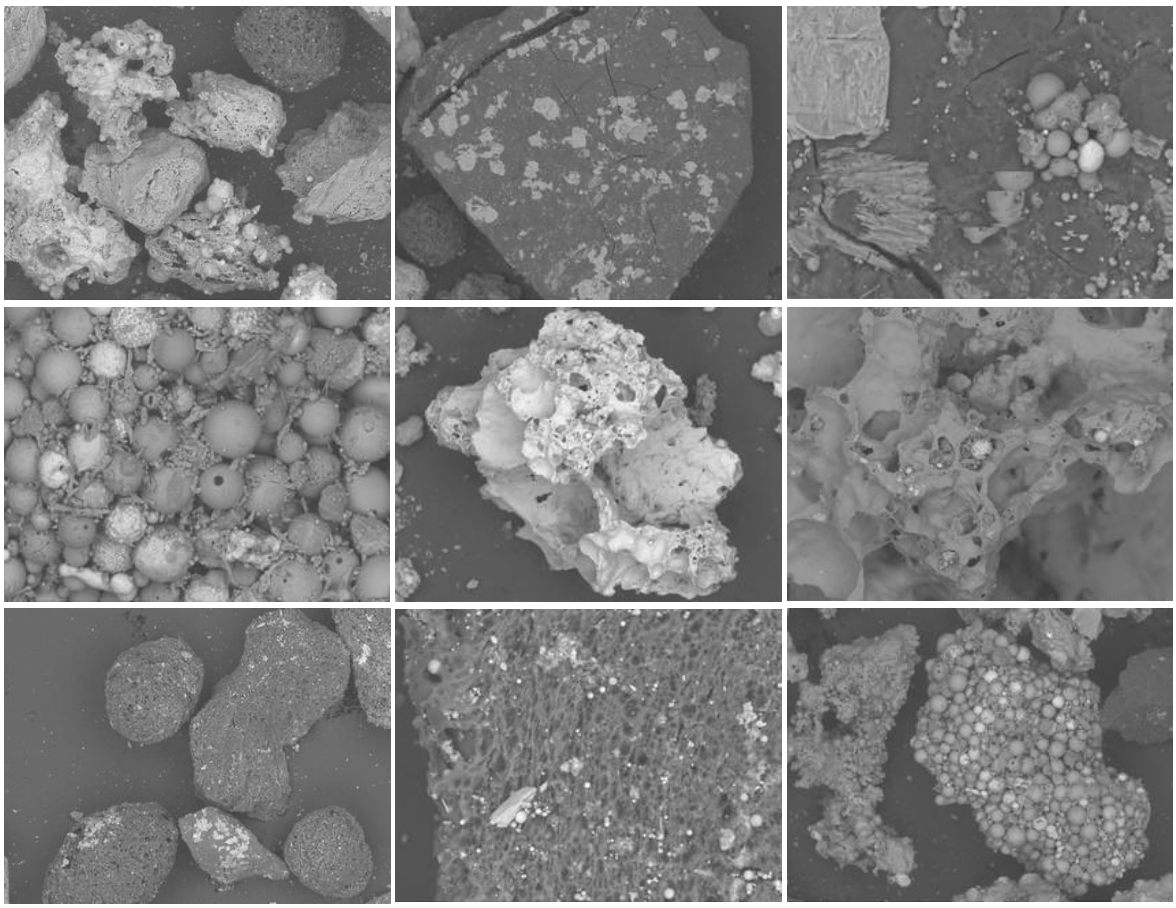

Figure 4. Different morphological types

The surface of aluminosilicate microspheres is generally smooth and dense, but it may also be porous, rough, or irregular (in cases of encrustations of different compositions or tiny microspheres). The surface of iron-rich microspheres is typically textured or ribbed due to the dense, patterned intergrowth of magnetite crystals; it may also be smooth when the microspheres are composed of iron with impurities or aluminosilicates with a high iron content. The composition of the aluminosilicate microspheres studied is somewhat variable. While the dominant elements remain Al, Si, and oxygen, the content of Mg, Ca, and Fe varies – for example, Ca may reach up to 17% by weight, and Mg up to 13% by weight. The composition also includes varying amounts of K, Na, Ti, S, P, and Cl. In some cases, the mineral composition of the microspheres is heterogeneous, showing tiny inclusions of carbonaceous material or fine disseminated intermetallic compounds such as Pb-Sn or Fe-Cr.

4. Conclusions

Analysis of scientific publications by foreign authors has led us to conclude that, first and foremost, ash and slag materials should be excluded from the «waste» category, as they represent a versatile material suitable for use in various industrial sectors. Moreover, valuable components extracted from them can be used to produce a wide range of products.

In addition, integrating coal combustion products from thermal power plants into industrial circulation will reduce their accumulation in ash disposal sites and prevent the storage of new volumes. This will contribute to the creation of zero-waste production systems and reduce the environmental burden of the fuel and energy sector. Research conducted at Satbayev University on ash and slag waste from TPP-2 in Almaty allows us to conclude that these materials can be used for the following purposes:

– as a precursor for the synthesis of geopolymers
– as an active mineral additive in building mixtures
– as a raw material for the production of ceramic materials.

Author contributions

Conceptualization: GKA, SMN, UKS; Data curation: BKT; Formal analysis: LSK, GBZ; Funding acquisition: GKA, UKS, SMN; Investigation: AD, SMN, UKS; Methodology: SMN, UKS; Project administration: GKA; Resources: AD; Software: GBZ; Supervision: SMN; Validation: AD; Visualization: GBZ, MS; Writing – original draft: SMN; Writing – review & editing: BKT, LSK. All authors have read and agreed to the published version of the manuscript.

Funding

This research was carried out within the framework of the Targeted Funding Program of the Science Committee of the Ministry of Science and Higher Education of the Republic of Kazakhstan for 2024–2026, under the priority area: Ecology, Environment, and Rational Use of Natural Resources, project number BR124992882 «Development of New Technologies for the Processing of Technogenic Waste to improve the Environmental Situation in the Region».

Acknowledgements

The authors would like to express their sincere gratitude to the reviewers for their constructive comments and valuable suggestions, significantly improving the manuscript.

Conflict of interest

The authors declare no conflict of interest.

Data availability statement

The original contributions presented in this study are included in the article. Further inquiries can be directed to the corresponding author.

References

[1] On approval of the Strategy for achieving carbon neutrality of the Republic of Kazakhstan until 2060 (Decree No. 121). *Retrieved from:* https://adilet.zan.kz/rus/docs/U2300000121

[2] Concept for the transition of the Republic of Kazakhstan to a «green economy». *Retrieved from:* https://adilet.zan.kz/rus/docs/U1300000577

[3] Federal Road Agency. (2014). ODM 218.2.031-2013: Methodological recommendations for the use of fly ash and ash-slag mixtures from coal combustion at thermal power plants in road construction. Moscow

[4] Code of the Republic of Kazakhstan «On Subsoil and Subsoil Use» (No. 125-VI ZRK). *Retrieved from:* https://adilet.zan.kz/rus/docs/K1700000125

[5] Worldwide Coal Combustion Products Network. (n.d.). CCP basics. *Retrieved from:* http://wwccpn.org/ccp_basics.html

[6] World of Coal Ash. (2024). Craig Heidrich, Joachim Feuerborn. Global opportunities and challenges for coal combustion products with a circular economy. *Retrieved from:* https://worldofcoalash.org/wp-content/uploads/2022/09/global-opportunities-andchallenges-for-coal-combustion-products-with-a-circular-economy.pdf

[7] Kumar, N.D., Abhilash, P.P., Singh, R., Kumar, R., & Kumar, V. (2022). Fly ash for sustainable construction: A review of fly ash concrete and its beneficial use case studies. *Cleaner Materials*, (6), 100143. https://doi.org/10.1016/j.clema.2022.100143

[8] Zhang, Y., Smith, J., & Brown, L. (2022). Sustainable applications of coal combustion products in a circular economy. Environmental. *Advances*, (10), 100103.

[9] Siddique, R., & Cachim, P. (2018). Waste and Supplementary Cementitious Materials in Concrete: Characterisation, Properties and Application. *A volume in Woodhead Publishing Series in Civil and Structural Engineering*. https://doi.org/10.1016/C2016-0-04037-8

[10] Nguyen, H.A., Chang, T.P., Shih, J.Y., Chen, C.T., & Nguyen, T.D. (2015). Influence of circulating fluidized bed combustion (CFBC) fly ash on properties of modified high volume low calcium fly ash (HVFA) cement paste. *Construction and Building Materials*, (91), 208-215. https://doi.org/10.1016/j.conbuildmat.2015.05.075

[11] Giergiczny, Z., & Król, A.. (2008). Review Immobilization of heavy metals (Pb, Cu, Cr, Zn, Cd, Mn) in the mineral additions containing concrete composites. *Journal of Hazardous Materials*, *160*(2-3), 247-255. https://doi.org/10.1016/j.jhazmat.2008.03.007

[12] Fuller, A., Stegmaier, M., Schulz, N., Menke, M., Schellhorn, H., Knödler, F., Maier, J., & Scheffknecht, G. (2018). Use of wood dust fly ash from an industrial pulverized fuel facility for rendering. *Construction and Building Materials*, (189), 825-848. https://doi.org/10.1016/j.conbuildmat.2018.09.016

[13] Magdziarz, A., Dalai, A.K., & Koziński, J.A. (2016). Chemical composition, character and reactivity of renewable fuel ashes. *Fuel*, (176), 135-145. https://doi.org/10.1016/j.fuel.2016.02.069

[14] Martirena, F., & Monzó, J. (2018). Vegetable ashes as Supplementary Cementitious Materials. *Cement and Concrete Research*, (114), 57-64. https://doi.org/10.1016/j.cemconres.2017.08.015

[15] Nguyen, T.D., & Chang, T.P. (2015). Influence of circulating fluidized bed combustion (CFBC) fly ash on properties of modified high volume low calcium fly ash (HVFA) cement paste. *Construction and Building Materials*, (98), 448-455. https://doi.org/10.1016/j.conbuildmat.2015.05.075

[16] Nurpeisova, M., Estemesov, Z., Gabbasov, S., Ashimova, A., & Bek, A. (2023). Studying the properties of ash and slag waste for use in the manufacture of construction products. Mining of Mineral Deposits, 17(3), 102-109. https://doi.org/10.33271/mining17.03.102

[17] Rivera, F., Martínez, P., Castro, J., & López, M. (2015). Massive volume fly-ash concrete: A more sustainable material with fly ash replacing cement and aggregates. *Cement and Concrete Composites*, *63*, 104-112. https://doi.org/10.1016/j.cemconcomp.2015.08.001

[18] Marinković, S., & Dragaš, J. (2018). Fly ash. In K. M. A. Hossain & M. Lachemi (Eds.), Waste and Supplementary

Cementitious *Materials in Concrete, Elsevier*. https://doi.org/10.1016/B978-0-08-102156-9.00011-0

[19] Giergiczny, Z. (2019). Fly ash and slag. *Cement and Concrete Research*, (124), 105826. https://doi.org/10.1016/j.cemconres.2019.105826

[20] Liu, E., Kashwani, G., & Li, L. (2020). Transformation of industrial solid wastes into carbon-infused infrastructure materials. *Journal of Cleaner Production*, (260), 120890. https://doi.org/10.1016/j.jclepro.2020.120890

[21] Shill, S.K., Al-Deen, S., Ashraf, M., & Hutchison, W. (2020). Resistance of fly ash-based geopolymer mortar to both chemicals and high thermal cycles simultaneously. *Construction and Building Materials*, (239), 117886. https://doi.org/10.1016/j.conbuildmat.2019.117886

[22] Lingling, X., Wei, G., Tao, W., & Nanru, Y. (2005). Study on fired bricks with replacing clay by fly ash in high volume ratio. *Construction and Building Materials*, *19*(3), 243-247. https://doi.org/10.1016/j.conbuildmat.2004.05.017

[23] Panchal, S., Deb, D., & Sreenivas, T. (2018). Mill tailings based composites as paste backfill in mines of U-bearing dolomitic limestone ore. *Journal of Rock Mechanics and Geotechnical Engineering*, *10*(2), 310-322. https://doi.org/10.1016/j.jrmge.2017.08.004

[24] Senapati, P.K., Mishra, B.K., & Parida, A. (2013). Analysis of friction mechanism and homogeneity of suspended load for high concentration fly ash & bottom ash mixture slurry using rheological and pipeline experimental data. *Powder Technology*, *250*(3), 154-163. https://doi.org/10.1016/j.powtec.2013.10.014

[25] Behera, K., Ghosh, C.N., Mishra, D.P., Singh, P., Mishra, B.K., Buragohain, J., & Mandal, P.K. (2020). Strength development and microstructural investigation of lead-zinc mill tailings based paste backfill with fly ash as alternative binder. *Cement and Concrete Composites*, (109), 103553. https://doi.org/10.1016/j.cemconcomp.2020.103553

[26] Xu, W., Li, Q., & Liu, B. (2020). Coupled effect of curing temperature and age on compressive behavior, microstructure and ultrasonic properties of cemented tailings backfill. *Construction and Building Materials*, (237), 117738. https://doi.org/10.1016/j.conbuildmat.2019.117738

[27] Benzaazoua, M., Belem, T., & Bussière, B. (2002). Chemical factors that influence the performance of mine sulphidic paste backfill. *Cement and Concrete Research*, *32*(7), 1133-1144. https://doi.org/10.1016/S0008-8846(02)00752-4

[28] Ouellet, S., Bussière, B., Aubertin, M., & Benzaazoua, M. (2007). Microstructural evolution of cemented paste backfill: Mercury intrusion porosimetry test results. *Cement and Concrete Research*, *37*(12), 1654-1665. https://doi.org/10.1016/j.cemconres.2007.08.016

[29] Wu, D., Hou, Y., Deng, T., Chen, Y., & Zhao, X. (2017). Thermal, hydraulic and mechanical performances of cemented coal gangue-fly ash backfill. *International Journal of Mineral Processing*, (162), 12-18. https://doi.org/10.1016/j.minpro.2017.03.001

[30] Zheng, S., & Zhu, J. (2016). Utilization of limestone powder and water-reducing admixture in cemented paste backfill of coarse copper mine tailings. *Construction and Building Materials*, (126), 25-33. https://doi.org/10.1016/j.conbuildmat.2016.07.055

[31] Ghirian, A., & Fall, M. (2013). Coupled thermo-hydro-mechanical-chemical behaviour of cemented paste backfill in column experiments. *Part I: Physical, hydraulic and thermal processes and characteristics. Engineering Geology*, *164*, 195-207. https://doi.org/10.1016/j.enggeo.2013.01.015

[32] Koupouli, N.J.F., Belem, T., Rivard, P., & Effenguet, H. (2016). Direct shear tests on cemented paste backfill-rock wall and cemented paste backfill-backfill interfaces. *Journal of Rock Mechanics and Geotechnical Engineering*, *8*(4), 472-479. https://doi.org/10.1016/j.jrmge.2016.02.001

[33] Ercikdi, B., Baki, H., & İzki, M. (2013). Effect of desliming of sulphide-rich mill tailings on the long-term strength of cemented paste backfill. *Journal of Environmental Management*, (115), 5-13. https://doi.org/10.1016/j.jenvman.2012.11.014

[34] Zhang, L., Zhu, H., Zhou, B., & Zhang, M. (2014). Influence of fly ash and its mean particle size on certain engineering properties of cement composite mortars. *Powder Technology*, (253), 183-193. https://doi.org/10.1016/j.powtec.2013.10.014

[35] Behera, M., & Mishra, B. (2021). Utilization of mill tailings, fly ash, and slag as mine paste backfill material: Review and future perspective. *Construction and Building Materials*, (309), 125120. https://doi.org/10.1016/j.conbuildmat.2021.125120

[36] Chen, Z.W., Xiao, Y., Pang, L., Zeng, W.B., & Wu, S.P. (2014). Experimental assessment of flue gas desulfurization residues and basic oxygen furnace slag on fatigue and moisture resistance of HMA. *Fatigue and Fracture of Engineering Materials and Structures*, (37), 1242-1253. https://doi.org/10.1111/ffe.12205

[37] US Environmental Protection Agency (EPA). (2008). Agricultural uses for flue gas desulfurization (FGD) gypsum (EPA530-F-08-009). *U.S. Environmental Protection Agency.*

[38] Dhadse, S. (2024). Utilization of fly ash in agriculture: Perspectives and challenges. *Journal of Materials and Environmental Science*, *15*(7), 1038-1050.

[39] Nan, J., Chen, X., Wang, X., Lashari, M. S., Wang, Y., Guo, Z., & Du, Z. (2016). Effects of applying flue gas desulfurization gypsum and humic acid on soil physicochemical properties and rapeseed yield of a saline-sodic cropland in the eastern coastal area of China. *Journal of Soils and Sediments*, (16), 38-50. https://doi.org/10.1007/s11368-015-1186-3

[40] Buckley, M.E., & Wolkowski, R.P. (2012). Effect of land application of FGD gypsum on plant yield and crop nutrient concentration. *Crop Management.* https://doi.org/10.1094/CM2012-0925-01-RS

[41] Li, X., Mao, Y., & Liu, X. (2015). Flue gas desulfurization gypsum application for enhancing the desalination of reclaimed tidal lands. *Ecological Engineering*, *82*, 566-570. https://doi.org/10.1016/j.ecoleng.2015.04.010

[42] Chukaeva, M.A., Matveeva, V.A., & Sverchkov, I.P. (2022). Complex processing of high-carbon ash and slag waste. *Journal of Mining Institute*, 000, 1-8. https://doi.org/10.31897/PMI.2022.5

[43] Grebenshchikova, E.A., Yust, N.A., & Pykhteeva, M.A. (2016). The influence of chemical melioration by adding ash and slag waste on the physicochemical properties of the soil. *Bulletin of KrasSAU*, (6), 3-8.

[44] Dhadse, S. (2024). Utilization of Fly Ash in Agriculture: Perspectives and Challenges. *Journal of Materials and Environmental Science*, *15*(7), 1038-1050.

[45] Asante-Badu, B., Kgorutla, L.E., Li, S.S., Danso, P.O., Xue, Z., & Qiang, G. (2020). Phytoremediation of organic and inorganic compounds in natural and agricultural environments: A review. *Applied Ecology and Environmental Research*, *18*(5), 6875-6904. https://doi.org/10.15666/aeer/1805_68756904

[46] Banda, M., Matabane, L., & Munyengabe, A. (2024). A Phytoremediation Approach for the Restoration of Coal Fly Ash Polluted Sites: A Review. https://doi.org/10.20944/preprints202406.0768.v1

[47] Pandey, V.C., Abhilash, P.C., & Singh, N. (2009). The Indian perspective of utilizing fly ash in phytoremediation, phytomanagement and biomass production. *Journal of Environmental Management*, *90* (10), 2943-2958. https://doi.org/10.1016/j.jenvman.2009.05.001

[48] De Abreu, C.A., Coscione, A.R., Pires, A.M., & Paz-Ferreiro, J. (2012). Phytoremediation of a soil contaminated by heavy metals and boron using castor oil plants and organic matter amendments. *Journal of Geochemical Exploration*, (123), 3-7. https://doi.org/10.1016/j.gexplo.2012.04.013

[49] Yadav, S., Pandey, V.C., & Singh, L. (2021). Ecological restoration of fly-ash disposal areas Challenges and opportunities, 32(16). 4453-4471. https://doi.org/10.1002/ldr.4064

Тұрақты даму контекстінде отын-энергетика кешенінің күл-қож материалдарын қайта өңдеудің инновациялық тәсілдері

С.М. Нурмакова[1], У.К. Сарсембин[1], А. Далбанбай[1], Г.К. Абилова[2], Б.Х. Тусупова[3*], Л.С. Курбанова[3], Г.Б. Жаркимбаева[1], М. Шанбаев[4]

[1]*Satbayev University, Алматы, Қазақстан*
[2]*Қ. Жұбанов атындағы Ақтөбе өңірлік университеті, Ақтөбе, Қазақстан*
[3]*әл-Фараби атындағы Қазақ ұлттық университеті, Алматы, Қазақстан*
[4]*Ғ. Дәукеев атындағы Алматы энергетика және байланыс университеті, Алматы, Қазақстан*

**Корреспонденция үшін автор: tussupova@yandex.ru*

Аңдатпа. Бүкіл әлем көмір пайдалануды азайтуға бағытталған, бірақ мұндай саясатқа қарамастан, оны пайдалану көлемі өсіп жатқан елдер бар (Қытай, Үндістан). Егер көмірді пайдалану көлемі өссе, онда күл-қож қалдықтарының (материалдарының) көлемі артады, ал оларды кәдеге жарату немесе қайта өңдеу қажет. SiO_2, Al_2O_3, Fe_2O_3 көмірді жағудың жанама өнімінің құрамына кіретін негізгі элементтер. Жұмыста күл-қож материалдарын цемент, геополимер өндірісінде, цеолит синтезінде, микросфераны бөлуде, ауыл шаруашылығында, жерді мелиорациялауда, фиторемедиацияда, суды тазарту үшін реагент ретінде, жол құрылысында, пайдаланылған шахталарды толтыру кезінде пайдалану және қайта өңдеу, кәдеге жарату сияқты бағыттары бойынша шолу жасалған. Авторлар физикалық-химиялық талдау әдістерінің көмегімен күл қождарының негізгі құрамына SiO_2 (65.9%) және Al_2O_3 (22.5%) кіретінін растады. Нәтижесінде жоғары концентрациядағы кремний мен алюминий құрылыс және геополимерлік материалдар үшін, сондай-ақ керамикалық бұйымдар өндірісінде тиімді шикізат бола алатыны анықталды. Құрамындағы Fe_2O_3 (5.54%) каталитикалық процестерде және пигменттер өндірісінде қолдануға болады. Сулы күл сығындысының сілтілі реакциясы (pH = 9.25) күл қождарының химиялық құрамымен жақсы корреляциялайды және материалда белсенді сілтілі компоненттердің бар екендігін растайды. Осылайша, күлдің сілтілі табиғаты геополимерлеу процестеріне қолайлы болады және қышқыл активаторлармен әрекеттесу кезінде материалдың реакциялық қабілетін арттырады. Ал TiO_2-нің аз мөлшері (1.11%) күлге негізделіп жасалған материалдардың механикалық өнімділігін жақсартуға ықпал етуі мүмкін.

Негізгі сөздер: *циркулярлық экономика, жасыл экономика, өндірістік қалдықтар, күл-қож үйінділері, парниктік газдар, күлдің шығуы, күл-қож материалдары, отын қождары, күл-қож қоспасы.*

Инновационные подходы к переработке золошлаковых материалов топливно-энергетического комплекса в контексте устойчивого развития

С.М. Нурмакова[1], У.К. Сарсембин[1], А. Далбанбай[1], Г.К. Абилова[2], Б.Х. Тусупова[3*], Л.С. Курбанова[3], Г.Б. Жаркимбаева[1], М. Шанбаев[4]

[1]*Satbayev University, Алматы, Казахстан*
[2]*Актюбинский региональный университет им. К. Жубанова, Актобе, Казахстан*
[3]*Казахский национальный университет им. аль-Фараби, Алматы, Казахстан*
[4]*Алматинский университет энергетики и связи им. Г. Даукеева, Казахстан, Алматы, Казахстан*

**Автор для корреспонденции: tussupova@yandex.ru*

Аннотация. Весь мир нацелен на сокращение потребления угля, но несмотря на такую политику есть страны, где его потребление продолжает расти (Китай, Индия). Если растет потребление угля, то растет объем золошлаковых отходов (материалов), которые необходимо утилизировать, переработать с получение конечной продукции. В работе выполнен обзор по использованию и переработке золошлакоматериалов, и возможные направления утилизации: производство цемента, геополимера, в синтезе цеолитов, в разделении микросферы, в сельском хозяйстве, в мелиорации земель, в фиторемедиации, в качестве реагентов для очистки воды, в дорожном строительстве, при засыпке отработанных шахт. Физико-химическими методами анализа авторы подтвердили, что в основной состав золошлака входят SiO_2 (65.9%) и Al_2O_3 (22.5%). Вывод – кремний и алюминий, содержащиеся в высокой концентрации, могут быть эффективным сырьем для строительных и геополимерных материалов, а также в производстве керамических изделий. Наличие Fe_2O_3 (5.54%) открывает возможности для её использования в каталитических процессах и производстве пигментов. Щелочная реакция водной вытяжки золы (pH = 9.25) хорошо коррелирует с химическим составом золошлака и подтверждает наличие активных щелочных компонентов в материале. Тем самым щелочная природа золы

благоприятствует процессам геополимеризации и повышает реакционную способность материала при взаимодействии с кислыми активаторами. А незначительное присутствие TiO_2 (1.11%) может способствовать улучшению механических характеристик материалов на основе золы.

Ключевые слова: *циркулярная экономика, зеленая экономика, производственные отходы, золошлакоотвалы, парниковые газы, золоунос, золошлакоматериалы, топливный шлак, золошлаковая смесь.*

Publisher's note

All claims expressed in this manuscript are solely those of the authors and do not necessarily represent those of their affiliated organizations, or those of the publisher, the editors and the reviewers.

SATBAYEV UNIVERSITY

Engineering Journal of Satbayev University

Volume 148 (2025), Issue 3, 40-47

https://doi.org/10.51301/ejsu.2025.i3.06

Monitoring of the water and salt balance of the Bakbakty rice irrigation system under reuse of collector-drainage water for irrigation

M. Absametov[1], A. Ismagulova[1*], V. Mirlas[2], V. Kulagin[1], D. Umbetaliev[1], T. Rakhimov[1], V. Rakhimova[1]

[1]*Institute of Hydrogeology and Geoecology named after U.M. Akhmedsafin, Almaty, Kazakhstan*
[2]*Ariel University, Ariel, Israel*

**Corresponding author: ismagulovaaida101@gmail.com*

Abstract. This study presents the methodology, approach, and results of calculating the components of water and salt balances based on three years of field research on the reuse of collector-drainage water in the Tasmurun area of the Bakbakty irrigation system, under arid and low-water conditions typical for water-demanding rice fields. Balance calculations were based on data from in situ observations with active involvement of local farmers, ensuring data reliability. The water balance showed a slight negative discrepancy ranging from 0.4-0.6% in 2022 and 0.001-0.02% in 2023-2024, confirmed by groundwater level monitoring and maps. The salt balance showed a slight accumulation, with values from +0.016 to +0.29 t/ha in field No. 2 and +0.049 to +0.089 t/ha in field No. 4. Seasonal salt increases were linked to leaching regimes and the dominance of easily soluble salts, posing no threat to land reclamation status.

Keywords: *water and salt balance, irrigated lands, drainage systems, collector-drainage water, salinity, water quality.*

Received: 10 January 2025
Accepted: 15 June 2025
Available online: 30 June 2025

1. Introduction

The review and analysis of domestic and international publications and scientific studies demonstrate increasing attention to water and salt balance research and the reclamation status of rice irrigation systems. These issues have become central in recent years as tools for actively managing irrigated areas' water-salt regime and regulating groundwater levels during both the growing and non-irrigated seasons for rice and accompanying crops. The growing scarcity of water resources necessitates the search for additional sources of irrigation water, including the reuse of collector-drainage water formed within rice irrigation systems [1-4].

For example, Y. Okuda (2020) [5] presented results of water and salt balance studies on agricultural lands subject to leaching, using shallow subsurface drainage combined with traditional drainage. Secondary salinization in arid regions was shown to raise groundwater levels. The system was implemented on farmland in Uzbekistan.At the 16th International Conference «Monitoring of Geological Processes and Ecological Condition of the Environment», Rokochynskiy et al. (2022) [6] analyzed the causes of unsatisfactory hydrological and reclamation conditions in Danube rice irrigation systems. Their study proposed improving drainage efficiency by reducing the vertical infiltration rate in the drainage zone to no more than 25 mm/day. Turchenyuk et al. (2017) [7] examined the water balance and salt distribution in arable lands, wastelands, and ponds in a typical irrigated area. A water balance model was developed to assess irrigation impacts on soil salinity across different land types. R. Singh, J.C. van Dam, and R.K. Jhorar [8] applied a calibrated SWAP agro-hydrological model to assess water and salt balances on farm fields. Soil hydraulic properties were identified as key variables and were calibrated using PEST based on measured soil moisture and salinity before and after irrigation. Kasymbetova and Ergasheva (2020) [9] evaluated the water-salt balance of floodplain areas, the aeration zone, and root zone of crops in the Shuruzak massif of the Syrdarya region, assessing the reclamation status of irrigated lands. Zaitsev V.B., Semenenko A.N. [10], and Reshetnyak N.F. [11] described the features of groundwater regimes in flooded rice fields and the effects of groundwater on the dynamics of water-soluble salts in paddy soils.

Thus, the discussion and analysis of numerous studies confirm the critical importance of water-salt balance analysis. The justification of real and forecasted parameters for the quantitative and qualitative potential of collector-drainage water reuse must be based on accurate water and salt balance data [12]. Furthermore, in irrigation practice, it is often necessary to evaluate long-term average balances and those specific to water availability levels and critical seasonal periods.

Accordingly, this study presents the methodology and results of calculating all inflow and outflow components of the water and salt balance at the field level for a rice-alfalfa crop rotation system. These findings summarize three years of field-based scientific research on implementing collector-drainage water reuse technologies in the Tasmurun section of the Bakbakty irrigation system.

m.absametov@satbayev.university; ismagulovaaida101@gmail.com; vladimirm@ariel.ac.il; vitali_kulagin@mail.ru; doc_dauren@mail.ru; rakhimov@mail.ru; valentina.salybekova@gmail.com
Engineering Journal of Satbayev University. eISSN 2959-2348. Published by Satbayev University

2. Materials and methods

The field research was conducted in the Balkhash district of the Almaty region, Republic of Kazakhstan, within the Ili River basin, specifically in the Tasmurun area of the Bakbakty system of the Akdaly irrigation massif.

The irrigated lands are located within part of the ancient delta of the Ili River, whose surface was shaped by successive erosional and accumulative processes against the background of aeolian activity. The average surface slope is approximately 0.0002.

Climatically, the area belongs to the desert zone, which, combined with the shallow depth of the groundwater table, contributes to the intensive development of salt accumulation processes in the soil profile.

As a representative site for implementing the technology of collector-drainage water reuse, the irrigation (Tasmurun Main Canal) and collector-drainage network (collector K-2) of the Tasmurun section of the Bakbakty irrigation system were selected. These systems serve the irrigated lands of SPK «Miyaly Agro», PC «Dinara», and LLP «EDD».

The beneficiaries and direct participants of the experimental studies included three farming enterprises – «Raimbek», «Bagnur», and «Alga» - affiliated with SPK «Miyaly Agro» and PC «Dinara».

The total irrigated area of the six-field rice-alfalfa crop rotation system is 890 hectares, of which the experimental area covers 607 hectares, including:

– Field 2. 173 ha (81 ha under SPK «Miyaly Agro» and KFH «Alga», and 92 ha under PC «Dinara»);

– Field 3. 187 ha under PC «Dinara»;

– Field 4. 138 ha under PC «Dinara»;

– Field 5. 109 ha under LLP «EDD».

The cropping structure for 2022-2024 was as follows: rice was cultivated on fields 2 (173 ha) and 4 (138 ha), while alfalfa was cultivated on fields 3 (187 ha) and 5 (109 ha) (Figure 1).

The water and salt balance calculations were based on empirical data from stationary hydrogeological monitoring, measurements of collector-drainage water flow, meteorological observations, and agricultural and water management conditions information. These calculations were conducted separately for two experimental fields (fields 2 and 4), where rice was cultivated in 2022 under the existing irrigation regimes and technical operation conditions of the Tasmurun section of the Bakbakty massif, and in 2023-2024 using a recirculating water use system.

The water balance equation for the irrigated experimental plots is as follows [12]:

$$S_w + S_r + S_g - S_d - S_e - S_i - S_f = \pm\Delta S, \text{ million m}^3 \quad (1)$$

where:

$\pm\Delta S$ – balance discrepancy;

S_w – volume of irrigation water;

S_r – atmospheric precipitation;

S_g – groundwater inflow into the experimental site;

S_d – volume of drainage-discharge outflow;

S_e – total evaporation;

S_i – infiltration into the aeration zone from irrigation and mixed irrigation-drainage water;

S_f – lateral filtration outflow beyond the experimental plots.

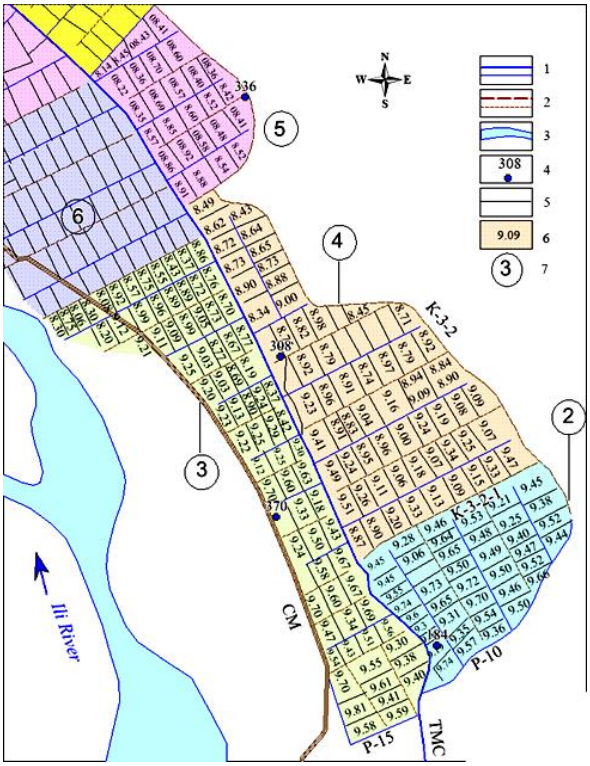

Figure 1. Schematic map of the irrigation and collector-drainage network with land use layout for the experimental research plots (III rotation system, fields 2, 3, 4, and 5): 1 – irrigation canals; 2 – collectors; 3 – river; 4 – monitoring hydrogeological well and its inventory number; 5 – boundary of the rice check; 6 – absolute elevation of the rice check; 7 – field number

The incoming components of the water balance included: the amount of atmospheric precipitation, the volume of irrigation water supplied (including the reuse of collector-drainage water), and the inflow of groundwater to the experimental plots.

The total volume of precipitation received over the irrigated area of fields No. 2 and No. 4 (planted with rice) during the hydrological year was calculated using the formula:

$$S_a = N_a \cdot S_r, \quad (2)$$

where:

N_a – total atmospheric precipitation, mm;

S_r – total calculated area, ha.

The volume of irrigation water supplied was determined based on two conditions: in the first year of the experiment, the existing irrigation regimes and technical operating parameters were used; in the subsequent two years, recommended irrigation regimes and rice irrigation technologies with implementation of a recirculating water reuse system were applied.

Groundwater inflow to the field-level experimental plots of the Tasmurun irrigation system was calculated using the formula:

$$S_g = J \cdot B \cdot T \cdot 365, \quad (3)$$

where:

J – average hydraulic gradient of the groundwater table for the hydrological year;

B – width of the groundwater flow, m;

T – transmissivity of the aquifer, m^2/day.

The outgoing components of the water balance included: the volume of drainage-discharge flow, the total evaporation, the volume of water that infiltrated into the aeration zone due to irrigation and mixed irrigation-collector-drainage water, and the lateral filtration outflow of groundwater beyond the boundaries of the experimental plots.

Drainage-discharge flow was estimated based on hydrometric measurements of collector-drainage water discharge from the irrigated lands of the experimental plots at certified hydrological posts during the growing season.

The formula calculated the lateral filtration outflow of groundwater beyond the experimental area:

$$S_f = J \cdot B \cdot T \cdot 240, \quad (4)$$

where:

J – hydraulic gradient derived from the post-irrigation hydroisohypse map;

B – width of the subsurface flow, m;

T – aquifer transmissivity, m^2/day;

240 – average duration of the calculation period, days.

The actual parameters were based on maps of filtration coefficients and hydrogeological cross-sections developed for the experimental sites.

The volume of moisture accumulated in the aeration zone was calculated as:

$$S_i = F_n \cdot h_{avg} \cdot W_{avg}, \quad (5)$$

where:

F_n – total area of the calculated land plots with uniform groundwater depths and saturated zone thickness, before and after irrigation (m^2). These were determined from monitoring well data and interpolated according to the delineated calculation contours for the experimental sites.

h_{avg} – average groundwater level change during the irrigation period within the calculation contours (m), obtained from constructed groundwater fluctuation graphs from 2021 to 2024 (Figure 2);

W_{avg} – average volumetric water content of the aeration zone soil, expressed as a fraction. The volumetric moisture and field capacity values were taken from field and laboratory investigations.

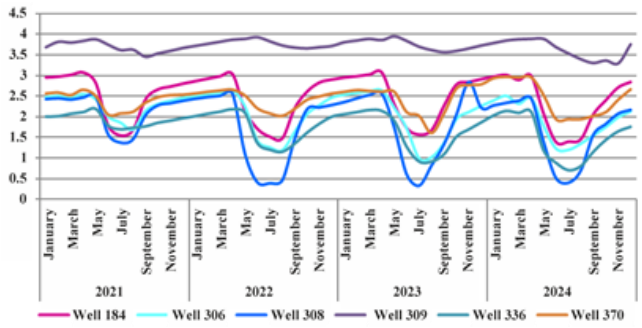

Figure 2. Groundwater level fluctuation graphs in monitoring wells located on irrigated lands of the experimental research plots and adjacent areas during the observation period from 2021 to 2024

The salt balance was calculated using the following equation:

$$\pm\Delta M = M_{gn} + M_w + Ma - M_{gk} - M_d - M_f, \quad \ldots\ldots(6)$$

where:

$\pm\Delta M$ – balance discrepancy;

M_{gn} – salt content in groundwater of the balance layer at the beginning of the calculation period;

M_{gk} – the same at the end of the calculation period;

M_v, M_a – the volume of salts brought in with irrigation water and precipitation, respectively;

M_d, M_f – the volume of salts carried out by the corresponding drainage and underground outflow outside the massif.

The volume of salts brought in with irrigation water, precipitation and underground inflow within the calculation contour was calculated using the equation:

$$M_v = W \cdot m, \quad (7)$$

where:

W – water volume, million m^3;

m – mineralization of irrigation water (2022) and mixed with collector-drainage water (2023-2024) (Figure 3); groundwater mineralization (Figure 4), mg/dm^3.

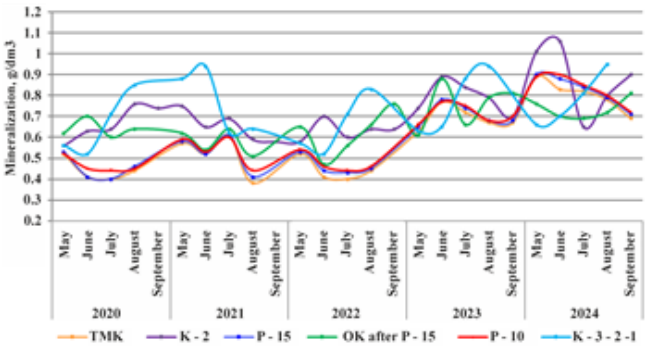

(a)

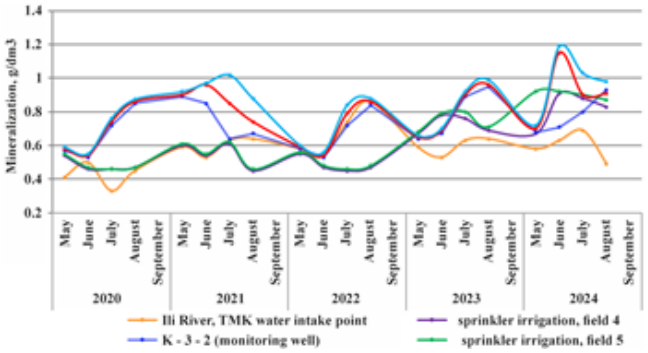

(b)

Figure 3. Dynamics of mineralization of irrigation and collector-drainage waters on irrigated lands of the experimental site and adjacent territories, a) before the start (2020-2022) and b) during the research (2023-2024), g/dm^3

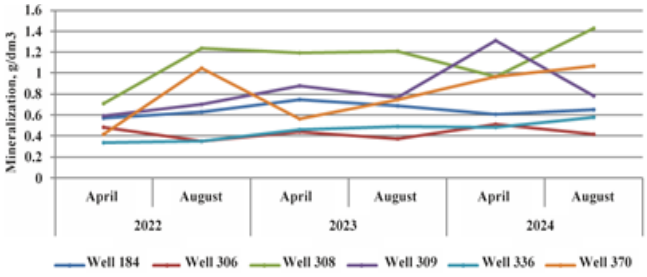

Figure 4. Graph of the dynamics of groundwater mineralization in monitoring pits on irrigated lands of experimental sites before the beginning (2022) and during scientific research (2023-2024), g/dm^3

The salt content in groundwater of the balance layer at the beginning of the calculation period was determined by the calculation filtration blocks and by the equation:

$$M_{gn} = 0.001 \cdot F \cdot (h_y - h_{gw}) \times W_n \cdot M_{gw}, \quad (8)$$

where:

0.001 – conversion factor;

F – area of the calculation contour, ha;

h_y –depth of the balance layer base (10 m);

h_{gw} – average weighted depth of groundwater at the beginning of the calculation period, m

W_n – total moisture capacity of aquifers;

M_{gw} – average weighted mineralization of groundwater within the calculation contour at the beginning of the calculation period, mg/dm^3 (Figure 4).

The volume of salts carried beyond the design contour by underground outflow was calculated using the equation:

$$M_f = W \cdot m, \quad (9)$$

W – the volume of groundwater carried beyond the design contour by underground outflow (taken from water balance articles), million m^3;

M – groundwater mineralization during the non-growing season, mg/dm^3.

The volume of salts carried beyond the design contour by collector-drainage runoff was calculated using the equation:

$$M_{drain} = W_{drain} \cdot m, \quad (10)$$

where:

W – the volume of collector-drainage runoff (taken from the water balance) of groundwater carried beyond the design contour by underground outflow (taken from water balance articles), million m^3;

m – the mineralization of collector-drainage runoff, mg/dm^3.

The salt content in groundwater of the balance layer at the end of the calculation period was determined based on the calculation filtration blocks and the equation:

$$M_{gk} = 0.001 \cdot F \cdot (h_y - h_{gw.e}) \cdot W_n \cdot M_{gw.e}, \quad (11)$$

where:

$h_{gw.e}$ – weighted average depth of groundwater at the end of the calculation period, m;

W_n – total moisture capacity of aquifers;

$M_{gw.e}$ – weighted average mineralization of groundwater within the calculation contour at the end of the calculation period, mg/dm^3 (Figure 4).

Wells 184, 306 and 308 – rice; wells 336, 370 – alfalfa; well 309 – on cutting. Figure 4 shows the graph of the dynamics of groundwater mineralization in monitoring wells on irrigated lands of experimental sites before the start (2022) and during scientific and applied research (2023-2024), g/dm^3.

3. Results and discussion

Table 1 presents detailed results of the calculated inflow and outflow components of the water balance for irrigated lands at the experimental plots of the Tasmurun irrigation system.

Table 1. Water balance of irrigated lands at the experimental plots of the Tasmurun irrigation system with the implementation of a field-level return-flow reuse system of collector-drainage water, before (2022) and during the applied scientific research period (2023-2024)

Components of the balance sheet	On rice crops of experimental field No. 2				On rice crops of experimental field No. 4			
	Year of experiment	m^3/ha	million m^3	%	Year of experiment	m^3/ha	million m^3	%
Incoming balance sheet items								
Water supply	2022	23879	4.131	92.9	2022	26082	3.599	93.3
	2023	22900/17518*	3.962/3.031*	93.5	2023	22900/17518*	3.16/2.417*	93.5
		5382**	0.931**			5382**	0.743**	
	2024	22900/17518*	3.962/3.031*	91.4	2024	22900/17518*	3.16/2.417*	91.0
		5382**	0.931**			5382**	0.743**	
Atmospheric precipitation	2022	1489	0.258	5.8	2022	1489	0.206	5.3
	2023	1241	0.214	4.8	2023	1241	0.171	5.1
	2024	1860	0.322	7.2	2024	1860	0.257	7.4
Groundwater inflow	2022	323.7	0.056	1.3	2022	355.1	0.049	1.4
	2023	358.4	0.062	1.7	2023	333.3	0.046	1.4
	2024	283.2	0.049	1.4	2024	384.1	0.053	1.6
Total	2022	25691.7	4.445	100	2022	27926.1	3.854	100
	2023	24499.4	4.238	100	2023	24474.3	3.380	100
	2024	25043.2	4.333	100	2024	25144.1	3.470	100
Balance sheet expense items								
Total evaporation	2022	10930	1.890	41.7	2022	10930	1.5083	38.9
	2023	10930	1.890	42.5	2022	10930	1.5083	44.6
	2024	10930	1.890	43.6	2022	10930	1.5083	43.4
Drainage and discharge flow	2022	12768	2.209	50	2022	14717	2.031	63.5
	2023	11855	2.051	50.3	2023	11348	1.566	46.3
	2024	12572	2.175	49.9	2024	11877	1.639	47.1
Moisture accumulation in the aeration zone	2022	1601.0	0.277	6.0	2022	1754	0.243	6.2
	2023	1277.4	0.221	4.9	2023	1442	0.199	5.9
	2024	1304.6	0.179	4	2024	1601	0.221	6.3
Groundwater outflow	2022	514.4.	0.0894	2.3	2022	710.1	0.098	2.4
	2023	549.1	0.095	2.3	2023	797.1	0.11	3.2
	2024	595.4	0.103	2.5	2024	797.1	0.11	3.2
Total	2022	25809	4.465	100	2022	28111.1	3.879	100
	2023	246112.5	4.258	100	2023	24490.3	3.383	100
	2024	25127.0	4.347	100	2024	25205.1	3.478	100
Balance (discrepancy) of the balance	2022	-117.3(0.4%)	-0.020	–	2022	-190(0.6%)	- 0.025	–
	2023	- 116.5(0.5%))	-0.020	–	2023	-19.8 (0.001%)	- 0.003	–
	2024	- 83.8 (0.3%)	- 0.014	–	2024	-58.1(0.2%)	- 0.008	–

Assessment of Precipitation and Irrigation Contributions to the Water Balance of Rice Fields in the Tasmurun Irrigation System under Conditions of Water Scarcity (2022-2024)

According to data from the Bakanas Regional Meteorological Station, the total volume of atmospheric precipitation on the irrigated lands of fields No. 2 and No. 4 amounted to 257.6 and 205.5 thousand m³ in 2022, 214.7 and 171.3 thousand m³ in 2023 and 321.8 and 256.7 thousand m³ in 2024, respectively. These values indicate prevailing arid and water-deficient climatic conditions, as precipitation contributed only 4.5-7.4% to the total inflow components of the water balance.

In 2022, the volume of irrigation water supplied by the state municipal enterprise for water management «Balkhashirrigation» for rice cultivation in fields No. 2 and No. 4 amounted to 4.13 and 3.59 million m³, respectively. The net irrigation norm at the field level was 23.87 and 26.08 m³/ha.

With the implementation of recommended irrigation regimes and rice irrigation technologies, including using a return flow system to reuse collector-drainage waters, the total irrigation volume in 2023-2024 was reduced. For fields No. 2 and No. 4, the irrigation volumes were 3.962 and 3.16 million m³, respectively, with a unified net irrigation norm of 22.90 m³/ha. Of these totals, 3.03 and 2.41 million m³ were supplied from the surface water of the Ili River. At the same time, 0.931 and 0.743 million m³ originated from collector-drainage waters pumped from collector K-2 into the Tasmurun central canal. The substitution of irrigation water with drainage water accounted for approximately 23.5% across both experimental sites during 2023-2024.

The calculations confirm that irrigation is the primary forming component of the water balance, with irrigation water volumes contributing from 91.0% to 93.4% of the total inflow balance.

The value of total evapotranspiration was assumed to be 10.93 thousand m³/ha for all three years of the study, constituting more than 40% of the total outflow balance. This finding supports the widely accepted understanding that rice, being cultivated under waterlogging or partial submersion conditions, belongs to the group of hydrophytes. Hydrophytic plants exhibit high transpiration rates and possess permanently open stomatal apparatuses. As a result, the evapotranspiration of rice plants is equivalent to the rate of free evaporation from open water surfaces.

Changes in soil moisture reserves in the vadose zone and groundwater levels (Table 2) were influenced by rice crop area, infiltration water losses, and the depth of the groundwater table.

A salt balance calculation was performed to assess the direction of salt transfer processes on irrigated lands. The overall salt balance is directly related to the components of the water balance, since the movement of salts in the aeration zone occurs in the form of water-salt solutions (Table 3).

Table 2. Moisture accumulation calculations in irrigated lands of experimental sites of the Tasmurun irrigation system before and during the field studies (2022-2024)

Increment, m	Year of research	Area of the calculated contour, ha	Average weighted depth of groundwater, m		Increment, m	Volume due to increment, million m³	Average volumetric moisture content of soils in the aeration zone, W_{total}	Average volumetric moisture content of soils in the aeration zone, W_{total}
			April	September				
Field No. 2	2022	173	3.0	2.5	+0.5	0.865	0.32	0.2773
	2023	173	3.0	2.6	+0.4	0.692	0.32	0.2214
	2024	173	3.0	2.68	+0.32	0.5597	0.32	0.1791
Field No. 2	2022	138	3.0	2.45.	+0.55	0.7590	0.32	0.2429
	2023	138	3.0	2.55	+0.45	0.6210	0.32	0.1987
	2024	138	3.0	2.5	+0.5	0.690	0.32	0.2208

Note: Table content should follow in your formatted manuscript with appropriate scientific units and descriptions

Table 3. Salt balance of irrigated lands on experimental plots (fields 2 and 4) III - its rice-alfalfa crop rotation of the Tasmurun irrigation system before the start (2022) and during scientific and applied research (2023-2024)

Balance sheet items	Elements of salt balance	On rice crops of experimental field No. 2		T/ha tn	On rice crops of experimental field No. 4		T/ha tn
		A year of experimental research			A year of experimental research		
		2022	2023	2024	2022	2023	2024
Incoming	Salt content of the balance layer at the beginning of the calculation period before sowing rice	1.28	1.36	1.344	1.395	2.044	2.53
		221.6	236.15	232.51	192.51	282.07	349.31
	The volume of salts brought in with irrigation and mixed drainage water	12.178	16.259	17.862	14.345	16.717	17.175
		2106.84	2812.81	3090.13	2481.69	2306.95	2370.15
	The volume of salts brought in by atmospheric precipitation	0.301	0.253	0.381	0.301	0.253	0.381
		52.073	43.769	65.965	41.538	34.914	43.884
	The volume of salts brought in by underground inflow	0.226	0.286	0.269	0.302	0.366	0.461
		39.098	49.478	46.537	41.676	50.508	63.618
	Total	13.985	18.158	19.856	16.343	19.380	20.547
		2419.405	3142.21	3435.14	2255.33	2674.44	2841.81
Outgoing	The salt content of the balance layer at the end of the calculation period after rice harvesting	2.44	3.157	3.120	2.681	3.589	5.111
		422.3	546.16	539.96	370.01	495.25	705.27
	Removal of salts by collector-drainage runoff	9.065	11.144	11.943	12.510	10.440	11.521
		1568.0	1927.9	2066.2	1726.4	1440.7	1589.8
	Removal of salts by filtration and discharge of runoff	1.84	3.421	4.378	0.720	4.545	3.109
		318.32	591.833	757.394	99.36	627.21	429.042
	The volume of salts carried beyond the calculated contour by underground outflow	0.350	0.399	0.399	0.497	0.757	0.717
		60.55	69.013	69.013	68.596	104.499	98.946
	Total	13.695	18.121	19.840	16.408	19.331	20.458
		2369.235	3134.933	3432.32	2264.36	2667.678	2832.204
	Salt balance (mismatch), + increase, - decrease	+0.29	+0.037	+0.016	-0.065	+0.049	+0.089
		+50.17	+7.28	+2.82	-9.03	+6.76	+9.61

The magnitude of the positive discrepancy of the salt balance in the experimental plots (fields 2 and 4) III - its rice-alfalfa crop rotation of the Tasmurun irrigation system before the start (2022) and during scientific and applied research (2023-2024) amounted to minimal values, even with the repeated use of collector-drainage waters from +0.016 to +0.29 tons/ha in rice field No. 2 and from +0.049 to +0.089 tons/ha in rice field No. 4, which indicates the predominance of insignificant accumulation of salt reserves in the zone of active salt exchange during the growing season. The leaching regime of rice and the prevalence of readily soluble salts in the chemical composition of groundwater, the increase in salts is seasonal and will not lead to a regional deterioration in the meliorative state of irrigated lands.

According to the data of the salt survey and the preliminary compiled schematic map of the degree and type of salinization of irrigated lands in the soil layer of 0-0.100 cm, the soils in all areas after the experimental studies are classified as non-saline (85% of the surveyed area) and on the lands adjacent to the collector-drainage network, a narrow strip is represented by slightly saline, the salinization type is sulfate-sodium-calcium. In the alfalfa fields, the soils are somewhat saline, and the salinization type is sulfate-hydrocarbonate-calcium. The salt content in the soil profile varies from 0.185% in the upper soil layer to 0.091% at a depth of 60 cm and below.

4. Conclusions

Substantiation of Forecasted Characteristics and the Potential for reuse of collector-drainage water in the Tasmurun irrigated area of the Bakbakty irrigation system

The justification for forecasted real characteristics, quantitative and qualitative potential, and the intensity of collector-drainage water reuse presented in this study is based on a comprehensive analysis of the water and salt balances in the Tasmurun section of the Bakbakty irrigation system. This system serves the irrigated lands of the agricultural enterprises SPC “Miyaly Agro,” PC “Dinara,” and LLP “EDD.” The research was conducted over three consecutive years, all characterized as arid and water-deficient, particularly affecting the water availability of moisture-sensitive rice fields.

A notable strength of the study is that the estimation of all components of the water and salt balances – both inflows and outflows – was not based on secondary literature or archival data. Instead, it was derived from field-based empirical measurements conducted directly by project stakeholders, namely local farmers. This approach ensured the reliability and validity of the baseline data used.

The recommended rice irrigation technology incorporated the reuse of collector-drainage return flow and entailed a phased water application strategy. During the initial flooding and maintenance stages (Stages I-III), irrigation relied solely on river water. During subsequent stages (Stages IV-VI), a blended water source was used, with drainage water accounting for up to 30% and river water for up to 70% of the irrigation volume. In practice, during the 2023-2024 vegetation periods, collector-drainage waters comprised up to 25% of the irrigation volume, with the remaining 75% sourced from river inflow.

Results from the water balance analysis of irrigated lands revealed a slight negative discrepancy, ranging from 0.4% to 0.6% in 2022 and from 0.001% to 0.02% in 2023-2024. These deviations correspond to an average drop in the groundwater table across the experimental sites – from 0.04 m in 2022 to 0.015 m in 2023-2024 as confirmed by stationary groundwater level monitoring and supporting cartographic materials. These results indicate that the inflow components of the water balance exhibit relative stability and are well-balanced by the outflow components.

The salt balance discrepancy on the experimental rice-alfalfa rotation fields (fields 2 and 4) of the Tasmurun irrigation system, both before (2022) and during (2023-2024) the applied research, showed only slight positive values, even with the reuse of collector-drainage waters. The excess salt accumulation ranged from +0.016 to +0.29 tons/ha on Field No. 2 and from +0.049 to +0.089 tons/ha on Field No. 4, indicating a minor salt buildup within the active salt-exchange zone over the vegetation period.

The leaching irrigation regime of rice cultivation, the predominance of highly soluble salts in the groundwater composition, and the seasonal character of salt accumulation suggest no adverse regional impact on the reclamation status of irrigated lands.

Based on soil salinity surveys and a preliminary schematic map of salinity types and severity in the 0-100 cm soil layer, most surveyed land (85%) was classified as non-saline following the experimental period. Narrow strips adjacent to the collector-drainage network showed weak salinization, predominantly sulfate-sodium-calcium type. Alfalfa fields exhibited weak salinization of the sulfate-bicarbonate-calcium type. Salt content in the soil profile ranged from 0.185% in the upper layers to 0.091% at depths of 60 cm and deeper.

Author contributions

Conceptualization: MA, AI, VM, VR; Data curation: AI; Formal analysis: AI, VK, DU; Funding acquisition: AI, MA; Investigation: AI, VK, TR; Methodology: AI; Project administration: MA, AI, VM; Resources: AI, VK, VM; Software: AI, TR; Supervision: AI; Validation: AI; Visualization: AI, MA; Writing – original draft: AI; Writing – review & editing: VM, TR, VR. All authors have read and agreed to the published version of the manuscript.

Funding

This research was funded by the Science Committee of the Ministry of Science and Higher Education and Science of the Republic of Kazakhstan («Groundwater resources as the main reserve of sustainable irrigated agriculture in Kazakhstan» № BR 21882211).

Acknowledgements

The authors gratefully acknowledge the editor and the reviewers for their critical reading of the manuscript and for offering thoughtful feedback that helped refine the clarity and scientific rigor of the work.

Conflict of interest

The authors declare no conflict of interest.

Data availability statement

The original contributions presented in this study are included in the article. Further inquiries can be directed to the corresponding author.

References

[1] Khimich, D.P. (1969). Water and Salt Balance and Issues of Rice Irrigation Systems. *Moscow Hydromelioration Institute.*
[2] Zulu, G., Toyota, M. & Misawa, S. (1996). Water reuse and its effects on water balance and ecosystems. *Agricultural Water Management*, (31), 269-283. https://doi.org/10.1016/0378-3774(95)01233-8
[3] Bazhenov, M.G. & Sarsenbayev, M.Kh. (1979). Regulation of Water-Salt Regime. *Almaty: Kainar.*
[4] Velichko, E.B. (1977). Water-Saving Techniques for Rice Cultivation. *USSR Conf. Proc., Moscow*, 41-43.
[5] Institute of Hydrogeology and Geoecology named after U.M. Akhmedsafin. (2023). Groundwater Resources as the Main Reserve of Irrigated Agriculture in Kazakhstan. *Almaty, Kazakhstan*.
[6] Okuda, Y. (2020). Secondary Salinization in Arid Regions. *Water*, *12*(11), 3207.
[7] Reports for 2016-2023. Regional Hydrogeological and Meliorative Center of the Ministry of Agriculture of the Republic of Kazakhstan. https://doi.org/10.3390/w12113207
[8] Turchenyuk, V., Frolenkova, N., & Rokochynskyi, A. (2017). Environmental and economic foundations of system optimization of operational, technological and construction parameters of rice irrigation systems. *Environmental Economics*, *8*(2), 76-82. https://doi.org/10.21511/ee.08(2).2017.08
[9] Mirlas, V., Kulagin, V., Ismagulova, A., & Anker, Y. (2022). Field Experimental Study on the Infiltration and Clogging Processes at Aksu Research Site, Kazakhstan. *Sustainability*, *14*(23), 15645. https://doi.org/10.3390/su142315645
[10] Singh6 J.C., van Dam, R.K., Jhorar6 R.K. (n.d.). Water and Salt Balances. *WUR eDepot.*
[11] Absametov, M.K. (2020). Rational Use and Protection of Groundwater in the Republic of Kazakhstan in the Context of Climatic and Anthropogenic Changes. *Almaty, Kazakhstan.*

Суару үшін коллекторлық-дренаждық суды қайта пайдаланудағы Бақбақты күріш суару жүйесінің су-тұз теңгеріміне мониторинг жүргізу

М. Әбсаметов[1], А. Исмағұлова[1*], В. Мирлас[2], В. Кулагин[1], Д. Үмбеталиев[1], Т. Рахимов[1], В. Рахимова[1]

[1]*У.М.Ахмедсафин атындағы Гидрогеология және геоэкология институты, Алматы, Қазақстан*
[2]*Ариэль университеті, Ариэль, Израиль*

**Корреспонденция үшін автор: ismagulovaaida101@gmail.com*

Аңдатпа. Бұл зерттеуде суды қажет ететін күріш алқаптарына тән құрғақ және суы аз жағдайларда Бақбақты суару жүйесінің Тасмұрын учаскесінде коллекторлық-дренаждық суды қайта пайдалану бойынша үш жыл бойы жүргізілген далалық зерттеулердің негізінде су-тұз балансының құрамдас бөліктерін есептеу әдістемесі, тәсілі және нәтижелері берілген. Баланс есептеулері деректердің сенімділігін қамтамасыз ете отырып, жергілікті фермерлерді белсенді түрде тарта отырып, in-situ бақылау деректеріне негізделген. Су балансы 2022 жылы 0.4-0.6% және 2023-2024 жылдары 0.001-0.02% аралығындағы шағын теріс сәйкессіздікті көрсетті, бұл жер асты суларының деңгейінің мониторингі және карталарымен расталды. Тұз балансы шамалы жинақтауды көрсетті, №2 кен орнында +0.016-дан +0.29 т/га-ға дейін және №4 кен орнында +0.049-дан +0.089 т/га-ға дейін. Тұздың маусымдық көбеюі сілтілеу режиміне және құрлыққа оңай еритін тұздардың басым болуына байланысты болды, бұл қайталану қаупі жоқ.

Негізгі сөздер: *су-тұз балансы, суармалы жерлер, құрғату жүйелері, коллекторлық-дренаждық сулар, тұздылық, су сапасы.*

Мониторинг водно-солевого баланса рисовой оросительной системы Бакбакты при повторном использовании коллекторно-дренажных вод на орошение

М. Абсаметов[1], А. Исмагулова[1*], В. Мирлас[2], В. Кулагин[1], Д. Умбеталиев[1], Т. Рахимов[1], В. Рахимова[1]

[1]*Институт гидрогеологии и геоэкологии имени У.М. Ахмедсафина, Алматы, Казахстан*
[2]*Университет Ариэль, Ариэль, Израиль*

**Автор для корреспонденции: ismagulovaaida101@gmail.com*

Аннотация. В данной работе представлены методология, подход и результаты расчета компонентов водно-солевого баланса на основе трехлетних полевых исследований по повторному использованию коллекторно-дренажных вод в районе Тасмурун оросительной системы Бакбакты в засушливых и маловодных условиях, характерных для водоемких рисовых полей. Расчеты баланса проводились на основе данных натурных наблюдений при активном участии местных фермеров, что обеспечило достоверность данных. Водный баланс показал небольшое отрицательное расхождение в пределах 0.4-0.6% в 2022 году и 0.001-0.02% в 2023-2024 годах, подтвержденное мониторингом уровня грунтовых вод и картами. Солевой баланс показал незначительную аккумуляцию, значения

от +0.016 до +0.29 т/га на поле № 2 и от +0.049 до +0.089 т/га на поле № 4. Сезонные повышения солей были связаны с режимами промывки и доминированием легкорастворимых солей, не представляющих угрозы мелиоративному состоянию земель.

Ключевые слова: *водно-солевой баланс, орошаемые земли, дренажные системы, коллекторно-дренажные воды, засоление, качество воды*.

Publisher's note

All claims expressed in this manuscript are solely those of the authors and do not necessarily represent those of their affiliated organizations, or those of the publisher, the editors and the reviewers.

CONTENTS

МАЗМҰНЫ

СОДЕРЖАНИЕ

Учредитель: Satbayev University

Регистрация:
Министерство информации и общественного развития Республики Казахстан
№ KZ19VPY00056529 от 30.09.2022

Официальный сайт: https://vestnik.satbayev.university/index.php/journal/

Основан в августе 1994 г. Выходит 6 раз в год

Адрес редакции:
г. Алматы, ул. Сатпаева,
22 тел.: 292-63-46